ABSTRACT

SINGLE AND MULTIPHASE MIXING IN PARTIALLY FILLED STIRRED VESSELS

by
Shilan Motamedvaziri

In many industrial applications, mixing vessels have a liquid height-to-tank diameter ratio, H/T, equal to, or larger than 1. However, there are many instances where this ratio is lower than 1, as in all those cases in which the vessel is either emptied or filled. Even when H/T<1, sufficient agitation must still be provided in order to attain the desired process objectives. When the impeller submergence is reduced as a result of lowering the liquid level, the fluid dynamics of even a single-phase stirred liquid can become quite complex, with different regimes possibly existing depending on the geometric characteristics of the system (such as impeller clearance, liquid height, or liquid submergence above the impeller). The objectives of this work were to study in detail the hydrodynamic changes that occur when H/T is decreased, and to determine the minimum liquid levels and the critical impeller submergence for different impeller off-bottom distances, impeller diameters and agitation speeds where adequate mixing process can still be achieved, both in a single liquid phase and in solid-liquid suspensions.

Flat-bottomed, baffled vessels (5L, 12L, 20L and 170L) equipped with a single disk turbine (DT) of four different sizes placed at five different impeller off-bottom clearances were used here to study the system's hydrodynamics and related mixing phenomena. A number of experimental tools were used to analyze the systems under investigation, including: Particle Image Velocimetry (PIV) for the experimental determination of the velocity profiles, and after the appropriate data manipulation, the

impeller pumping capacity and its Pumping Number; a colorimetric system coupled with image processing to quantify mixing time; a strain gage-based rotary torque transducer system to measure the power dissipated by the impeller; and a visual observation method to determine the minimum agitation speed for complete solids suspension, N_{js}. In addition, Computational Fluid Dynamics (CFD) modeling was used to predict the behavior of the system in terms of its velocity profile, Power Number, Pumping Number, and mixing time. CFD predictions were obtained using a multiple reference frame (MRF) model coupled, when needed, with a Volume of Fluid (VOF) model, in order to study systems in which a vortex could be expected to form.

In general, good agreements between the experimental data and the predicted results for the velocities distribution, Power Number, radial Pumping Number, mixing time, and N_{js} were obtained. Results show that there is a critical impeller submergence ratio S_b/D below which: (1) the macroscopic flow pattern generated by the impeller changes substantially, transitioning from either a “double-loop” recirculation flow or a "single-loop" recirculation flow (depending on the impeller clearance off the tank bottom) to an upward "single-loop" recirculation flow; (2) the Power Number and radial Pumping Number drop significantly; (3) solid suspension cannot be attained at any agitation speed; (4) mixing time increases suddenly; (5) vortex formation occurs, air entrainment is significantly facilitated, and impeller flooding typically results. This is the first time that such hydrodynamic regime change has been reported and characterized. When this flow regime transition occurred, it was observed that the average velocity field and turbulence intensity close to the tank bottom decreased substantially; this was identified as the reason why solid suspension became unachievable. Furthermore, the

critical impeller submergence ratio resulting in the establishment of the newly described flow regime was not affected by dynamic variables such as agitation speed. Impeller flooding was observed only when the new regime was established and when the vortex depth reached the impeller disk. This phenomenon was correlated to critical values of the Froude number. Additionally, by decreasing the impeller off-bottom clearances the operating window within which the stirred vessels could be operated effectively became wider. However, for low impeller off-bottom clearances ($C_b/T<0.05$) and low impeller submergence ratios ($S_b/D<0.37$, corresponding to $H/T<0.16$) even the lower recirculation loop was suppressed (tank bottom effect) and an unstable flow system was observed with no clear recirculation, implying that effective mixing could not achieved.

The results from this work show that mechanically stirred vessels can be effectively operated only within certain ranges of the operating variables without compromising their mixing effectiveness. These operating ranges were quantified. It is expected that this knowledge will help practitioners avoid operating their equipment in regions where the desired mixing effects are not achievable. Furthermore, in this work, the establishment of a previously unreported hydrodynamic regime at critical impeller submergences was described. This regime is not only associated with reducing mixing effectiveness, but can also explain why phenomena such as air entrainment and loss in impeller pumping capacity occur at low H/T ratios.

SINGLE AND MULTIPHASE MIXING IN PARTIALLY FILLED STIRRED VESSELS

by
Shilan Motamedvaziri

A Dissertation
Submitted to the Faculty of
New Jersey Institute of Technology
in Partial Fulfillment of the Requirements for the Degree of
Doctor of Philosophy in Chemical Engineering

Department of Chemical, Biological and Pharmaceutical Engineering

January 2012

APPROVAL PAGE

SINGLE AND MULTIPHASE MIXING IN PARTIALLY FILLED STIRRED VESSELS

Shilan Motamedvaziri

Dr. Piero M. Armenante, Dissertation Advisor — Date
Distinguished Professor of Chemical, Biological and Pharmaceutical Engineering, NJIT

Dr. Costas Gogos, Committee Member — Date
Distinguished Research Professor of Chemical, Biological and Pharmaceutical Engineering, NJIT

Dr. Basil Baltzis, Committee Member — Date
Professor of Chemical, Biological and Pharmaceutical Engineering, NJIT

Dr. Norman Loney, Committee Member — Date
Professor of Chemical, Biological and Pharmaceutical Engineering, NJIT

Dr. Maziar Kakhi, Committee Member — Date
Staff Fellow, U.S. Food and Drug Administration

BIOGRAPHICAL SKETCH

Author: Shilan Motamedvaziri

Degree: Doctor of Philosophy

Date: January 2012

Undergraduate and Graduate Education:

- Doctor of Philosophy in Chemical Engineering,
  New Jersey Institute of Technology, Newark, NJ, 2012

- Bachelor of Science in Chemical Engineering,
  Isfahan University of Technology, Isfahan, Iran 2001

Major: Chemical Engineering

Presentations:

Shilan Motamedvaziri and Piero M. Armenante, "Effect of Impeller Submergence on Flow Characteristics and Minimum Agitation Speed for Solids Suspension in Partially Filled Stirred Vessels", AIChE Annual Meeting, Minneapolis, MN, October 2011

Shilan Motamedvaziri, Sandra Lazo and Piero M. Armenante, "Flow Regimes, Induced Air Entrainment and Power Dissipation in Partially Filled Stirred Vessels at Different Fill Ratios", AIChE Annual Meeting, Minneapolis, MN, October 2011

Shilan Motamedvaziri and Piero M. Armenante, "Single and Multiphase Mixing in Partially Filled Stirred Vessels Using Computational Fluid Dynamics and Particle Image Velocimetry", AIChE Annual Meeting, Salt Lake City, UT, November 2010

Shilan Motamedvaziri and Piero M. Armenante, "Analysis of Single Phase Mixing in Stirred Vessels with Low Height-to-Tank Diameter Ratio Using Computational Fluid Dynamics and Particle Image Velocimetry", AIChE Annual Meeting, Nashville, TN, November 2009

Yueyang Shen, John Bryndza, Shilan Motamedvaziri and Boris Khusid, “Controlled Deposition of Drops on Edible Film Using an AC-Electric Field” APS Annual Meeting, San Antonio, Texas, November 2008

Yueyang Shen, Shilan Motamedvaziri and Boris Khusid, “AC Electric Field Drop-on-Demand Printing of Drug Dosage” AIChE Annual Meeting, Philadelphia, PA, November 2008

to my wonderful family,
for their heartwarming support throughout my life

to my great husband,
for his love, support and encouragement.

AKNOWLEDGEMENT

I am deeply indebted to my advisor Professor Piero Armenante not only because of providing me with a tremendous amount of advisement but also for his support over the past three and half years. I consider myself quite fortunate to have known him. Special thanks are given to the committee members: Professor Basil Baltzis, Professor Costas Gogos, Professor Norman Loney and Dr. Maziar Kakhi for their time, comments and instrumental cooperation.

Moreover, I would like to also thank all my lab-mates in the Mixing Lab, room 312 in Tiernan hall. Very special thanks go to Dr. Giuseppe Di Benedetto, Dr. Micaela Caramelino and Nonjaros Chomcharn for their continuous assistance over the course of this research.

Finally, I would like to thank the Otto H. York Department of Chemical, Biological and Pharmaceutical Engineering for providing me with financial support in pursuit of this degree.

TABLE OF CONTENTS

TABLE OF CONTENTS
(Continued)

TABLE OF CONTENTS
(Continued)

TABLE OF CONTENTS
(Continued)

Chapter **Page**

LIST OF TABLES

LIST OF FIGURES

LIST OF FIGURES
(Continued)

LIST OF FIGURES
(Continued)

LIST OF FIGURES
(Continued)

LIST OF FIGURES
(Continued)

Figure **Page**

NOMENCLATURE

α_A	Volume fraction of air phase in each cell (-)
α_w	Volume fraction of water phase in each cell (-)
C	Distance from bottom of the impeller disk and tank bottom (m)
c and c'	Mean component and fluctuating component of tracer mass concentration (kg/m^3)
C_1, C_2, σ_k, σ_ε	Empirical constants for the k-ε turbulence model (-)
C_b	Distance from bottom of the impeller blades and tank bottom (m)
C_b/T	Impeller off-bottom clearance ratio (-)
C_μ	Constant, except for realizable k-ε turbulence model (-)
C_T	Distance from top of the impeller blades and tank bottom (m)
D	Impeller Diameter (m)
D_m	Molecular diffusion coefficient (m^2/s)
ε	Local rate of dissipation of turbulence kinetic energy per unit volume (m^2/s^3)
E_D	Eddy diffusivity (kg/(m.s))
Fr	Froude Number (-)
$Fr_{flooding}$	Froude number at which impeller flooding starts (-)
g	Gravitational acceleration (m/s^2)
Γ	Torque (Nm)
H	Maximum liquid level (m)
H/T	Fill ratio (-)
H_c	Critical maximum liquid level (m)

NOMENCLATURE
(Continued)

k	Turbulence kinetic energy (m^2/s^2)
μ_t	Turbulent viscosity (kg/m.s)
ν	Kinematic viscosity (m^2/s)
N	Agitation speed (rpm)
N_E	Agitation Speed at Onset of Air Entrainment (rpm)
N_{js}	Minimum Agitation Speed for Solid Suspension (rpm)
N_Q	Pumping Number or Flow Number (-)
N_{Qr}	Radial Pumping Number (-)
t_uN	Global mixing time (-)
P	Instantaneous power dissipated by the impeller (J/s)
P	Pressure (pa) in Navier-Stokes equation
Po	Power Number (-)
Q	Total discharge flow rate from or inward flow rate toward impeller (m^3/s)
Q_r	radial discharge flow rate from impeller (m^3/s)
R	Tank reduce (m)
ρ	Liquid density (kg/m^3)
Re	Reynolds Number (-)
ρ_p	Particle density (kg/m^3)
S_b	Impeller submergence (distance from bottom of the impeller blades to the air-liquid interface (m))
S_b/D	Impeller submergence ratio (-)

NOMENCLATURE
(Continued)

S_{bc}	Critical impeller submergence (m)
S_d	Impeller submergence (distance from bottom of the impeller disk to the air-liquid interface (m))
σ_t	Turbulent Schmidt Number (-)
T	Tank Diameter (m)
t_u	Mixing time required to achieve a desired level of uniformity of U (sec)
U	Desired level of uniformity (-)
u, $\bar{u}$ and u′	Fluid velocity magnitude, mean velocity and Fluctuating velocity (m/s)
U_{tip}	Impeller tip velocity (m/s)
V	Total volume of the liquid inside the tank (m^3)

ABBREVIATIONS

DL Regime	A "double loop" recirculation flow in stirred tanks
CFD	Computational Fluid Dynamics
DT	Disk Turbine
LI	Light intensity
MRF	Multiple reference frames
FS	Flat surface (air-liquid interface)
NC Regime	No recirculation flow in stirred vessels
PIV	Particle Image Velocimetry
RKE	Realizable k-ε turbulence model
SKE	Standard k-ε turbulence model
SL-dp Regime	A "single loop-downpumping" recirculation flow in stirred vessels
SL-up Regime	A "single loop-uppumping" recirculation flow in stirred vessels
t_{BR}	Batch recirculation time
VOF	Volume of Fluid

CHAPTER 1

INTRODUCTION

1.1 Background

Mixing of liquids and dispersed-phase systems is a very common operation encountered in the pharmaceutical industry as well as in many other industries. The development and utilization of mixing technologies is critical to a variety of industrial applications, since different types of mixing-related phenomena are often the preliminary requirement for, or an integral component of, other operations, such as reaction or crystallization.

In the industrial practice, mixing of liquids in the presence or absence of a separate phase, such as finely divided solids, is often conducted in cylindrical, baffled tanks stirred by mechanical agitators. One of the key issues associated with a more fundamental understanding of mixing phenomena in such systems is the quantification of the hydrodynamics behavior of the mixing system itself, since the hydrodynamics of mixers is typically quite complex. Over three decades, researchers have studied the velocity distributions in agitation vessels using a number of approaches including experimental techniques such as Particle Image Velocimetry (PIV) and Laser-Doppler Velocimetry (LDV), and computational techniques such as Computational Fluid Dynamics (CFD). These methods have been essential to investigate a number of complex phenomena in mixing vessels (Yianneskis et al. 1987; Armenante et al. 1996; Armenante et al. 1997; Sheng et al. 2000; Montante et al. 2001; Campolo et al. 2002; Akiti and Armenante 2004; Yeoh et al. 2004; Deglon et al. 2006; Murthy and Joshi 2008).

Efforts have also been concentrated on the determination of the roles of key variables on the establishment of different flow regimes in mixing tanks. Different

macroscopic flow patterns (flow regimes) are commonly observed in stirred tanks depending on the impeller type and a number of geometric parameters. The occurrence of a given flow pattern in stirred tanks has a significant impact on the process carried out in the mixing system. For instance, a typical radial impeller placed in a cylindrical vessel filled with a low viscosity liquid typically produces a “double-loop” recirculation flow, where the fluid flow forms two loops, one above and the other below the impeller. However, if the impeller clearance off the bottom of the tank is reduced, flow pattern transition eventually (and suddenly) occurs at a critical impeller clearance value, and the lower recirculation loop is suppressed as a result. This double-loop to single-loop transition was first described by Nienow (1968) and its importance on processes carried out in stirred tanks such as solid suspension behavior was investigated by a number of investigators, such as Ibrahim and Nienow (1996, 1999), Armenante et al. (1998) and then by Montante et al. (2001), Ochieng et al. (2007) and Li et al. (2011) who also computationally simulated this flow transition.

The overall flow pattern in mixing tanks and the changes that are introduced when geometric and operating variables are varied have a strong impact on different mixing phenomena and mixing parameters, which, in turn, have a significant effect on the process carried out in the mixing system. One of the most important variables in the description of mixing phenomena is the non-dimensional power number, Po, which quantifies the power dissipated by the impeller. The power dissipated by the agitation system is fundamental to any mixing process since energy is needed to homogenize the vessel content, disperse immiscible phases, suspend solids, increase mass transfer, and, in general, produce the desired mixing effect.

The pumping capacity of an impeller, i.e., the flow rate generated by the impeller during its operation, is another important characteristic of the impeller. Usually the pumping capacity is expressed in terms of another important non-dimensional number, i.e., the Pumping Number (or Flow Number) N_Q. Different types of impellers produce different pumping actions which cause the establishment of fluid flow circulation patterns inside the tank.

Power consumption and pumping capacity of the impeller depend not only on the type of impeller used, the agitation speed, and the physical properties of fluid but also on the geometric characteristics of the system (such as impeller clearance, liquid height, or liquid head above the impeller) that produced different flow regimes (Rushton et al., 1950; Yianneskis et al., 1987; Dyster et al., 1993; Lane and Koh, 1997; Patwardhan et al., 1999; Murthy and Joshi, 2008; Yang and Takahasi, 2010). This topic has been the subject of significant work. For example, Mahmoudi et al. (1992) investigated the effect of the impeller position on mixing time when the process undergoes different flow patterns. Rutherford et al. (1996) and Chapple et al. (2002) studied the effect of the impeller dimension on mixing characteristics such as power and pumping number. Zhao et al. (2011) studied the flow characteristics for different impeller types and spacing. They have reported that global flow pattern was strongly depended on impeller spacing which produced different mixing efficiencies.

In addition, other less easily quantifiable phenomena are also critical for the success of very common mixing operations, such as the effect of the intensity and the characteristics of the flow pattern in the lower portion of the vessel on the attainment of the complete suspension of solids off the tank bottom. Suspension of solid particles is a

complex phenomenon caused by strong turbulent disturbances near the tank bottom which can lift the particles upwards, combined with a sufficiently high average velocity field "sweeping" the tank bottom and distributing the particles in other regions of the vessel (Baldi et al. 1978). Therefore, the vessel configurations and impeller types and geometries that generate stronger turbulence near the bottom of the vessel are typically capable of suspending solids at lower agitation speeds, often with lower energy consumption.

Of particular relevance for the work to be conducted in this investigation is the suspension of solid particles in a liquid in an agitated vessel. In the past the minimum agitation speed for complete off-bottom solid suspension, N_{js}, has been experimentally determined (Nienow, 1968; Baldi et al., 1978; Armenante et al., 1992; Ibrahim and Nienow, 1996, 1999; Armenante et al., 1998; Kasat et al., 2005; Sardeshpande et al., 2009; Brucato et al., 2010; Collignon et al., 2010 and Tamburini et al., 2011) and then correlated with a number of operating variables (Zwietering, 1958; Armenante et al., 1998). These are both geometric variables (e.g. impeller type, size, position, and tank diameter), and physical variables (e.g. density difference between the solids and the liquid, liquid viscosity).

The effect of the intensity and the characteristics of the flow pattern near air-liquid interface are also important for a number of processes such as for the case of surface air entrainment (Bhattacharya et al., 2007; Malli et al., 2009). Impeller types, geometric (such as liquid head above the impeller, S_b) and operating variables that produced up-pumping flow have more tendencies toward ingesting air bubbles from the air-liquid interface since producing stronger velocity filed close to air-liquid interface.

For a constant flow pattern, researchers have reported that when the impeller submergence decreases surface air entrainment is observed at a lower agitation speed (Bhattacharya et al., 2007).

While air entrainment is beneficiary for processes such as wastewater treatment, it could produce serious problems in others, such as suspension polymerization. Therefore, N_E (the minimum agitation speed which adds sufficient energy to the stirred tank to entrain bubbles into the vessel) is an important operational limit. One of the mechanisms that has be reported in the literature to responsible for the gas entrainment, and an important one for the work conducted here, is the engulfment of gas bubble caused by turbulent velocity fluctuations at the free interface between the stirred liquid and the gas phase above it (Bhattacharya et al., 2007).

Up-pumping flow impellers have a significant tendency toward ingesting air bubbles from the air-liquid interface and facilitating surface air entrainment. When this occurs, the impeller may incorporate enough air in the liquid to compromise its pumping effectiveness. Ultimately, this phenomenon may result in impeller flooding, a condition observed in gas-liquid systems (where a gas is sparged below the impeller), when excessive bypassing of the gas bubbles occurs around the impeller and the impeller agitation speed is not enough to disperse them through the vessel. When flooding occurs the impeller power dissipation is reduced drastically. In addition, a stirred vessel under flooding condition loses its capability of providing adequate gas hold-up and liquid pumping, and thus gives poor process result (Paul et al., 2004). Therefore, it is important to determine the operating conditions under which flooding occurs in order to avoid them (Paul et al., 2004; Wang et al., 2006).

In the pharmaceutical and fine-chemical chemical industry, mixing vessels and reactors are not only often encountered, but are also operated in a variety of configurations. Typically, such vessels are utilized a full capacity, with implies that the liquid level is the maximum practically achievable in the system without overflowing it. In vessels in which the tank diameter T is the same or similar in size to the vessel height the liquid height H is typically similar or larger than the tank diameter, i.e., H/T=1 or H/T>1. It is therefore unsurprising that the systems for which H/T=1 have been extensively studied. Mixing studies have been conducted in homogeneous systems with H/T=1 to determine, among the others, the velocity distribution of the liquid inside the vessel, the power dispersed by the impeller, and the mixing time. Multiphase systems have also been investigated to determine, among others, the minimum agitation speed for complete dispersion of a second or even third phase in the liquid, including finely dispersed solids, immiscible liquids, and sparged gases. Although some areas have been investigated more than others, a significant body of literature exists on many such aspects of mixing in single, two, and three phase systems for which H/T=1.

1.2 Mixing in Partially Filled Vessels (H/T<1)

As already mentioned above, most of the mixing research conducted so far and reported in the literature addresses a number of different issues related to mixing in vessels for which H/T is equal to or larger than one. However, there are many instances where this ratio is lower than 1, as in all those cases in which the vessel is being filled or emptied. It is clearly desirable to maintain a sufficient agitation level even when H/T<1 in order to attain the process objectives.

It is often the case that stirred reactors and vessels operating at low H/T levels are also operating in batch mode, especially in the fine chemical and pharmaceutical industry. There are number of reasons why batch systems are used. In general, batch processes are suitable for small-scale production, for processes where a range of different products or grades is to be produced in the same equipment (i.e., when multi-purpose reactors are used), and in cases where reactions require long reaction times. In addition, quality control is easier to implement in a batch system since the product quality can be checked at the end of the batch. For all these reasons, batch processes have been and still are very commonly used in industry (Horowitz, 2010). However, batch operations have their own challenges such as consistency from one batch to another, and consistent output from a batch stirred vessel or reactor when this system is used to feed another system. In addition, there are some very common situations in which used partially filled stirred vessels have to be operated satisfactorily including:

i. adding ingredients to a compounding tank. A vessel is charged with different components to eventually achieve the desired composition of the final product. All component must be well mixed, even at low H/T values;
ii. dispensing a product from a vessel. A vessel, initially filled with a suspension or a dispersion of another phase, is used to in a filling line. All bottles must contain the same ingredients in the same ratios, i.e., full dispersion of the dispersed phase must be maintained under a variety of operating conditions for the feed tank;
iii. charging or empting a vessel during different steps of a manufacturing process;
iv. full recovery of expensive raw materials and products from the vessel;
v. minimization of waste products.

In all these cases, the vessel must be satisfactorily operated at different H/T ratios and under conditions in which the vessel is partially filled (i.e., H<T). Therefore, it is critical to maintain the proper level of agitation at all times in order to satisfy the mixing requirements of the process (e.g., solids suspension) or at least to be able to determine the operating regions in which the vessel can perform satisfactorily as far as mixing is concerned.

When the impeller submergence is reduced as a result of lowering the liquid level, the fluid dynamics of even a single-phase stirred liquid can become quite complex, with different regimes possibly existing depending on the geometric characteristics of the system (such as impeller clearance, liquid height, or liquid head above the impeller). Little information is available in the literature on the effect of H/T (when H/T<1) on liquid mixing and hydrodynamics, and the attainment of the off-bottom suspension of dispersed solids in agitated liquids. Therefore, significant work still remains to do to understand how mixing vessels operate at low fill ratios, i.e., for H/T<1.

1.3 Objectives of this Work

The objectives of this work were to study in detail the hydrodynamic changes that occur when H/T is decreased, and to determine the minimum liquid levels and the critical impeller submergence for different impeller off-bottom distances, impeller diameters and agitation speeds where adequate mixing objectives can still be achieved, both in a single liquid phase and in solid-liquid suspensions. More specifically, the focus of this work was on the characterization of the fluid dynamics and the different fluid flow regimes that can be observed in such systems when the impeller submergence is reduced as a result of

lowering the liquid level and how theses flow regimes affect the mixing performance of the agitation system.

Flat-bottomed, baffled vessels (5L, 12L, 20L and 170L) equipped with a single disk turbine (DT) of 4 different sizes with 5 different impeller off-bottom clearances were used here to study the system's hydrodynamics and related mixing phenomena. A number of experimental tools were used in this work to analyze the systems under investigation, including: Particle Image Velocimetry (PIV) for the experimental determination of the velocity profiles (including the fluctuating component), and after the appropriate data manipulation, the impeller pumping capacity and its pumping number; a colorimetric system coupled with image processing to quantify mixing time; a strain gage-based rotary torque transducer system to measure the power dissipated by the impeller; and a visual observation method to determine the minimum agitation speed for complete solids suspension, N_{js}. In addition, Computational Fluid Dynamics (CFD) modeling was used to predict the behavior of the system in terms of its velocity profile, Power Number, Pumping Number, and mixing time. CFD predictions were obtained using both a multiple reference frame (MRF) model coupled, when needed, with a Volume of Fluid (VOF) model, in order to study systems in which a vortex could be expected to form.

The work carried out in this investigation consists of different specific components aimed at studying different aspects of single and multiphase mixing in batch stirred vessels with low H/T ratios, including the following:

1. Determination of the effect of the impeller submergence ratio S_b/D, and consequently the fill ratio H/T, in stirred vessels with a single liquid phase for different impeller clearance-to-tank diameter ratios, and impeller diameter-to-tank diameter ratios:
    i. Determination of the velocity distribution, pumping rate, power, Power Number, and Pumping Number at different S_b/D ratios and different agitation speeds. This component of the work was carried out using both computational and experimental techniques, and was focused on the determination of the flow pattern, flow pattern transition and the distribution of velocity and turbulent intensity inside the vessels as the above-mentioned geometric and dynamic parameters were varied. The results of this portion of the worked identified the set of values of the geometric parameters that resulted in sudden changes of flow regime in the system for $H/T \leq 1$, and the role that dynamic variables such as agitation speed play in the entrainment of surface air into the liquid in the vessel;
    ii. Determination of the velocity distribution, pumping rate, power, Power Number, and Pumping Number at different S_b/D ratios for different combination of impeller off-bottom clearances, impeller diameters, and agitation speeds. This component of the work was carried out using the same computational and experimental tool mentioned above and resulted in the determination of a phase diagram for the existence of different regimes in which the system can be operated.
    iii. Experimental determination and computational prediction of mixing time for different S_b/D ratios. This component of work was important to determine for

which values of the geometric variables macromixing time changed drastically and how flow regime transitions affected the mixing time.

2. Determination of the effect of impeller submergence ratio S_b/D on minimum agitation speed to complete off-bottom solid suspension, N_{js} for stirred vessels with different impeller clearances, vessel and impeller diameters:

    i. Determination of N_{js} experimentally under different operating conditions. It is important to characterize how flow pattern transitions affected solid-suspension behavior and more important to determine for which values of the geometric variables solid suspension will be unattainable. These experimental results are also important in the validation of the CFD results and the prediction of changes in the flow pattern corresponding to the inability to attain solid suspension.

    ii. Development the set of conditions (geometrical and dynamic parameters related to the mixing system and particle size and density) under which solid suspension becomes unattainable.

In conclusion, in this work the role that key geometric and dynamic parameters play that result in different operating regimes for vessels operated under partial fill ratio conditions were determined and quantified. It is expected that the knowledge developed in this work will help practitioners properly operate their equipment in regions where the desired mixing effects can be achieved.

CHAPTER 2

EXPERIMENTAL APPARATUS, MATERIALS AND METHODS

2.1 Agitation System

The experimental apparatus, shown in Figure 2.1, consisted of one of several baffled, cylindrical, transparent, Plexiglas mixing tank with a flat bottom, having an internal diameter, T. The tank was provided with four baffles having a width of T/10 and spaced 90° apart extending all the way to the bottom of the tank. The tank was equipped with a single 6-blade disk turbine (DT) impeller having a diameter, *D*. The detailed dimensions of the different vessels and impellers used in this work are shown in Table 2.1 and Table 2.2, respectively.

The impeller was mounted on a centrally placed shaft (shaft diameter: 1.27 cm) coupled to an inline torque transducer (described below) which was in turn connected to a variable-speed motor (Model CG-2033-11; Chemglass Life Sciences, Vineland, NJ). The motor was equipped with a controller to adjust the agitation speed in the range 0-500 rpm and with an rpm-meter, measuring the rotational speed within ±1 rpm. The agitation speed was periodically checked using a digital tachometer (Model HT-4100, Distek, Inc., New Brunswick, NJ). A traversing system supporting the tank was used to change the vertical position of the tank with respect to the impeller in order to vary the impeller clearance off the tank-bottom, C_B, measured from bottom of the impeller to the bottom of the tank.

The liquid medium was always distilled water. For each C_B value the vessel was filled with distilled water at the desired liquid level, *H*. Consequently, the impeller submergence, S_B, i.e., the distance between the bottom of the impeller (bottom of the blades) and air-liquid interface under no-agitation condition, was also varied. Four

different impeller size and tank sizes (5L, 12L, 20L and 170L) with 5 different impeller off-bottom clearances were used here to study the system's hydrodynamics and related mixing phenomena.

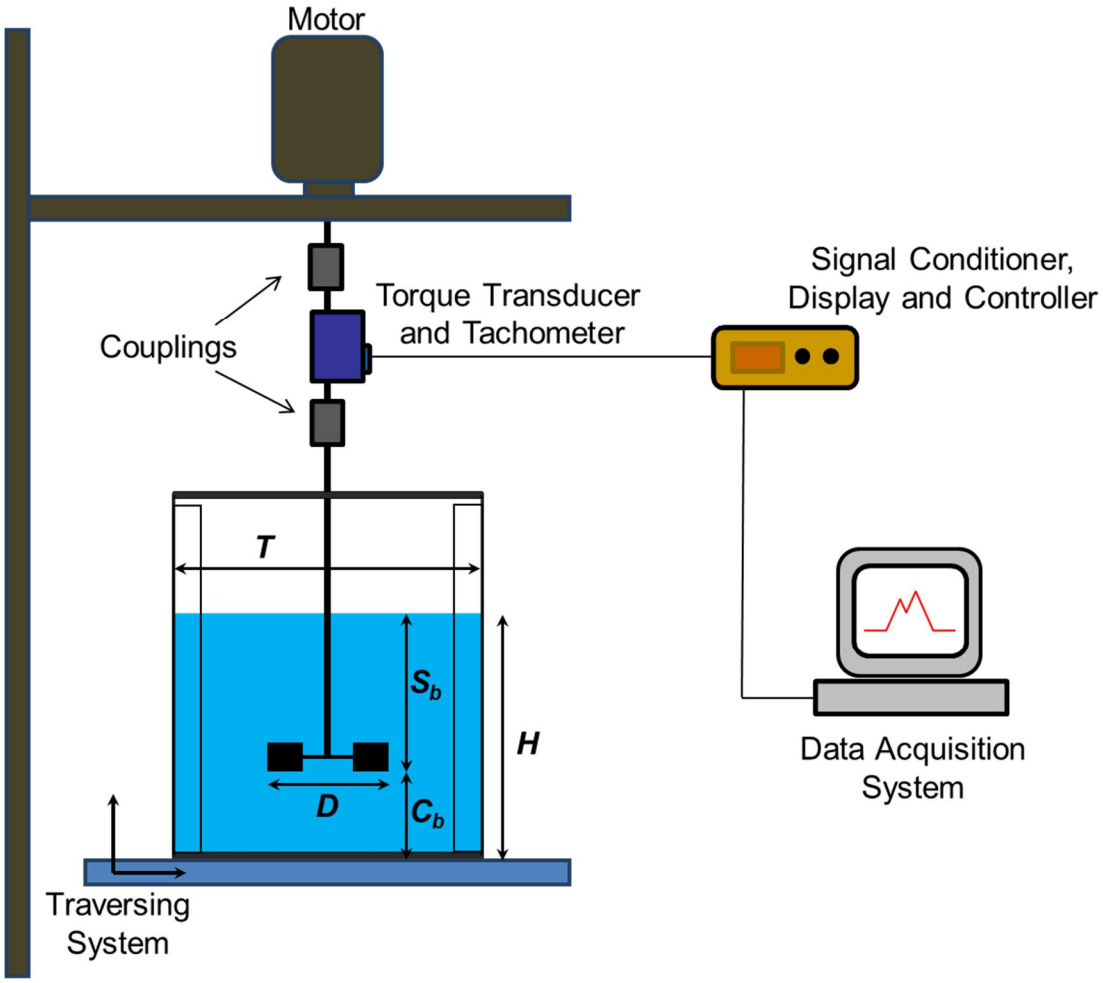

Figure 2.1 Schematic of experimental set-up of agitation system.

Table 2.1 Dimensions of the Vessels used in this Work

Tank No.	Diameter (T) **m**	Height (L) **m**	Baffle Width (W_f) **m**	Baffle Thickness (t_f) **m**
1	0.190	0.23	0.0190	0.0060
2	0.246	0.30	0.0250	0.0072
3	0.294	0.50	0.0290	0.0072
4	0.585	0.600	0.0585	0.0072

Table 2.2 Dimensions of the Disk Turbine Impellers used in this Work

Impeller No.	Diameter (D) **m**	Disk Diameter **m**	Disk Thickness (t_d) **m**	Blade Width (W_b) **m**	Blade Length (L_b) **m**	Blade Thickness (t_b) **m**
1	0.0640	0.0473	0.0020	0.0160	0.0126	0.0015
2	0.0765	0.0575	0.0017	0.0190	0.0154	0.0015
3	0.1026	0.0760	0.0023	0.0190	0.0154	0.0024
4	0.1268	0.0845	0.0026	0.0320	0.025	0.0028

Experiments were carried out at impeller rotational speeds, N, between 50 rpm and 500 rpm. The impeller Reynolds number, defined as $Re=ND^2/\nu$, where N is the impeller speed (rev/sec), and ν is the kinematic viscosity of the water ($\nu= 10^{-6}$ m^2/s), was between 6000 and 10^6, i.e., in the turbulent regime.

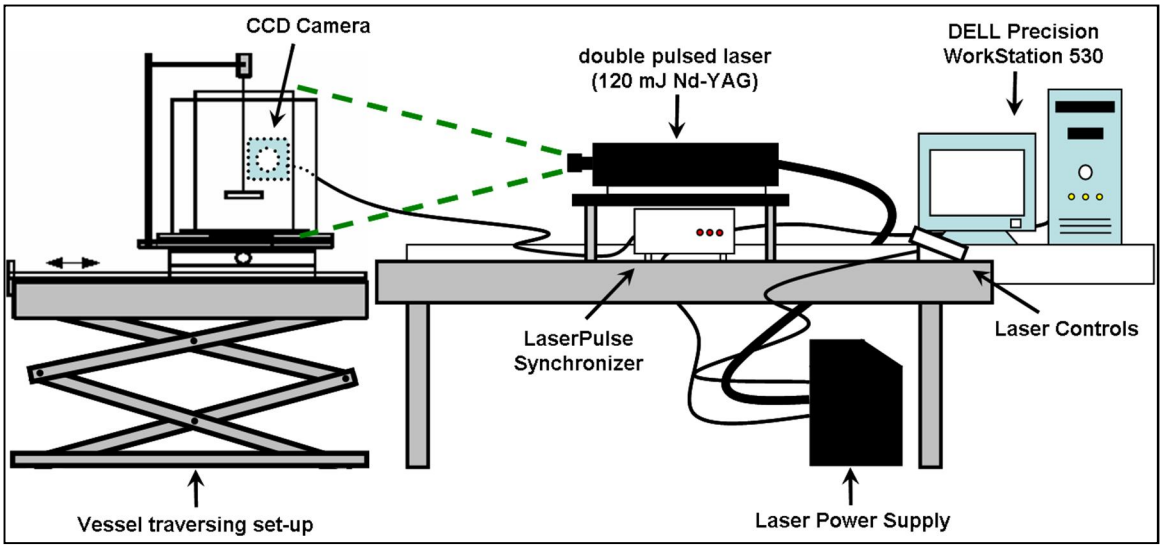

Figure 2.2 Schematic of laboratory PIV experimental set-up

2.2 Experimental Determination of Local Liquid Velocity and Related Variables by Particle Image Velocimetry (PIV)

Particle Image Velocimetry (PIV) is a non-intrusive optical method that can be used to experimentally determine the local fluid velocity within any transparent vessel or other equipment. Accordingly, the fluid is seeded with neutrally buoyant tracer particles with sizes typically between 10 and 100 μm designed to closely follow the liquid flow. A double laser sheet pulse is then used to illuminate the cross section of the equipment under investigation at two different times, spaced apart only by a few hundreds of microseconds. The seed particles scatter the incoming laser light, and two images at the two different times are captured. The frames are split into a large number of interrogation areas (the size of the interrogation area should be chosen to have at least 6 particles per area, on average). Then it is possible to calculate a displacement vector for each interrogation area, based on the light scattered by the particles in that area. This is typically accomplished by using a cross-correlation technique. The signal is converted to a velocity using the time between laser shots and the physical size of each pixel on the

camera. PIV has proven to be a highly effective experimental method for fluid dynamic studies and has been extensively used by several investigators to quantify the flow characteristics of mixing vessels (Sheng et al., 2000; Montante et al. 2001; Li and Bao, 2011; Zhao et al., 2011).

A schematic of the PIV apparatus used in this work is given in Figure 2.2. Actually, two different but similarly operating sets of PIV apparatuses, labeled “PIV1” and “PIV2”, were used here to determine the velocity flow field in the mixing systems. PIV1 is a two-dimensional TSI PIV apparatus (TSI Incorporated, Shoreview, Minnesota, USA) equipped with two individually water-cooled laser heads. PIV2 is a Dantec FlowMap 2D PIV apparatus (Dantec Dynamics A/S, Tonsbakken 16 – 18, DK – 2740 Skovlunde, Denmark) equipped with one laser head. Both PIV systems use a double pulsed 120 mJ Nd-YAG laser (New Wave Research model Gemini PIV 15, Fremont, CA, USA) consisting of two infrared laser heads combined in a single package with a second harmonic generator and two discrete power supplies. This laser is a Class IV laser product, emitting light at a 532 nm wavelength. The power supplies contain safety interlocks which are wired to the doors of the laboratory. The laser produces two pulsed infrared laser beams which pass through an optical arrangement of lenses to generate a laser light sheet. This laser light sheet acts as the photographic flash for the single digital camera (PIV1: PIVCAM 10-30, TSI model 630046; PIV2: Dantec HiSense PIV/PLIF). The laser and the digital camera are connected to a synchronizer (LASERPULSE Synchronizer, TSI model 610034), which is in turn connected to a computer (DELL Precision WorkStation 530). All of these components are controlled by software (PIV1: Insight PIV Software; PIV2: FlowManager Software) on the computer. The software

collects pairs of digitized images from the CCD camera (with the two images in each pair being collected at a small but known time interval), which are subdivided into small subsections called interrogation areas. Each pair of frames for a given interrogation areas is then analyzed using cross-correlation to determine the spacial x-displacement and y-displacement that maximize the cross-correlation function for that interrogation area. The resulting displacement vector obtained by dividing the x- and y-displacements by the time interval is taken as the fluid velocity in that interrogation area.

In the experiments performed here, the water in the vessel was seeded with neutrally-buoyant 10 µm silver coated particles (Dantec Measurement Technology USA, Mahwah, NJ, USA) that can follow the fluid flow pattern very closely. Then, guided by the settings from the software, the synchronizer accepted the trigger dictated by the encoder and proceeded to synchronizing the laser pulses with the capture of appropriate images using the digital camera.

2.2.1 Experimental Determination of Impeller Pumping Flow Rate and Pumping Number

Both radial and axial impellers exert a pumping action within the tank. Different types of impellers produce different pumping actions which cause the establishment of fluid flow circulation patterns inside the tank. The pumping number, N_Q, is used to determine the impeller pumping capacity, which is defined as (Paul et al. 2004):

$$N_Q = \frac{Q}{ND^3} \tag{2.1}$$

In this equation, Q is the flow rate produced by the impeller, N is the agitation speed, and D is the maximum impeller diameter. The pumping action of the impeller results in a discharge flow rate around the impeller, Q_{out}, balanced by incoming flow toward the

impeller, Q_{in}. In principle, the Pumping number could be calculated using either Q_{out} or Q_{in}. since the conservation of mass for an incompressible liquid requires that Q_{out} and Q_{in} be equal. To compute Q for an impeller, an appropriate control volume must be constructed around the impeller. A cylindrical volume around the impeller is a common shape that is used to calculate Q. Ideally the pumping number should be calculated using a cylinder around the impeller with a diameter and height exactly equal to the impeller diameter and blades height. However, acquiring velocity data at that position is impossible by either experimental or computational techniques.

Radial pumping number, N_{Qr} which is calculated based on radial discharge flow rate, Q_r, around the impeller has been reported in this work at different filling ratios. A typical radial impeller (such as Disk Turbine) placed in a cylindrical vessel filled with a low viscosity liquid typically produces a "double-loop" recirculation flow, where the fluid flow forms two loops, one above and the other below the impeller. For this kind of flow pattern Q_{out} around impeller is the same as the radial flow out, Q_r, from the side surface of the cylinder. Therefore N_Q for such a system is equal to N_{Qr}. However, N_Q and N_{Qr} might be different for other impeller types (such as axial impeller) since they produce different types of flow pattern.

In this work, the radial velocities measured by PIV along a vertical segment (rake) close to the impeller blades were used to calculate Q_r. This rake contained 7 points and it was 0.38 cm away from impeller blades in radial direction (r/R=0.34, knowing that vessel radius, R, was 12.3 cm and impeller radius, R_{imp}, was 3.83 cm). The rake began 0.38 cm below the blades and ended 0.38 cm above the blades (z_1/T=7.2 cm and z_2 = 9.3 cm,

knowing that blades extend vertically from 7.5 cm to 9.04 cm from the tank bottom). The following equation was used to calculate Q_r:

$$Q_r = \sum_{i=1}^{i=6} \overline{u}_{ri}(r, \overline{z}_i)\Delta z_i 2\pi r \tag{2.2}$$

where $\overline{u}_{ri}(r, \overline{z}_i)$ is the average of the radial velocities measured by PIV at z_i ($u_{ri}(r, z_i)$) and z_{i+1} ($u_{r(i+1)}(r, z_{i+1})$). $u_{ri}(r, z_i)$ were the average of the radial velocities of 200 PIV measurements at any given r and z_i. Since the PIV data were taken at any position of the impeller relative to the baffles, the average velocity obtained via PIV could be taken as the average of any point along a circle with a radius r and axial level of z_i (circumferential average). After computing the appropriate average radial velocity, this value was multiplied by the elemental surface area ($\Delta z 2\pi r$) of the cylinder surrounding the impeller where the measurements were taken (with Δz and r equal to 0.35 cm and 4.2 cm, respectively).

2.2.2 Experimental Determination of Impeller Discharge Angle

The impeller discharge angle is defined as the angle formed between the average vector of the discharge stream produced by the impeller and the horizontal plane. The impeller discharge stream angle was calculated by taking the average angle of the velocity vectors on the previously mentioned rake but only over the blade height. In this work, the radial and axial velocity components measured by PIV along a vertical rake close to the impeller blades were used to calculate impeller discharge angle. This rake contains 5 points and it was 0.38 cm away from impeller blades in the radial direction (r/R=0.34). Its

vertical length was equal to the impeller blade height (z_1=7.5 cm and z_2 = 9.04cm). Positive angles indicate that the stream is flowing upward.

2.3 Experimental Determination of the Impeller Power Dissipation and Power Number

The motor was mounted on a separate steel framework above the tank, as shown in Figure 2.1, in order to minimize vibrations that could have affect torque measurement. Appropriate couplings were carefully selected to mount the transducer on the shaft between the motor and the impeller in order to minimize wobbling of the impeller shaft. This arrangement prevented the introduction of friction sources in the torque measurement, as reported in other systems (Chapple et al., 2002).

The torque,Γ applied to the impeller by the motor was experimentally measured with a strain gage-based rotary torque transducer (Model, T6-5-Dual Range, Interface, Inc. Scottsdale, AZ) connected to an external multi-channel signal conditioner, display and controller (Model 9850). The transducer operated by producing an output voltage, proportional to the applied torque, which was generated by the change in electric resistance within the strain gages. The strain gages bonded (Model DCVA) to the torque sensor structure within the transducer. The magnitude of the resistance change was proportional to the deformation of the torque sensor and therefore the applied torque. In this apparatus, the controller was used to feed the torque transducer with a supply DC voltage, which was converted to AC in the transducer stator, transferred inductively to the transducer rotor electronics, rectified, stabilized, and fed to the strain gage bridge also contained within the rotor. The output from the bridge was conditioned in an amplifier, converted to a digital signal, and transferred back to the stator by a rotating transformer.

The transducer could measure the torque applied to the rotating shaft in two different ranges, i.e., 0-0.5 Nm and 0-5 Nm. However, only the first range was used in this work. The torque measurement error was ±0.1% of full scale. The same instrument could also measure the agitation speed, N, and then internally calculate and display the instantaneous power delivered, P, by the shaft, according to Equation 2.3.

$$P = 2\pi N\Gamma \tag{2.3}$$

The controller utilized its own software (M700) to interface with a computer, which was used for data acquisition, storage, and post processing. The data acquisition rate was 100 Hz.

Before collecting experimental torque data, the torque transducer was statically calibrated by blocking the motor and then mounting on the shaft, below the transducer, an arm extending perpendicularly to the shaft, which pushed on a dynamometer (Shimpo Digital Force Gauge, Model FGV-0–5XY, Cole-Parmer, IL), placed perpendicular to the arm. The torque calculated by multiplying the dynamometer force display by the length of the arm was compared with the torque measured by the torque transducer. The agreement was always within ±3%.

The experimental power dissipation was measured for different combinations of liquid level, impeller size, vessel size, impeller clearance, and agitation speed. In all experiments (conducted at least in duplicate), the system was allowed to stabilize for 2 minutes before collecting power data in 20 s time intervals. Equation 2.4 was used to obtain the experimental power number, Po.

$$Po = \frac{P}{\rho N^3 D^5} \tag{2.4}$$

where ρ is the liquid density.

2.4 Experimental Determination of Mixing Time

Mixing time can be defined as the time required achieving a pre-defined level of homogeneity when a tracer is added to a mixing system. If a miscible tracer is added to a homogenous liquid in an agitated vessel the local concentration, measured with an appropriate detector, fluctuates with time. Mixing time is the time it takes the tracer-liquid system to reach a desired (and pre-defined) level of uniformity.

The mixing system shown in Figure 2.1 was used also here to perform mixing time experiments. Mixing time was determined by analyzing a de-colorization reaction through image analysis when 95% uniformity was achieved. The strong acid (HCl) and base (NaOH) reaction was used. The base (3 mL of a 1.0 mol/L NaOH solution) was introduced into the tank together with the indicator (phenolphthalein, 10 drops) before the experiment started, while the acid (4.5 mL of a 1.0 mol/L HCl solution) was injected into the tank at the beginning of each experiment. The injection point was selected to be midway between two baffles, midway between the shaft and tank wall, and approximately 0.7 cm below the air-liquid interface. The injection was reproducible and the injection time was no longer that five seconds. The acid-to-base ratio was kept constant and equal to 1.5 in every experiment, so that the macro-mixing time could be measured.

The addition of the acid resulted in a pH change that was displayed by a color change of the indicator from pink to colorless. The color change was used to determine the mixing time. Digital images were recorded with a CCD camera (30 images/sec – 300 dpi x 300 dpi resolution). Each image was analyzed to determine the light intensity for a number of pixels at each time using the MATLAB Image Analysis Toolbox. Image analysis of the whole system was utilized because it overcomes the problems associated

with the measurement of a local mixing variable (i.e., concentration or conductivity) at just one or a few points in the mixing system via the introduction of probes at different locations. In addition, image analysis avoids the subjectivity problem usually associated with some of these methods.

2.5 Experimental Determination of the Minimum Agitation Speed for Solid Suspension, N_{js}

In solid-liquid suspension studies, the most critical agitation speeds that is usually measured is the minimum agitation speed required to "just suspend" all the finely divided solid particles, N_{js}. As in most previous studies, N_{js} was measured visually in this work. Accordingly, N_{js} was obtained using the method described by Zwietering (1958), i.e., a suspension is considered to have achieved the just-suspended state if no particles remain at rest on the bottom of the tank for longer than 1-2 sec. A mirror placed at 45 under the tank is used for the visual observation and a lamp of 150 watts is used to illuminate laterally the tank bottom. Spherical glass particles (Arthur S. La Pine & Company, Chicago,IL) were used. These particles had a 149.6-μm mean particle size, a particle size distribution range of 116.8-179.4 μm and a density of 2500 kg/m^3 (ρ_s). The laser diffraction instrument used for particle size measurement, Beckman-Coulter LS230 (Beckman Coulter, Inc., Fullerton, CA, USA). Their mass fraction (Φm) in the liquid in the tank was and 0.5%.

2.6 Experimental Determination of the Agitation Speed at Onset of Air Entrainment, N_E

N_E can be defined as the minimum agitation speed that results in sufficient surface entrainment of air bubbles into the vessel. N_E was determined by observing the number

of bubbles that were entrained into liquid in the vessel and that remained there. The experimental method described by Bhattacharya et al. (2007) was used in this work to measure N_E.

When the agitation speed was changed, the amount of bubbles entrained into the vessels changed as follows:

i. at very low impeller speed there were no bubbles inside the tank ($N<<N_E$)
ii. when the agitation speed was increased the air-liquid interface movements began to move and few bubbles were entrained into the system although the number of bubbles that permanently remained inside the vessel were negligible ($N< N_E$)
iii. when the agitation speed was further increased the air-liquid interface movements became stronger and more bubbles became entrained into the liquid and were distributed inside the tank ($N \sim N_E$)
iv. when the agitation speed was increased ever further the air-liquid interface movements were much stronger and many more bubbles became entrained into the system (gas holdup became large) and the bubbled distributed themselves inside the tank ($N >N_E$)

When N_E was determined, then the agitation speed decreased for 40 rpm and increased by 10 rpm to obtain a better estimate of N_E.

CHAPTER 3

COMPUTATIONAL FLUID DYNAMICS AND COMPUTATIONAL DETERMINATION OF MIXING VARIABLES

Computational Fluid Dynamics (CFD) is a computational tool designed to solve the momentum and mass balance equations under laminar or turbulent regimes to predict the flow field in complex geometries such as mechanically stirred mixing vessels.

In this work, numerical simulations of the velocity distribution and turbulence levels inside the stirred tank equipped with a single disk turbine were conducted using a commercial pre-CFD mesh generator (Gambit 2.4.6) coupled with a CFD software package (Fluent 6.3.26). For the first set of simulations, the full 360˚-tank geometry was modeled. In order to improve the simulation through the use of a structured mesh with smaller cells, periodic boundary conditions were also used in which only the 180˚-tank geometry was incorporated. The use of periodic boundary conditions and hence the need to simulate only half of the tank is much less computationally intensive.

3.1 Mesh

The exact geometry of each component of the system (such as the Plexiglas vessel, impeller, shaft, baffle, etc.) was obtained by measuring the actual dimensions with a caliper (Table 2.1 and Table 2.2). The geometry data then were inserted in the mesh generator, which was used to partition the domain into a set of discrete sub-domains to obtain the exact shape of the volume in which the numerical CFD simulations were conducted. Attention was paid to generate high quality meshes since this has a direct impact on the simulation results. In order to achieve a high quality mesh the domain was typically divided in different sub-volumes and different type or meshes were assigned to

each volume separately. Figure 3.1 and Figure 3.2 show the two different mesh constructing strategies that were used in this work. A mesh constructed by hexahedral cells was used in the entire domain for the first case. In this case, the entire domain was divided into 270 sub-volumes to achieve higher mesh qualities. In the second case, a tetrahedral-cell mesh around impeller and hexahedral-cell mesh in the rest of the domain were used (Figure 3.2); the entire domain was divided into 40 sub-volumes. The Equisize Skew parameter was used to quantify the quality of the mesh. The value of this parameter can be between 0 and 1: the lower the value, the higher the quality. The value of these parameters is preferred to be less than 0.9, possibly less than 0.85. 97% of the grids in Figure 3.1 had an Equisize Skew value less than 0.1 and only 0.02% of the grids had a value between 0.5 and 0.6. Thus the quality of the meshes was high. 75% of the grids in Figure 3.2 had an Equisize Skew value less than 0.1 and in 0.3% of the grids this value was between 0.7 and 0.8. Comparing these two methods led to these conclusions: (1) constructing a mesh based on the first method (Figure 3.1) required significant attention since the domain needs to be divided into many smaller sub-volumes, compared to meshes based on second method (Figure 3.2); (2) although the first method produced better mesh quality compared to the second method, the second method produced meshes that met our expectation. Since the goal in this research was to simulate different geometries of a stirred vessel (such as different liquid levels, impeller positions, and impeller sizes) an easier and less time consuming strategy for CFD simulation was preferred. Therefore, the second method of meshing was used in most of the simulations. It is important to note that this decision has been made after comparing the hydrodynamic results from both methods.

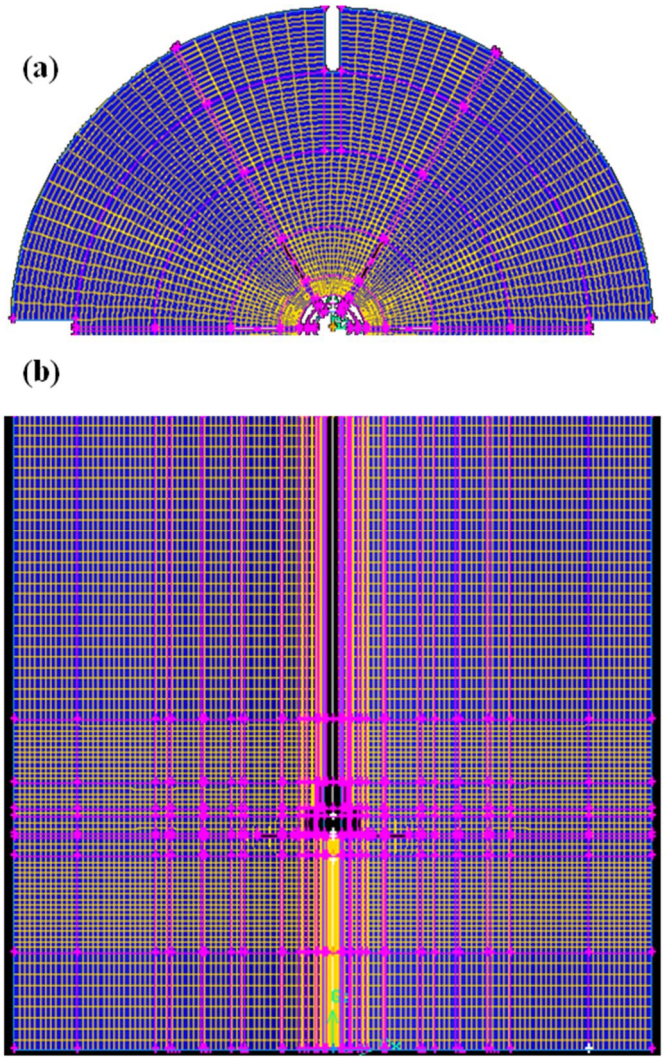

Figure 3.1 Constructed hexahedral meshes in entire domain (a) plan view, (b) sectional view.

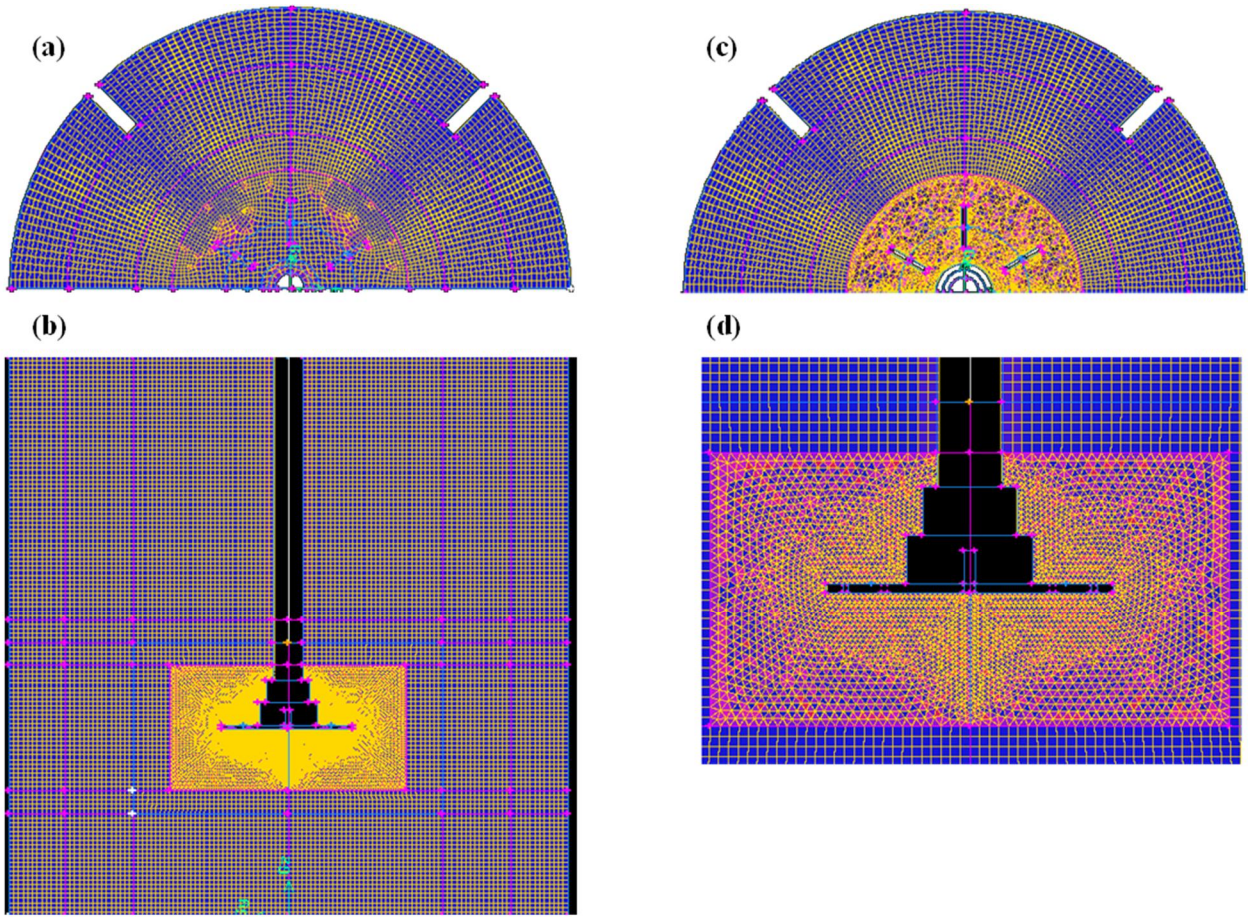

Figure 3.2 Constructed meshes in entire domain using two different types of meshes (a) plan, (b) sectional view of meshes in the domain (mostly hexahedral) and (c) plan, (d) sectional views of tetrahedral meshes in the area around impeller.

3.2 Multiple Reference Frames (MRF) Method

The rotating frame model solves the momentum equations for the entire domain in a rotating frame. Problems solved in a rotating frame typically use the angular velocity of the primary rotating component, as the angular velocity of the frame. In stirred tanks, the impeller serves this purpose, so the frame is assumed to rotate with the impeller. Thus, the impeller is at rest in the rotating frame. The boundaries of the rotating frame must be a surface of the revolution. Since baffles are not a surface of revolution and the selected configuration for this research is baffled stirred vessels, a modification of a single

rotating frame, i.e., the multiple reference frames (MRF) method was used. In order to use MRF simulation, the total system volume was divided in two volumes. The first volume enclosed the impeller region. The second volume contained the baffle and remainder of the vessel volume. The momentum equations inside the rotating frame were solved in the frame of the enclosed impeller while those outside the rotating frame were solved in the stationary frame. A steady transfer of information took place at the MRF interface as the solution progressed. If the interaction between impeller and baffles is weak, the effect of relative orientation of impeller and baffles can be neglected. However, for stronger interactions one should use the sliding mesh (SM) method, which is an unsteady state method and would be able to account for that interaction (Paul et al. 2004). In order to use the same geometry for both MRF and SM the meshes (including rotating volume and stationary volume in the MRF method) should be exactly the same.

CFD programs such as Fluent numerically solve the general equations representing the conservation of mass and momentum. In Cartesian coordinates, the continuity equation for an incompressible fluid written using the summation convention can be expressed as:

$$\frac{\partial u_i}{\partial x_i} = 0 \tag{3.1}$$

Similarly, the momentum balance equation for the same incompressible fluid (Navier-Stokes equation) can be written as:

$$\frac{\partial u_i}{\partial t} + \frac{\partial u_i u_j}{\partial x_j} = -\frac{1}{\rho}\frac{\partial P}{\partial x_i} + \nu \nabla^2 u_i + g_i \tag{3.2}$$

In this equation, the second term on the left accounts for the convective momentum transport, while the terms on the right represent, pressure forces, viscous transport, and body forces (such as gravity), respectively.

In turbulent flow, it is customary to assume that the velocity at any point can be taken to be the sum of the mean (time-averaged) and fluctuating components, i.e.:

$$u_i = \overline{u}_i + u_i' \tag{3.3}$$

Using this equation the continuity equation can be rewritten as:

$$\frac{\partial \overline{u}_i}{\partial x_i} = 0 \tag{3.4}$$

The time-averaged momentum equation, which can be used for the prediction of the velocities in turbulent flow, becomes:

$$\frac{\partial \overline{u}_i}{\partial t} + \frac{\partial \overline{u}_i \overline{u}_j}{\partial x_j} = -\frac{1}{\rho}\frac{\partial \overline{P}}{\partial x_i} + \nu \nabla^2 \overline{u}_i + g_i - \frac{\partial}{\partial x_j}\left(\overline{u_i' u_j'}\right) \tag{3.5}$$

The last term in this equation represents the Reynolds stresses containing the product of the fluctuating velocity components. Since the Reynolds stresses cannot be predicted from first principles, they are typically calculated by making some assumptions about their relationship with other variables (closure problem). *"Boussinesq Hypothesis"* makes the assumption that Reynolds stresses can be expressed in terms of mean velocity gradients (Paul et al. 2004).

$$\rho\left(\overline{u_i' u_j'}\right) = \frac{2}{3}\rho k \delta_{ij} + \left[\mu_t\left(\frac{\partial \overline{u}_i}{\partial x_j} + \frac{\partial \overline{u}_j}{\partial x_i}\right)\right] \tag{3.6}$$

$$\mu_t = \rho C_\mu \frac{k}{\varepsilon} \tag{3.7}$$

In the above equation C_μ is a constant. There are different turbulence models that offer different equations to calculate the kinetic energy of turbulence (k) and the rate of dissipation of turbulence (ε). Two turbulence models were used in this research to account for the turbulent effects during the numerical simulations, i.e., the standard k-ε model and the realizable k-ε model coupled with wall treatment. These two turbulent models are discussed below (Paul et al. 2004).

3.2.1 Standard k-ε Model

The *k-ε* model is one of the families of two-equation models for which two additional transport equations must be solved to compute the Reynolds stresses. The main advantage of this model is its robustness, meaning that it is computationally stable and easy to work with even for a fluid with more complex behavior. It is a semi-empirical model based on observation of high-Reynolds-number flow. The main disadvantage of this model is the assumption that fluctuating velocities are isotropic. There are two transport equations that need to be solved for k and ε. These governing equations for standard *k-ε* model are (Paul et al. 2004):

$$\frac{\partial}{\partial t}(\rho k)+\frac{\partial}{\partial x_i}(\rho k\overline{u}_i)=\frac{\partial}{\partial x_i}\left(\mu+\frac{\mu_t}{\sigma_k}\right)\frac{\partial k}{\partial x_i}+G_k+G_b-\rho\varepsilon \tag{3.8}$$

$$\frac{\partial}{\partial t}(\rho\varepsilon)+\frac{\partial}{\partial x_i}(\rho\varepsilon\overline{u}_i)=\frac{\partial}{\partial x_i}\left(+\frac{\mu_t}{\sigma_\varepsilon}\right)\frac{\partial\varepsilon}{\partial x_i}+C_1\frac{\varepsilon}{k}G_k=\mu C_2\rho\frac{\varepsilon^2}{k} \tag{3.9}$$

$$G_k=\mu_t\left(\frac{\partial\overline{u}_i}{\partial x_j}+\frac{\partial\overline{u}_j}{\partial x_i}\right)\frac{\partial\overline{u}_j}{\partial x_i} \tag{3.10}$$

C_1, C_2, σ_k, and σ_ε are empirical constants.

3.2.2 Realizable k-ε Model

The realizable *k-ε* model (Shih et al. 1995) is a more recent addition to the family of two equation models. It is different from the standard *k-ε* model in two ways (Paul et al. 2004):

i. C_μ is no longer constant here. This is because in highly strained flow, some of the normal Reynolds stress, $\overline{u}_i^2$ can become negative in the *k-ε* model, which becomes "*unrealizable*".

ii. Different source and sink terms in the transport equations for eddy dissipation are sued.

The modified prediction of ε, along with the modified calculation for μ_t, makes this model superior to other *k-ε* models for a number of applications. In particular, the model does better in predicting the spreading rate of round jets, such as those emitted from a rotating impeller blade.

3.3 Volume of Fluid (VOF) Method

The VOF method can model two immiscible fluids (or phases) by solving a single set of momentum equations and tracking the volume fraction of each of the fluids throughout the domain (Hirt et al., 1987). In stirred tank applications, the VOF model is useful for tracking the shape of air-liquid interface (Sera et al., 2001; Haque et al., 2006; Mahmud et al., 2009). In this research VOF model was used to model the air-water interface in stirred tanks for different liquid level. The following restrictions apply to the VOF model in Fluent:

i. One set of momentum equations is used in this model. The variables or properties in any given cells are either purely representative of one of the phases, or representative of a mixture of phases, depending on the volume fraction values.
    a. α_i=0: The cell is empty (of phase i)
    b. α_i=1: The cell is full (of phase i)
    c. 0< α_i<1: The cell contains the interface between two phases.

ii. All control volumes must be filled with either a single phase (e.g. air or water) or a combination of both phases. The VOF model does not allow any void regions in the domain.

iii. The VOF formulation relies on the fact that two or more phases are not interpenetrating. In another word this model has been designed for immiscible phases.

If the interface lies inside the control volume, special treatment is used to track its position and slope in both the control volume and neighboring cells as the calculation progresses. This procedure contains calculation of the volume fraction for secondary phase, α_i, which represents the fractional volume of the cell occupied by that phase. Since the fluid type does not change along particle paths in an incompressible, non-reacting flow, the characteristic function α_i is passively advected with the flow. The VOF model includes the solution of a scalar advection equation for the quantity of the volume fraction of the secondary phase. In this work primary phase is water and secondary phase is air. The advection equation for the volume fraction for phase A (air) in Cartesian coordinate is:

$$\frac{\partial \alpha_A}{\partial t} + \vec{u}_A \frac{\partial \alpha_A}{\partial x} + \vec{v}_A \frac{\partial \alpha_A}{\partial y} + \vec{w}_A \frac{\partial \alpha_A}{\partial z} = 0 \tag{3.11}$$

$\vec{v} = (u, v, w)$, velocity field

For an incompressible fluid, the conservation of mass or continuity equation is:

$$\frac{\partial u_A}{\partial x} + \frac{\partial v_A}{\partial y} + \frac{\partial w_A}{\partial z} = 0 \tag{3.12}$$

Multiplying Equation 3.12 by α_A and adding it to Equation 3.11, conservation law for the volume fraction will be obtained:

$$\frac{\partial \alpha_A}{\partial t} + \frac{\partial \vec{u}_A \alpha_A}{\partial x} + \frac{\partial \vec{v}_A \alpha_A}{\partial y} + \frac{\partial \vec{w}_A \alpha_A}{\partial z} = 0 \tag{3.13}$$

Then the volume fraction for the primary phase (water) can be simply calculated from:

$$\alpha_A + \alpha_W = 1 \tag{3.14}$$

As mentioned before, a single momentum equation is solved throughout the domain and the resulting field is shared among the phases. The governing momentum balance equation is:

$$\frac{\partial u_i}{\partial t} + \frac{\partial u_i u_j}{\partial x_j} = -\frac{1}{\rho}\frac{\partial P}{\partial x_i} + \nu \nabla^2 u_i + g_i + \mathrm{F} \tag{3.15}$$

In the momentum equations, material properties are determined based on presence of the component phases in each control volume. For the case of a two-phase flow, the density and viscosity are calculated by these equations:

$$\rho = \alpha_A \rho_A + (1 - \alpha_A)\rho_W \tag{3.16}$$

$$\mu = \alpha_A \mu_A + (1 - \alpha_A)\mu_W \tag{3.17}$$

F, the source term, in VOF simulation is the surface tension. The surface tension model in Fluent is the continuous surface force (CSF) model proposed by (Blackball et al. 1992).

In summary, in the VOF model there are six equations (Equation 3.12, Equation 3.13, Equation 3.14, and three equations such as Equation 3.15 in three directions)) to be solved. Depending on the method that one can choose to solve the volume fraction (α_A) equation (Equation 3.13) in Fluent 6.3, VOF models can be classified into two categories (www.fluentusers.com):

i. Interface Reconstruction methods:

   a) Geo-Reconstruct: which is an explicit time marching solution for α and it captures most accurate shape of interface. The left ring shown below (Figure 3.3) is the real interface and the right one is the simulated interface based on Geo-Reconstructed method.

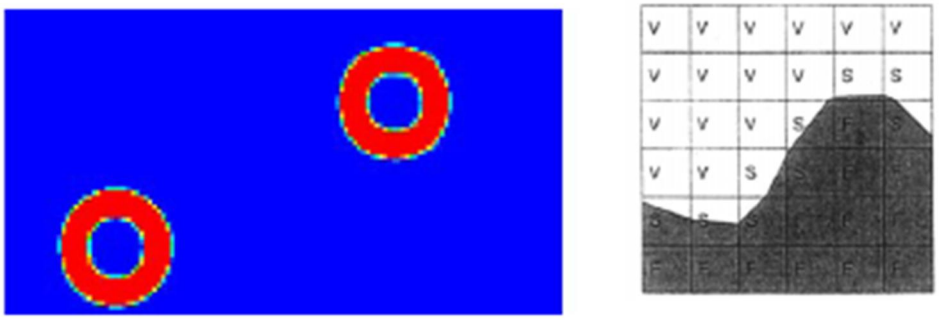

Figure 3.3 On the left side the real interface and the right side the simulated interface based on Geo-Reconstruct method.

Source for Figure 3.3: http://www.fluentusers.com/support/ugm04/auto/multiphase.pdf, accessed October, 2010.

b) Donor-Acceptor: which is an explicit time marching solution for α and it captures less accurate shape of interface. The left red ring, shown in Figure 3.4, is the real interface and the right one is the simulated interface based on Donor-Acceptor method.

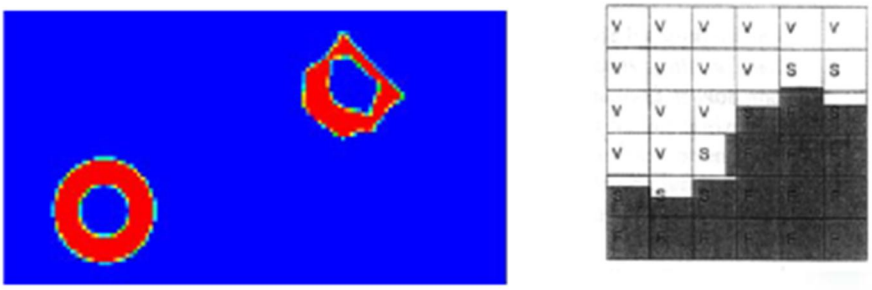

Figure 3.4 On the left side the real interface and the right side the simulated interface based on Donor-Acceptor method.

Source for Figure 3.4: http://www.fluentusers.com/support/ugm04/auto/multiphase.pdf, accessed October, 2010.

ii. Discretization methods

c) In this method, the equations are solved as any other transport equation. One such solving method is implicit time marching which allows larger time steps and has interface diffusion and needs higher order of discretization scheme to solve. Figure 3.5 shows the real interface of the rig in the left hand side and the simulated interface on the right one

In Stirred tank application, the VOF model is useful for tracking the shape of the liquid surface during operation. Even though usually the steady state shape of the surface is of interest, a transient VOF formulation is usually the best way to obtain it. With this in mind, either the steady state MRF or transient SM model can be used for this purpose. If the MRF model is used, the gradual change of the free surface can be predicted using the

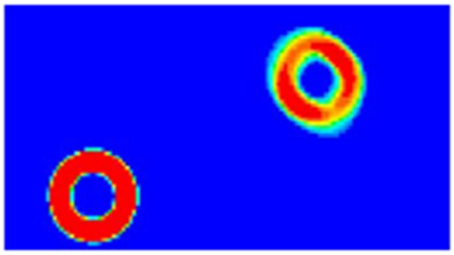

Figure 3.5 On the left side the real interface and the right side the simulated interface based on Discretization method-Implicit, are shown.

Source for Figure 3.5: http://www.fluentusers.com/support/ugm04/auto/multiphase.pdf, accessed October, 2010.

However, in VOF simulation here since the orientation of the impeller relative to the baffles is fixed, any irregularities in the free surface that result in impeller rotation will not be captured. If these details are important, the sliding mesh model should be used (Paul et al. 2004). In this work, since the interaction between the impeller and baffles were weak and the details of the interface tracking were not of interest, transient VOF simulation combined with MRF method were used. Moreover, both Regular Discritization and Reconstruct Interface methods (Geo-Reconstruct) were used to solve volume fraction equation.

In this work, the air-liquid interface was not predicted based on Regular Discritization method because of numerical diffusion. However, the Geo-Reconstruct method predicted an air-liquid interface which was very close to the experimental observations. Therefore, the results from this method (Geo-Reconstruct) are presented in the Results section (Chapter 4).

3.4 Computational Prediction of Impeller Pumping Flow and Pumping Number

The same approach described in the experimental section was used here computationally to calculate N_{Qr}. The only difference here was the use of computationally predicted velocities instead of experimental results. In order to compute the radial Pumping number, the radial discharge flow rate (Q_r) must be calculated. The following equation was used for this purpose:

$$Q_r = \int_{-w_c/2}^{w_c/2} V_{r\ out}{}_{r=d/2} \pi D_c dz \tag{3.18}$$

In these equations, D_c and w_c denote, respectively, the diameter and height of the cylinder surrounding the impeller where the velocities were predicted and used to calculate the pumping rate. Ideally, the radial discharge flow rate Pumping number should be calculated using velocities a cylinder around the impeller with a diameter and height exactly equal to the impeller diameter and blades height. However, acquiring velocity data at that position is impossible by both experimental and computational techniques. In this work the constructed cylinder had a diameter of 4.2 cm (r/R=0.34) and a height of 2 cm (h/W=1.33) around a DT 7.65 cm in diameter in a 24.6 cm tank.

There are two methods to calculate radial discharge flow rate through the side surface of constructed cylinder, computationally: (1) using the velocity data calculated via CFD and calculating Q_r based on Equations 3.18; (2) using the net flow rate data through a selected surface (side surface of the cylinder) included by commercial software such as Fluent. The former method is more accurate but it needs more calculation since it captures any possible radial income flow rate. In the latter method, it should be assumed that there is either flow out or flow in, through each surface of the cylinder around the impeller. Both methods have been used in this work and the results were extremely

similar. Radial pumping numbers (N_{Qr}) for different filling ratios and impeller off-bottom positions were predicted as a result.

3.5 Computational Prediction of Impeller Discharge Angle

The impeller discharge angle was calculated using CFD simulation data and compared to that obtained experimentally. In this work, radial and axial velocity components predicted by CFD on the side surface of a cylinder around impeller with a radius r such that r/R=0.34 and height equals to the blade height (z_1=7.5 cm and z_2 = 9.04cm) were used to calculate impeller discharge angle at each point on this surface. Then the final impeller discharge angle was reported as the average of all those data (some 2000 points).

3.6 Computational Prediction of Impeller Power Dissipation and Power Number

In this work, the torque applied to the impeller was calculated from the predicted values of the pressures applied at each point on the impeller blades, from which the tangential forces on the impeller blades could be calculated. The same equations (Equation 2.1 and Equation 2.2) mentioned in experimental section were used to calculate the power dissipated and hence power number from computational predictions. The pressure difference on each impeller blade and the shear stress on the blade width, disk, hub and shaft are the forces applied to the impeller in the tangential direction. Using the following equation, the torque, Γ, was calculated from CFD simulations:

$$\Gamma = \sum_i \left(P_1 - P_2\right)_i . r_i \delta A_i + \sum_j \tau_j . r_j \delta A_j \tag{3.19}$$

where the calculation was performed over all control cells, i corresponds to each blade and j corresponds to the thickness of the blades, disk and hubs. In this equation, r is the

force arm and δAi is the cell surface area, and P_1 and P_2 are the pressures on the front and back of the blade.

3.7 Computational Prediction of Mixing Time

Numerical simulation method used here to calculate the mixing time similarly to the way it was determined experimentally. First the flow field for the system under study was computationally determined and then a blob of a tracer was numerically introduced (a vertical cylinder with reduce of 0.4cm, a height of 1cm and center point of (X=0 cm, Y=6.15 cm, Z'=0.7 cm away from air-liquid interface)). With the flow field SO "frozen", the tracer mass fraction was solved in a transient way to calculate the time required to achieve a predefined level of homogeneity (95%). The temporal and spatial distributions of the tracer concentration were obtained from the solution of the Reynolds-averaged species transport equation (Javed et al. 2006).

$$\frac{\partial c}{\partial t}+\frac{\partial}{\partial x_i}\left(u_i c\right)=-\frac{\partial}{\partial x_i}\left(-D_m\frac{\partial c}{\partial x_i}\right)-\frac{\partial}{\partial x_i}\left(u_i^{'}c^{'}\right) \tag{3.20}$$

Where c and $c^{'}$ are the mean component and fluctuating component of tracer mass concentration, respectively, and D_m is molecular diffusion coefficient. The turbulent mass fluxes component, $u_i^{'}c^{'}$, are modeled using gradient-diffusion approach (Javed et al. 2006):

$$\overline{u_i^{'}c^{'}}=-E_D\frac{\partial c}{\partial x_i} \tag{3.21}$$

Where E_D (=μ_t / σ_t) is the eddy diffusivity, μ_t (=$C_\mu \rho k^2/\varepsilon$) the turbulent viscosity, σ_t stands for the turbulent Schmidt number and is taken as 0.7, and C_μ is a constant number.

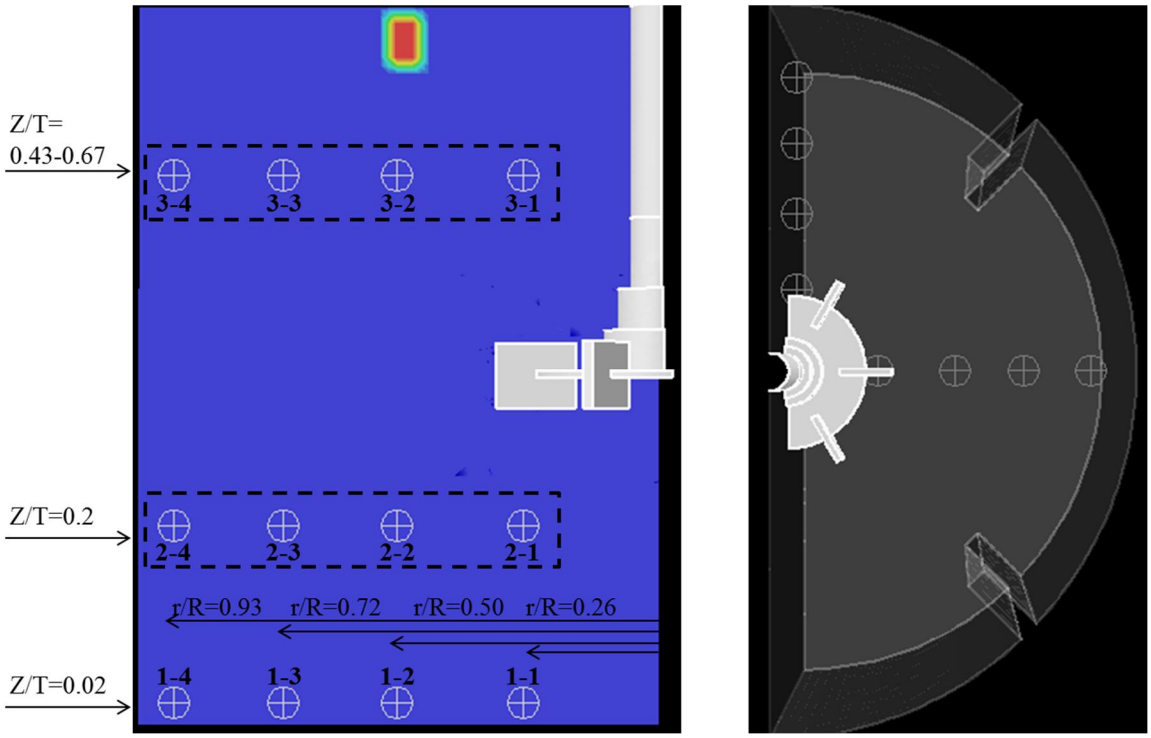

Figure 3.6 Geometric locations in which the normalized concentrations of tracer as a function of time were recorded. The dashed lines indicate the areas considered by Javed et al. (2006). The square area at the top of the vessel is the location of tracer injection.

Mixing time was determined by analyzing the tracer mass fraction in different points in the vessel, when 95% uniformity was achieved. Two vertical planes at 0° and 90° have been used to calculate mixing time. The calculation locations within each plane and also tracer injection area are shown in Figure 3.6. Data at Z/T=0.02 were used to study the mixing phenomena close to the tank bottom.

The next two axial data sets were between the impeller and tank bottom and between impeller and air-liquid interface which have been selected to study the mixing time in the whole vessel as impeller submergence is decreasing. t_{95} is the average of all data calculated to achieve 95% uniformity. The highest Z/T data location is different for different impeller submergence ratios and it is in the middle of impeller and air-liquid interface: Z/T= 0.43 for S_b/D= 0.56 and Z/T=0.67 for S_b/D=2.23. Data points for Z/T=0.2 and Z/T=0.67 have used by other researchers (Javed et al., 2006 and Distelhoff et al., 1997) for mixing time calculation in stirred vessel with standard configuration (C/T~1/3, H/T=1 and S_b/D~2.23) and their results have been used here as another benchmark for the CFD simulation.

CHAPTER 4

RESULTS AND DISCUSSION I - FLOW REGIMES IN CONVENTIONAL STIRRED VESSELS FOR DIFFERENT FILL RATIOS

4.1 Result for Standard Case (H/T=1)

The most common configuration for stirred vessels is that with H/T=1, D/T=1/3, and C=T/3 (S_b/D=2.23). This system has been extensively studied by previous investigators. Therefore, this configuration was used in this component of the work to validate the appropriateness of the experimental technique and the computational approach used here.

The velocity profiles in stirred Tank #2 with Impeller #2 (dimensions specified in Chapter 2) with the standard configuration (H/T=1, C=T/3) were obtained here using both computational and experimental techniques. The impeller speed was 300 rpm corresponding to an impeller tip speed of 1.2 m/s and an impeller Reynolds Number of 29,250. Since this value falls within the turbulent regime, a turbulence model was incorporated in the simulation to account for turbulence effects.

Steady state results were obtained using a multiple references of frames (MRF) approach and assuming the flat air-liquid interface (FS). Results were obtained using both the standard k-ε model and the realizable k-ε models for turbulence. The former method is denoted in the graphs and tables as "FS-SKE CFD Simulations" and the latter method as "FS-RKE CFD Simulations". For each model, first-order discretization and second-order discretization were used. However, only the results with second-order discretization are presented in this paper because of their better agreement with the experimental results. Three different mesh densities and qualities were tested here in order to assess the quality of the meshes and also to determine the smallest mesh size that produced mesh-independent results (Deglon and Meyer, 2006; Coroneo et al., 2011).

Since the MRF simulation is a steady state simulation of an intrinsically unsteady-state system, the average velocity field along a circumference at any radial location was taken as the average velocity at that location and compared with the experimental data.

The experimental results presented here are averages of 500 PIV measurements by PIV1 (TSI PIV). This eliminated any periodic effects caused by the impeller position. The time between two laser pulses was 400 μs and the interrogation area was set to 64×64 pixels. The cross correlation method of image pares was performed on a rectangular grid with 50% overlap between adjacent grids.

Figure 4.1 presents the CFD and PIV data obtained in this work. Dimensionless mean axial and radial velocities at three different axial levels, one rake below the impeller and one above the impeller and one in the impeller region, are presented. These figures show that, in general:

i. there is good agreement between the experimental data and the predicted results for the velocity distribution found in this work;
ii. the velocity profiles predicted using both turbulence models (SKE and RKE) are close to each other but that results using RKE are in better agreement with the experimental measurements.

Another approach to validate the simulations is by calculating global parameters such as the impeller Pumping Number, N_Q, and the Power Number, Po. . These non-dimensional numbers are constant for specific type of impellers in the standard configuration and under turbulent conditions. In this portion of the work, the Power Number and Pumping Number for the stirred tank with standard configuration (C=T/3 and H/T=1) were obtained experimentally and computationally (using both SKE and

RKE models) and compared with the results available in the literature. The system under investigation here produced a “double loop” recirculation flow (DL Regime), one above and the other below the impeller. For this kind of flow pattern Q_{out} around impeller is expected to be

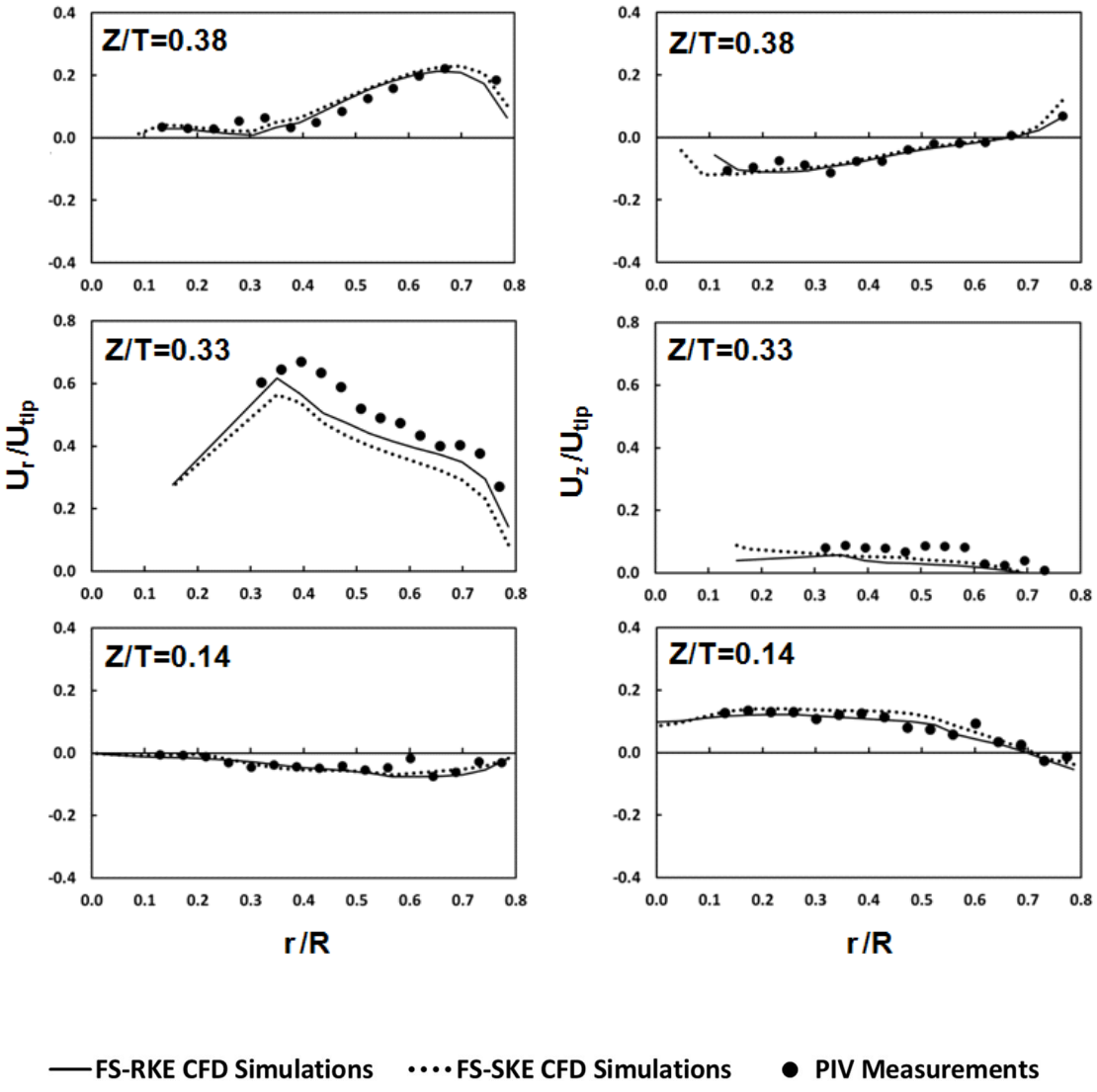

Figure 4.1 Comparison between PIV and CFD predictions of axial and radial velocities using both standard k-ε and realizable k-ε on three different iso-surfaces for C_b/T=0.30, D/T=0.31 and N=300 rpm.

almost identical to radial flow out, Q_r. Therefore, the impeller Pumping Number, N_Q and the impeller radial Pumping Number, N_{Qr} are expected to be the same.

A summary of the results are presented in Tables 1 and 2. These results show that there is good agreement between the experimental data and the computational results obtained here for N_Q and Po. The RKE-based results for Po are in slightly closer agreement with the experimental measurements. The Pumping Number predicted by both turbulence models are the nearly same. Also, the results obtained in this work are in agreement with those available from the literature.

Based on the computational results achieved so far, the realizable k-ε turbulence (RKE) model for H/T=1 appeared to be slightly better than the SKE model. Therefore, the RKE model was used as the turbulent model for the remaining simulations in this work.

After validating the CFD simulation for H=T, the flow pattern and velocity field in the same stirred vessel at different impeller submergence ratios (S_b/D), i. e. different fill ratios (H/T), were studied.

4.2 Effect of Impeller Submergence Ratio on Flow Pattern in a Conventional Stirred Vessel with H/T<1

A flat air-liquid interface was assumed for all the simulations in this portion of the work. Therefore, the results from this section are denoted in the figures as FS (Flat Surface). PIV2 (Dantec PIV) was used here to measure the velocity field. The 2D Velocity vectors obtained through PIV measurements at 300 rpm and the corresponding values predicted by FS-CFD simulations and are shown in Figure 4.2. These results were obtained are for different impeller submergence ratios S_b/D, i.e., 2.23 (H/T=1), 1.24 (H/T=0.69), 0.98

(H/T=0.61), 0.77 (H/T=0.54), and 0.59 (H/T=0.49). The flow pattern predicted by CFD simulations are presented for a larger cross sectional area than to PIV measurements for better visualization purpose. The rectangular area shown in each of the CFD simulation panels shows the areas of the tank that had been investigated by PIV. 2D velocity contour plots were also obtained using the same PIV data and compared to the CFD simulations, as shown in Figure 4.3. The velocity contours plots cover the same cross sectional area of the tank, both computationally and experimentally.

Table 4.1 Pumping Number for D/T=0.31 and C_b/T=0.30

Method	**N_{Qin}**	**N_{Qout} or N_{Qr}**	**Difference (%)[d]**
PIV Measurements		0.808	
FS-SKE CFD Simulation	0.790	0.790	-2.23 %
FS-RKE CFD Simulation	0.790	0.790	-2.23 %
Literature Data[b,c]	0.70-0.85		

[a] Difference between PIV measurements and CFD predictions (this work)
[b] Experiments: Wu and Patterson (1989); Dyster et al. (1993);
[c] Simulations: Lane and Koh (1997)

Table 4.2 Power Number for D/T=0.31 and C_b/T=0.30

Method	**Po**	**Difference (%)[d]**
Torque Measurements	4.89	
FS-SKE CFD Simulation	4.66	-4.70 %
FS-RKE CFD Simulation	4.74	-3.07 %
Literature Data[e]	4.4-5.5	

[d] Difference between present experimental torque-based power measurements and CFD predictions
[e] Dyster et al. (1993), Murthy and Joshi (2008), Yang and Takahasi (2010), Lane and Koh (1997)

A comparison of the results presented in Figure 4.2 and Figure 4.3 shows that the CFD predictions and PIV measurements of the velocity profiles and velocity contours are substantial agreement for all different S_b/D values (a detailed point-by-point comparison is provided in section 4.2.2). Additionally, it can be observed that the flow patterns for S_b/D=0.59 (H/T= 0.49) is different from the other cases in both the simulations and the experimental results. It appears that when the submergence level (S_b/D) reaches a value between 0.59 and 0.77 the upper recirculation above the impeller is suppressed and the flow regime transitions from a "double loop" recirculation flow (DL Regime), where the fluid flow forms two recirculation loops one above and the other below the impeller, to a "single loop-up-pumping" recirculation flow from top to the bottom (SL-up Regime), as evident from Figure 4.2. The submergence level above the flow transition has been defined as a critical level. For the stirred vessel studied in this chapter the critical submergence level was S_b/D=0.77 (H/T=0.54).

4.2.1 Impeller Discharge Angles, Pumping Numbers and Power Numbers in a Conventional Stirred Vessel for Different Impeller Submergence Ratios

The flow regime transition (DL to SL-up Regime) shown in Figure 4.2 and Figure 4.3 is also associated with other changes in the impeller discharge angle, Pumping Number and Power Number, as shown in Figure 4.4. For relatively large impeller submergences (S_b/D > 0.98 (H/T > 0.61)) the average impeller discharge angle was slightly pointing upwards (4-7^O). However, when the submergence was closer to the critical value (S_b/D=0.77 (H/T=0.54)) this angle started to increase and it suddenly and significantly increased to 60.10° when the flow pattern changed (S_b/D (H/T) =0.59 (0.49)). This rapid

transition was predicted computationally and experimentally (Figure 4.4a). This figure

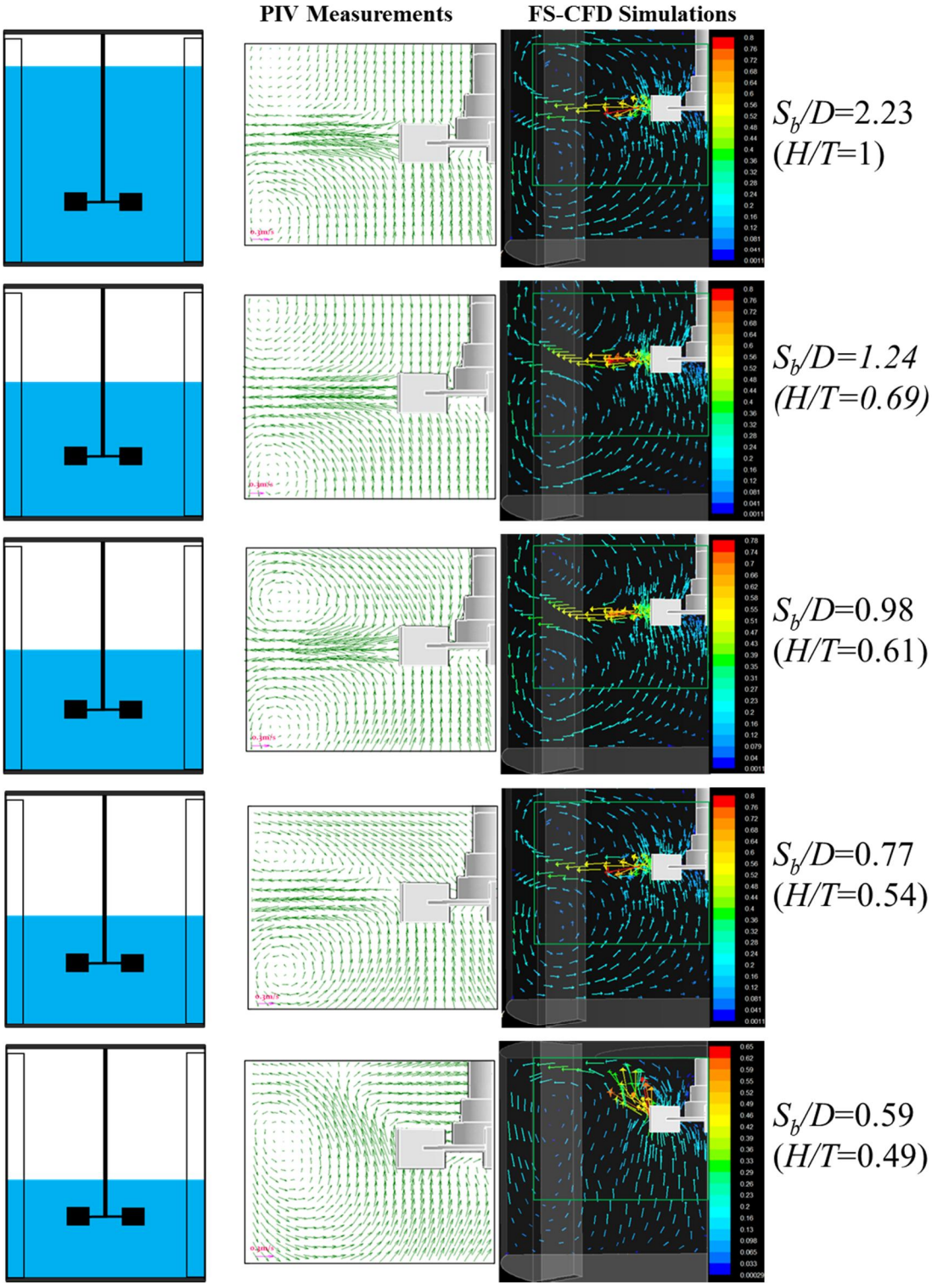

Figure 4.2 PIV measurement and FS-CFD prediction of 2D velocity vectors for different S_b/D ratios, C_b/T=0.30, D/T=0.31 and N=300 rpm.

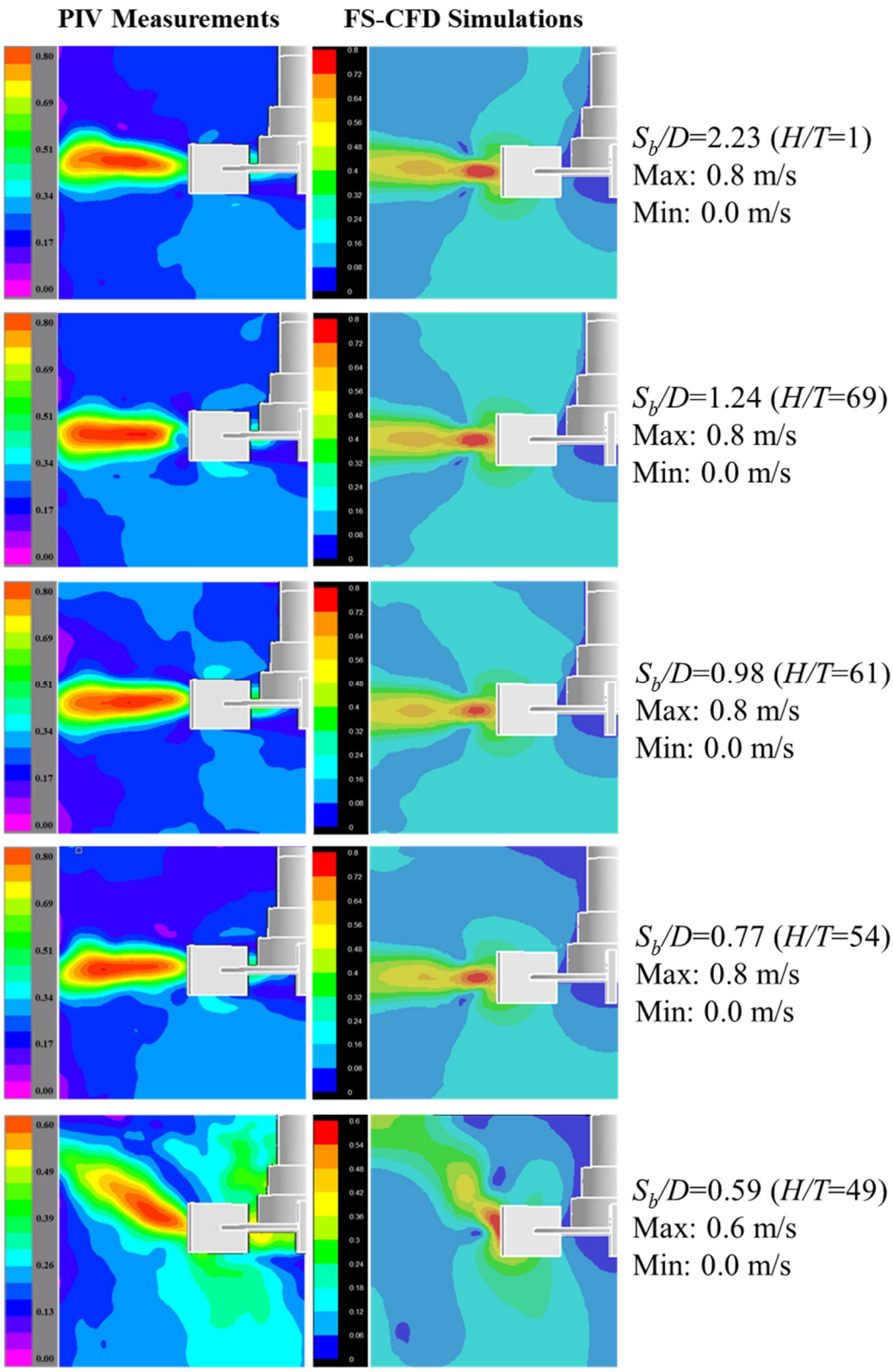

Figure 4.3 PIV measurement and FS-CFD prediction of 2D velocity contours for different S_b/D ratios, C_b/T=0.30, D/T=0.31 and N=300 rpm.

additionally shows that a substantial agreement between predictions and results exists at all submergence levels: the simulations under predicted the discharge angles by 6-12%, i.e., by less than one degree for first two cases and by 5 degrees for $S_b/D=0.59$ ($H/T=0.49$).

Figure 4.4b and Figure 4.4c show the computational predictions and experimental measurements of the Power Number and the radial Pumping Numbers, respectively, at different fill ratios. When the impeller submergence ratio S_b/D was higher than 0.59, N_{Qr} Po were nearly unaffected by submergence. However, when the impeller submergence ratio decreased to the critical level ($S_b/D=0.77$) and reached the $S_b/D=0.59$, i.e., when the flow pattern changed, these two dimensionless numbers decreased drastically.

The FS-CFD predictions for Po and N_{Qr} are in very good agreement with the experimental data for the liquid levels equal to, and higher than, the critical submergence level ($S_b/D \geq 0.77$ ($H/T \geq 0.54$)), i.e., before flow pattern transition. When $S_b/D=0.59$ the agreement is still substantial although the FS-CFD simulations slightly over predict Po and N_{Qr}.

4.2.2 Velocity Distribution in a Conventional Stirred Vessel for Different Impeller Submergence Ratios

A quantitative comparison of the FS-CFD simulation results for the radial and axial velocities for the impeller submergence ratios (S_b/D) equal to 2.23 ($H/T=1$), 1.24 (0.69), 0.77 (0.54), and 0.59 (0.49) at five different axial (vertical) locations in the liquid are presented in Figure 4.5. These figures show that the axial velocity profiles and the radial

velocities profiles were not strongly affected by the submergence ratio when this ratio was sufficiently high, i.e., when S_b/D was equal to 2.23, 1.24 and 0.77 (this was less so when the measurement were taken closer to the free surface, as when Z/T=0.45). However, when the flow pattern switched to the SL-up Regime (S_b/D =0.59; (Figure 4.2 and Figure 4.3) the velocities changed significantly, and were lower both radial and axial components. Figure 4.5 also shows the experimental velocity measurements for S_b/D=0.59, which as in substantial although not perfect, agreement, with the predictions, thus again validating the change in flow pattern and the weakening of the overall circulation flow. The decrease in the radial and axial velocities that accompany the flow transition is likely to impact the mixing efficiency in such systems, and especially solid suspension which require higher velocities field close to tank bottom to avoid particle settling. This phenomenon will be discussed in greater detail in Chapter 6.

Another less pronounced change in the flow field can be seen in these graphs for impeller submergence ratios from 1.24 to 0.77. The radial velocity in upper portion of the liquid (Z/T= 0.45) for S_b/D=0.77 is mostly negative, implying that the flow in that region is toward the impeller. However, for $S_b/D \geq 1.24$ this velocity is very small but positive. This observation further confirms the flow patterns for the same impeller submergence ratios presented in Figure 4.2.

4.3 Effect of Agitation Speed on Flow Pattern, Surface Air Entrainment and Impeller Flooding

N_E can be defined as the minimum agitation speed that results in the surface entrainment of air bubbles into the vessel. As the impeller submergence is decreased, air entrainment typically occurs at a lower agitation speed (Bhattacharya et al., 2007 and Malli et al.,

2009). For instance, N_E for agitation system used in this work with S_b/D =2.23, 0.77 and 0.59 were 600, 450 and 300 rpm, respectively.

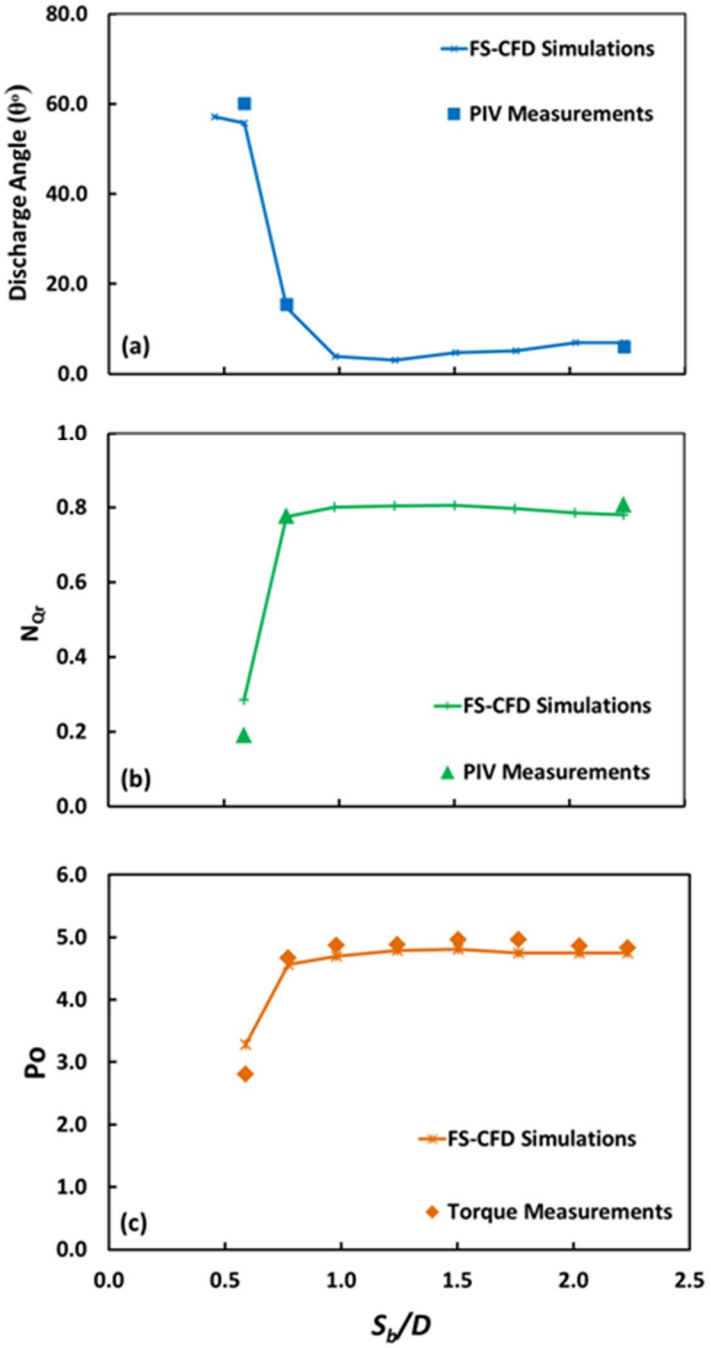

Figure 4.4 (a) Impeller discharge angle, (b) radial Pumping Number, N_{Qr} and (c) Power Number, Po for different S_b/D ratios, C_b/T=0.30, D/T=0.31 and N=300 rpm calculated from both experimental and FS-CFD Simulation data.

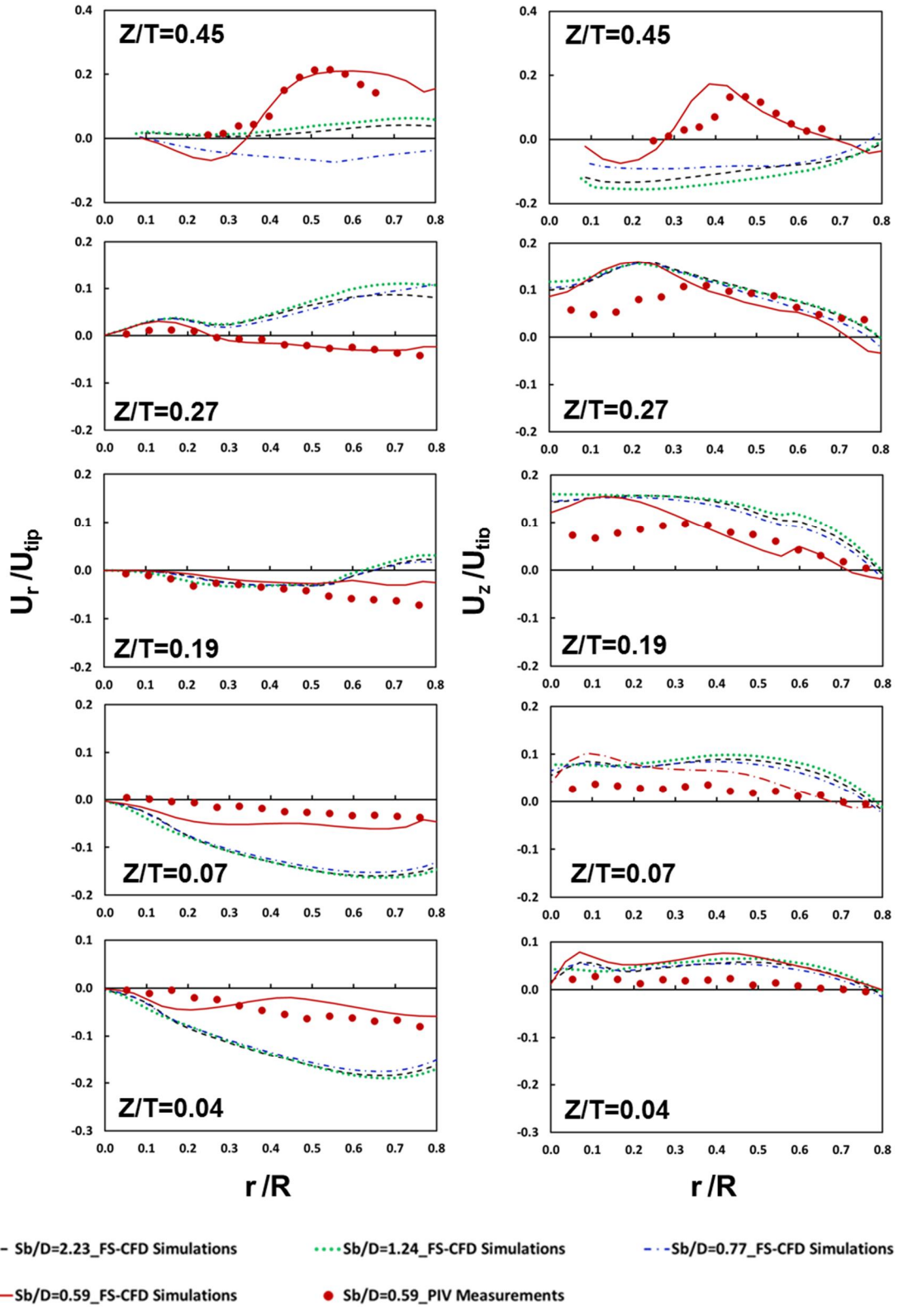

Figure 4.5 FS-CFD simulations of radial and axial velocities for different S_b/D ratios on five different iso-surfaces (C_b/T=0.30, D/T=0.31 and N=300 rpm).

The flow patterns shown in Figure 4.2 for different impeller submergence ratios (S_b/D) were obtained at a constant agitation speed equal to 300 rpm. These results seem to indicated that flow transition occurred as a result of the change in the system geometry only, as the liquid level decreased, but they still leave open the question of the effect of agitation speed on flow pattern, flow pattern transition, and other important phenomena such as surface air entrainment, which is typically observed for low submergence ratios. In another words, it is still unclear at this point if the flow regime transition can only be attributed to geometric variables (such as S_b/D) or if dynamic effects (such as agitation speed) are also important.

To address this question, the flow patterns at low submergence were determined for different agitation speeds using PIV. The results were obtained for $S_b/D=0.77$ and $S_b/D=0.59$ for 5 different agitation speeds, i.e., 50 rpm, 200 rpm, 300 rpm 400 rpm and 500 rpm, corresponding to Reynolds and Froude Numbers equal to Re=5000 (Fr=0.005), 20,000 (0.087), 30,000 (0.195), 39,000 (0.347) and 49,000 (0.542), and are presented in Figure 4.6 and Figure 4.7, respectively. The right-hand panels in these figures additionally show the actual CCD images for each case, in order to evidence possible air entrainment effects.

Figure 4.6 shows that the “double loop” recirculation flow (DL Regime) at $S_b/D=0.77$ was not affected by increasing the agitation speed. Some small air entrainment effects could be observed at N=500 rpm (bubbles can also be seen in CCD image), but the air bubbles had no effect on the flow pattern for this impeller submergence ratio. A closer look to the flow patterns obtained for this case shows that some difference can be observed is in the upper zone around shaft at different agitation speeds. At high agitation

speeds, the upper recirculation pattern was able to produce a flow that penetrated the upper area more deeply, reaching the impeller shaft. However, at lower agitation speeds, the upper recirculation was weaker and the loop "closed" closer to the impeller blades than to the shaft. However, the double-loop flow pattern was always present for this impeller submergence, irrespective of agitation speed, even at agitation speeds as high as 600 rpm (results not shown for this case).

A different pattern emerges in Figure 4.7 which shows the PIV flow patterns and CCD images at the same agitation speeds used as the previous figure but for a lower submergence ($S_b/D=0.59$). The first observation from this figure is that the dominating flow pattern at this submergence level is the SL-up Regime, as previously observed, and this flow pattern is present at all agitation speeds, including very low agitation speeds. This flow pattern results in the formation of a segregated region above the impeller at any agitation speed. When the agitation speed is low, the radially outward jet emanating from the impeller is not able to "pull" fluid from this region and no air entrainment occurs. However, when the agitation speed is increased, the centrifugal force associated with this jet is able to pull radially more liquid from the upper central region resulting in a vortex which, depending on the agitation speed, can be more or less strong and possibly result in surface air entrainment. More specifically, the experimental results presented in Figure 4.7 along with visual observation show that for a relatively high agitation speed (starting at 200 rpm) the air-water interface started to become deformed and a vortex began to appear. By further increasing the agitation speed, the vortex depth increased. At an agitation speed equal to 300 rpm the vortex reached the impeller disk and this greatly facilitated surface air entrainment. However, this type of air entrainment was very

different from the limited air entrainment of single bubble observed at higher submergence levels when the DL Regime dominated. For example, for $S_b/D=0.77$, the few and small bubbles that were entrained were distributed into the whole mixing vessel (Figure 4.6 and N=500 rpm), which it is a common observation even for higher submergence ratios. However, when the submergence was at or below the level that produced a change in flow pattern to SL-up ($S_b/D=0.59$), massive air entrainment occurred and the bubbles remained mostly closer to the air-liquid interface (Figure 4.7 and N=300 rpm, N=400 rpm and N=500 rpm), with no bubbles observed in the lower portion of the vessel below the impeller. The PIV 2D velocity vectors in the shaded areas in Figure 4.7 should be disregarded because the air-liquid interface is no longer flat (for $N \geq 200$ rpm), and because of the presence of many large air bubbles (especially for $N \geq 300$ rpm).

Surface air entrainment at low S_b/D could result in "flooding" the impeller. Impeller flooding is a term that is commonly used in gas-liquid systems (where a gas is sparged below the impeller) when excessive bypassing of gas bubbles occurs in the system and the agitation speed is not enough to disperse them through the vessel. As a consequence, the bubbles swarm will go through the impeller region and remain closer to the shaft (Figure 4.8a). A consequence of impeller flooding is that: (1) gas-liquid system power consumption reduced drastically; (2) a stirred vessel under flooding condition loses its capability of providing adequate gas hold-up and liquid pumping, and thus gives poor process result (Paul et al., 2004).

In the system studied here, impeller flooding can occur at low enough S_b/D ratios associated with the SL-up Regime. However, in this case bubbles may entrain as a result

of surface air entrainment and then stayed mostly in the upper portion of the vessel (Figure 4.8b). Impeller flooding for this system can occur only if these two conditions are satisfied: (1) S_b/D is low enough to produce SL-up Regime; and (2) Froude Number (agitation speed) is high enough to create vortex reaching the impeller.

In order to describe the surface air entrainment process in greater detail, the Power Number was experimentally obtained at different agitation speeds (100 rpm, 200 rpm, 300 rpm, 400 rpm and 500 rpm corresponding to Fr equal to 0.022, 0.087, 0.0195, 0.347 and 0.542, respectively) for different submergence ratios (S_b/D equal to 0.46, 0.59, 0.77 and 0.98). The results presented in Figure 4.9 show that for impeller submergence ratios higher than the critical level (S_b/D=0.77 and 0.98), Po remains constant at increasing agitation speeds. However, for lower impeller submergence ratios (S_b/D=0.59 and 0.46) that are associated with a “single loop-uppumping” recirculation flow (SL-up), a power reduction can be observed. Two operating regions corresponding to different levels of power reduction can be observed. For relatively low agitation speeds (N=100 rpm and 200 rpm), the Power Number decreases from about 5 at high S_b/D to about 4 a low S_b/D ratios. This drop can be attributed exclusively to the transition in flow regime (from DL to SL-up). For example for N=200 rpm, Po decreases from 4.7 to 3.9 by decreasing impeller submergence ratio from 0.77 to 0.59. However, for higher agitations speeds the drop in Po is significantly more pronounced when S_b/D is decreased. For example for N=300 rpm, Po decreases from 4.7 to 2.8 when decreasing the impeller submergence ratio from 0.77 to 0.59 and from 4.7 to 2 when decreasing the impeller submergence ratio to 0.46. Even bigger drops in Po can be observed as the agitation speed is further increased. This larger reduction in Po at low submergence ratios is

associated with significant air entrainment. This drastic reduction in Po at low S_b/D ratios is similar to that observed in submerged gas-sparged systems when the impeller flooding is approached.

In summary, the transition from the DL Regime to the SL-up Regime resulting from lowering the submergence level is a necessary but not sufficient requirement for surface air entrainment. Air entrainment will result only if the agitation speed, and hence the Froude Number, are high enough to generate a sufficiently deep vortex that draws air into the liquid. If the agitation speed is further increased and the vortex reaches the impeller, impeller flooding will occur. In all cases in which flow transition to SL-up Regime occurs Po will drop. However, this drop will be much more significant if aeration is additionally present. Additional details on the effect of S_b/D ratio and impeller flooding on mixing performance (mixing time and minimum agitation speed to complete off-bottom solids, N_{js}) will be discussed in Chapter 6.

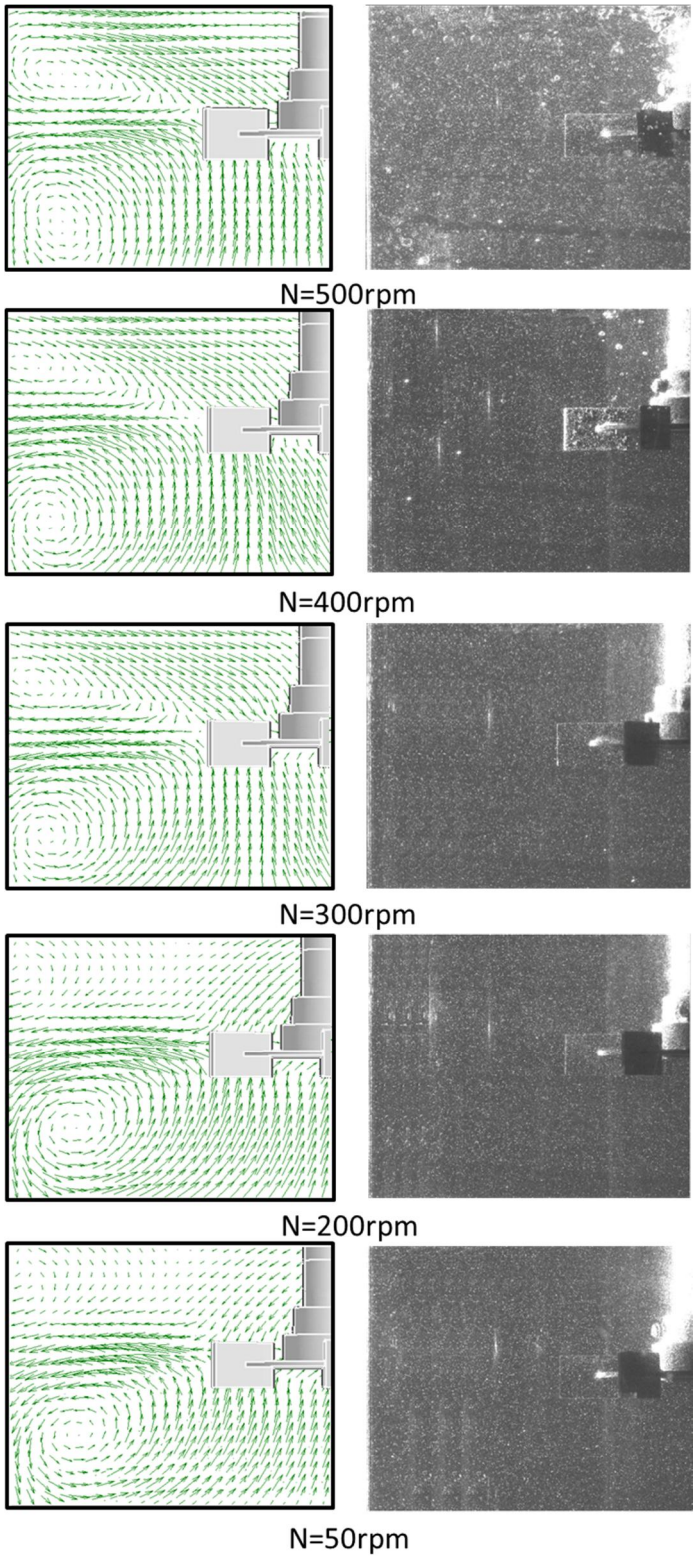

Figure 4.6 2D velocity profile measured by PIV (left-hand panels) and CCD images of the PIV investigation area (right-hand panels) for different agitations speeds when $S_b/D=0.77$, $C_b/T=0.30$ and $D/T=0.31$.

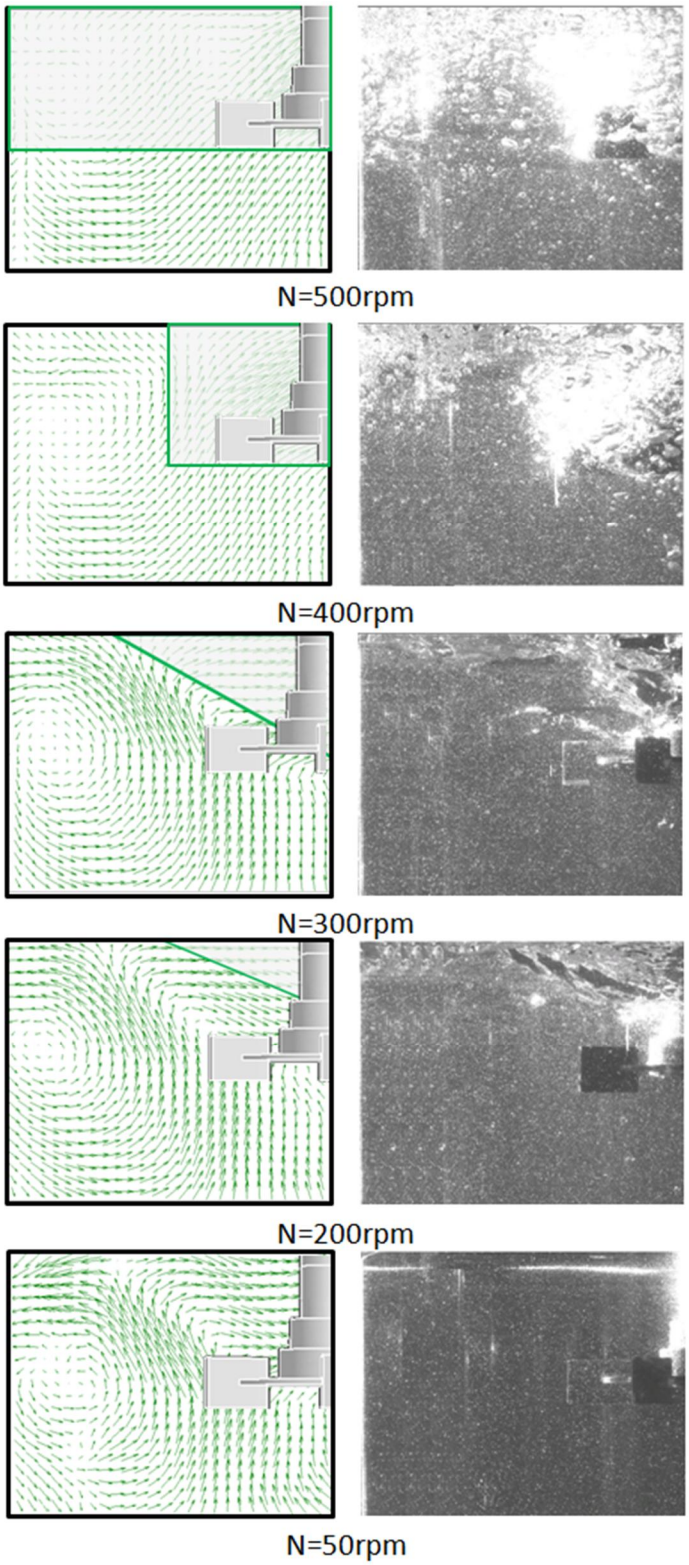

Figure 4.7 2D velocity profile measured by PIV (left-hand panels) and CCD images of the PIV investigation area (right-hand panels) for different agitations speeds when $S_b/D=0.59$, $C_b/T=0.30$ and $D/T=0.31$. PIV data in the shaded area not considered due to vortex formation and surface air entrainment.

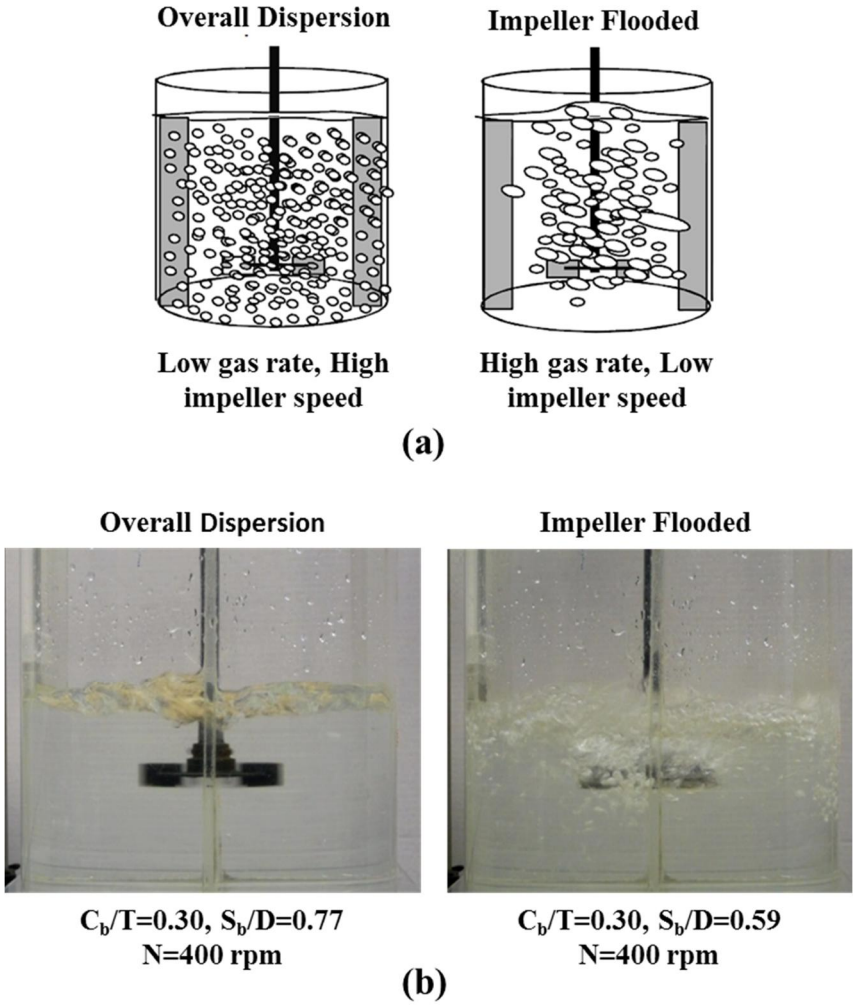

Figure 4.8 (a) Impeller flooding for submerged gas sparged system; (b) Impeller flooding for low S_b/D liquid level.

Source for Figure 4.8a: Paul et al. 2004, page 600.

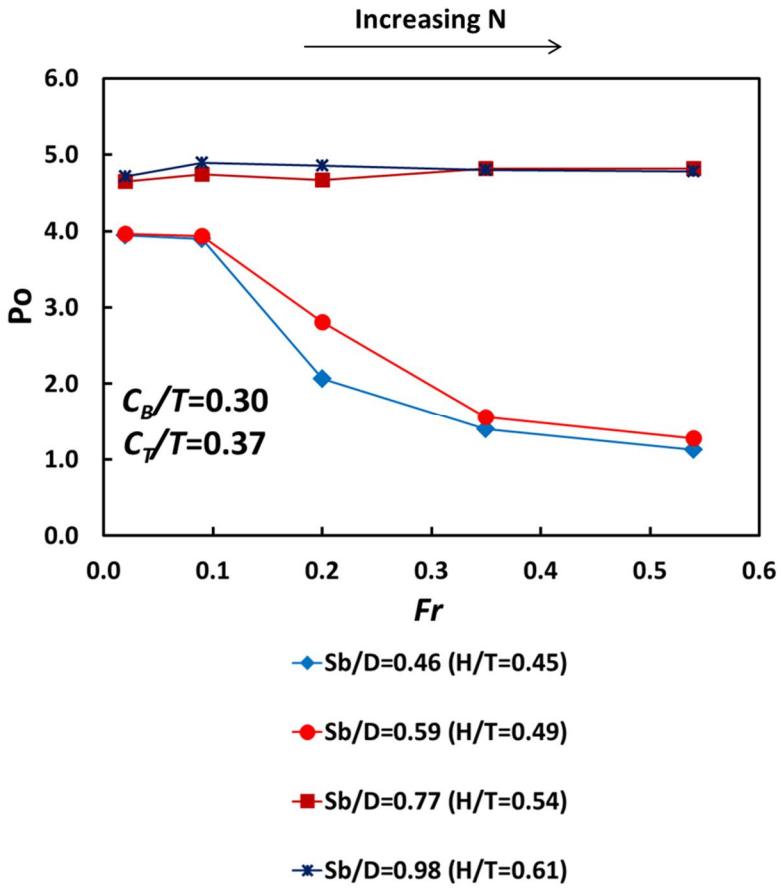

Figure 4.9 Power Number as a function of Froude Number for different S_b/D ratios, C_b/T=0.30 and D/T=0.31.

4.3.1 Volume of Fluid (VOF) Simulation for Critical Impeller Submergence Ratios

CFD simulations of the baffled stirred tanks require the specification of the boundary conditions at all surfaces, including the air-liquid interface. Typically, this interface is flat, at least for baffled tanks for which H/T=1 and possibly even when H/T<1. However, when the impeller submergence ratio decreases to below the critical value (0.59 for the geometrical variables used in this section) then the air-liquid interface might no longer remain flat since a vortex may form which modifies the surface and can result in surface air entrainment. In order to attempt to capture this phenomenon, in this part of the work,

a different computational approach was used to examine the impact of free surface simulation on the hydrodynamics. The multiphase Volume of Fluid (VOF) simulation method was used for this purpose.

A quantitative comparison of FS-CFD and VOF-CFD predictions and PIV measurements at $S_b/D=0.59$ are presented in Figure 4.10 (remark: the FS-CFD and PIV data presented here are the same as those shown in Figure 4.5). In general, the VOF-CFD predictions are in better agreement with experimental data especially in the lower portion of the tank (z/T=0.04, 0.19 and 0.27). Impeller discharge angles, Pumping Numbers and Power Numbers were also calculated using VOF-CFD simulations for the same impeller submergence ratios at 300 rpm. Figure 4.11 shows a comparison with the experimental data and the FS-CFD and VOF- CFD simulations. The VOF-CFD and FS-CFD predictions were very similar for $S_b/D=0.77$. However, the VOF-CFD predictions were in better agreement with the experimental data compared to FS-CFD simulations for $S_b/D=0.59$. As expected, the VOF method can predict the flow transition more accurately.

In the literature, the VOF simulation method has been mostly used for interface tracking. In addition, by generating appropriate meshes at the interface between two phases, the VOF model can predict air entrainment. Air entrainment simulation is computationally very intensive since in order to capture air bubbles in the liquid phase the mesh size for that zone should be 10-20 times smaller than real bubble size and as a result time step needs to be very small. Therefore, VOF simulations require much longer time for convergence in order to capture the real phenomena. In this work, a mesh size of

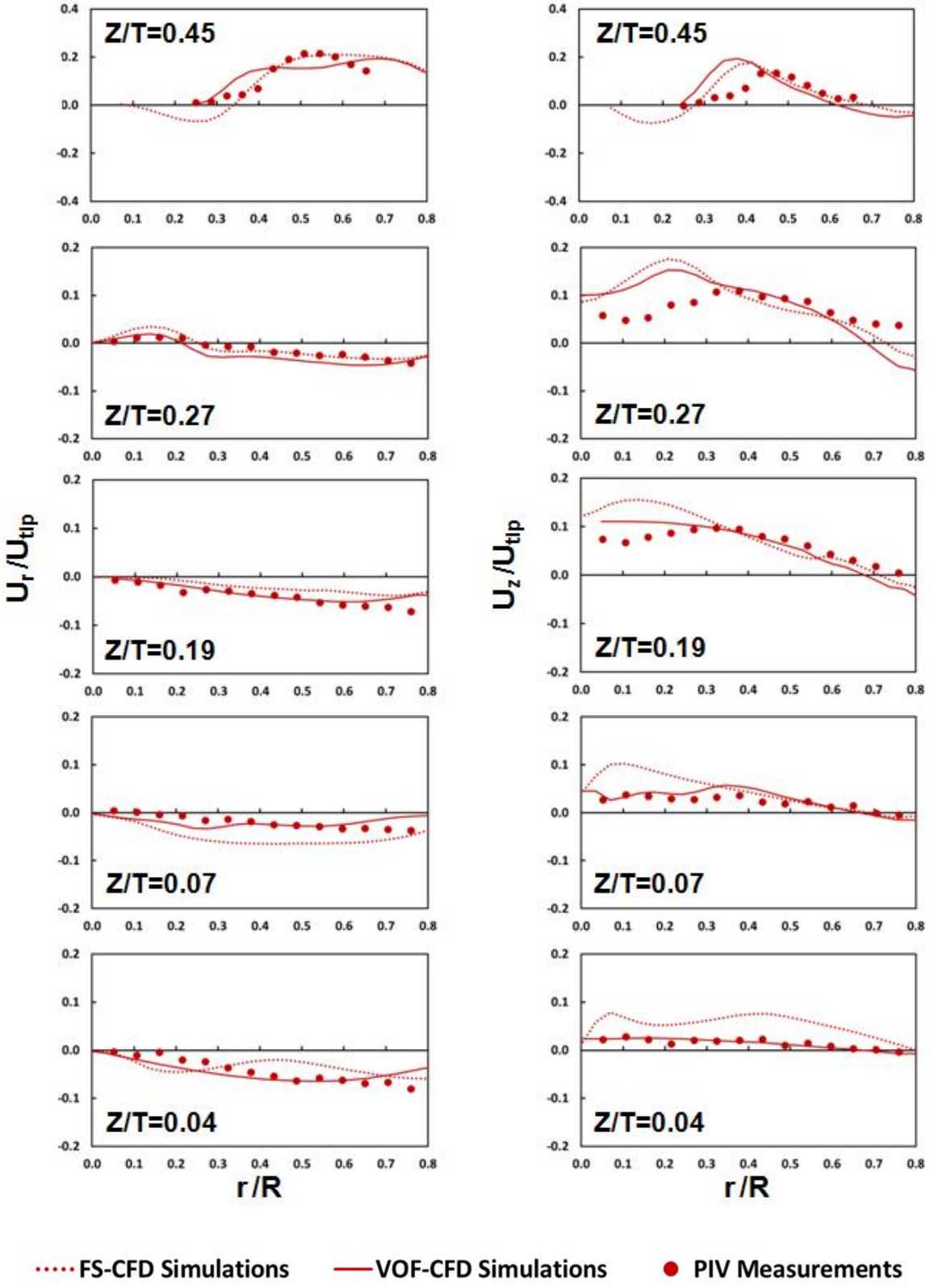

Figure 4.10 Comparison between axial and radial velocities predicted by FS-CFD simulation method and VOF-CFD simulation method and PIV data for $S_b/D=0.59$, $C_b/T=0.30$ and $D/T=0.31$ on five different iso-surfaces.

0.1 cm was used around the air-liquid interface (to ensure that that mesh quality was within a range that is acceptable for VOF simulations) which clearly is not 10-20 times smaller than bubble size. However, simulating the hydrodynamics in stirred tank with H/T=0.49 and N=300 rpm and using the above-mentioned mesh size led to the time step size on order of 10^{-5} and needed at least 400,000 iterations to converge (mesh size=650,000 cells). The VOF simulation for this case was the most computationally intensive, since it involved drastically changing of the air-liquid interface. For lower agitation speeds (N=200 rpm) this simulation was less intensive since air entrainment was not an issue although the air-liquid interface did not remain flat.

Transient VOF simulations also incorporating the MRF approach (VOF-CFD Simulations) were conducted for two different impeller submergence ratios, i.e., S_b/D=0.77 (H/T=0.54) and 0.59 (H/T= 0.49) at 200 rpm and 300 rpm (based on experimental observations, modifications to the air-liquid interface for higher impeller submergence ratio (S_b/D>0.77) were negligible. Therefore, the VOF simulations for those cases were expected to be similar to those presented in the previous section). The air-liquid phase contours predicted by the VOF-CFD simulations are shown in Figure 4.12. This figure shows that the simulation predicted a near flat air-surface interface for Sb/D=0.59 at 200 rpm. At N=300 rpm, Figure 4.12 shows that the interface between air and water was no longer predicted to be flat and that the vortex reached the impeller, possibly leading to significant air entrainment and impeller flooding. Clearly the model is not able to capture the formation of small bubble and the impeller flooding regime.

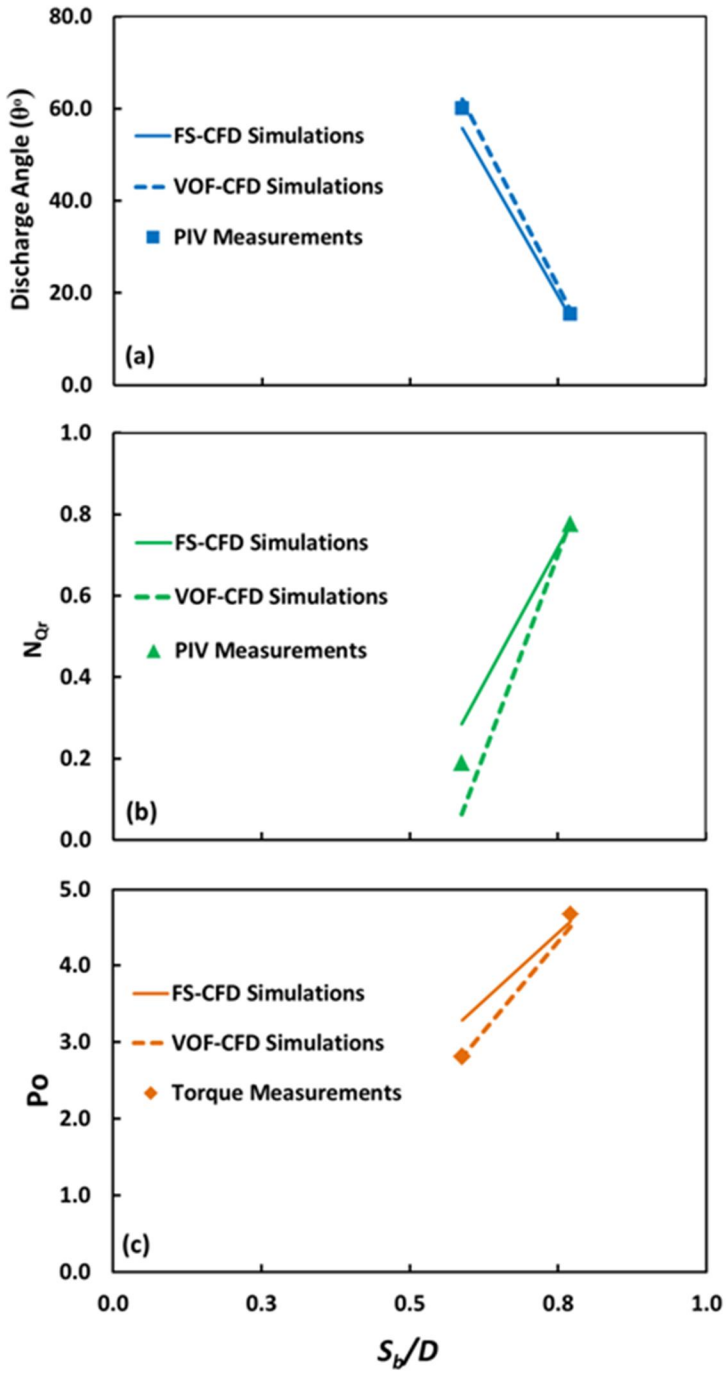

Figure 4.11 Comparison between Impeller discharge angle (a), radial Pumping Number, N_{Qr} (b) and Power Number Po (c) for $S_b/D=0.77$ and $S_b/D=0.59$ predicted by FS-CFD simulation method and VOF-CFD simulation method and experimental results ($C_b/T=0.30$ and $D/T=0.31$).

However, this method clearly predicted the correct vortex depth and shape compared to experimental observations. Additionally, for the same agitation speeds with impeller submergence ratio of 0.77 the interface tracking showed a much less pronounced change in the surface geometry that was exactly matched with the experimental observations. The flow pattern predicted by the VOF-CFD simulation was essentially the same as what was reported in the beginning of this chapter (Figure 4.2) which was based on the flat surface assumption. However, as it can be observed from Figure 4.11a that the VOF-CFD simulation predicted for impeller discharge angle values that were much closer to the experimental values.

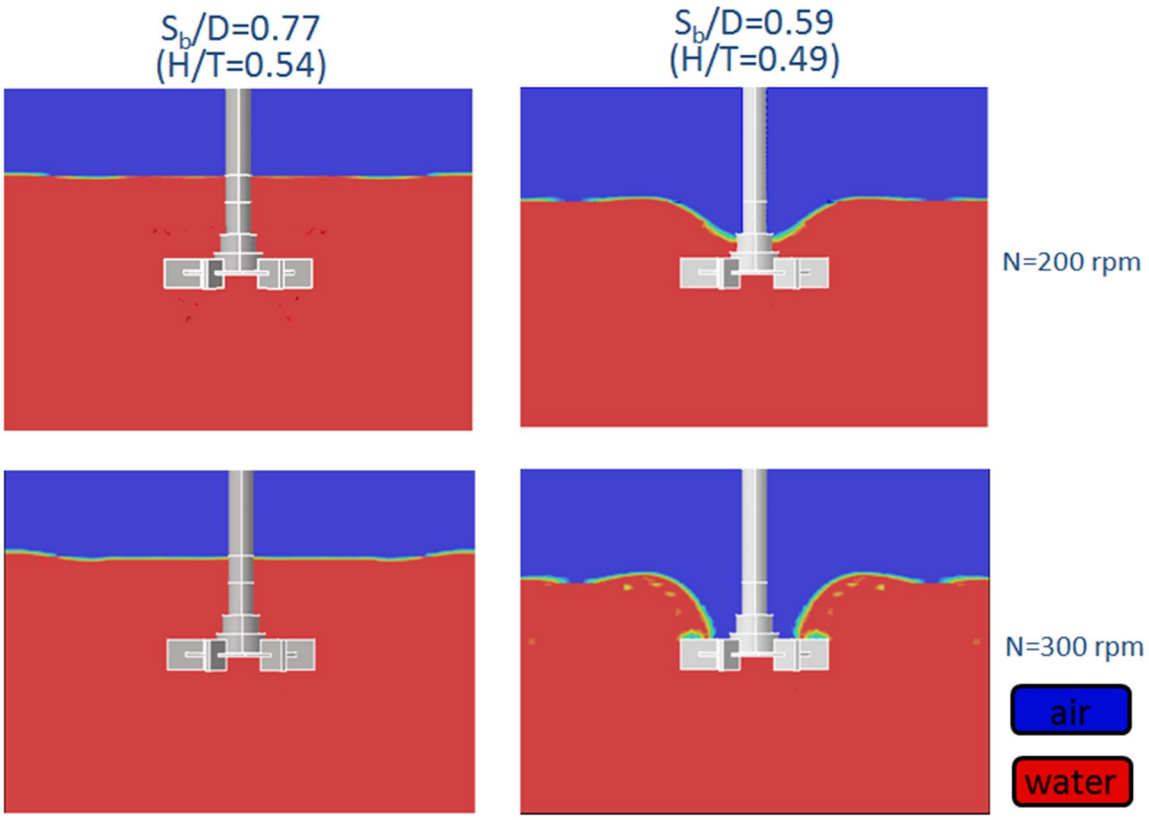

Figure 4.12 Air-liquid interface tracking (VOF-CFD simulation - Phase contour) for S_b/D=0.77 and S_b/D=0.59 at N=200 rpm and 300rpm (C_b/T=0.30 and D/T=0.31).

4.4 Conclusion I

Based on the results presented in this chapter it can be concluded that:

i. For a conventional stirred vessel (H/T=1 and C=T/3), CFD predictions of the velocity components, Power and Pumping Numbers were is significant agreement with experimental measurements and data available in the literature;

ii. The impeller submergence ratio S_b/D, which is a function of the H/T ratio, can play a critical role on the flow regimes produced in stirred vessels when H/T<1

iii. There is a critical impeller submergence ratio (S_{bc}/D) below which:

   a. The macroscopic flow pattern changed by decreasing the impeller submergence ratio from 0.77 to 0.59, transitioning from a “double loop” recirculation flow (DL Regime) to a "single loop-up-pumping" recirculation flow (SL-up Regime)

   b. The Power and radial Pumping Numbers drop significantly in correspondence of this flow transition

iv. Below the critical impeller submergence ratio which resulted in the establishment of the newly described flow regime was not affected by dynamic variables such as agitation speed;

v. Significant surface air entrainment possibly resulting in impeller flooding for low S_b/D liquid system was observed only when; (1) the SL-up Regime was established and; (2) the Froude Number (and consequently the agitation speed) was high enough to create vortex reaching the impeller.

vi. The velocity profiles, contours, Power and Pumping Numbers at different impeller submergence ratios predicted by FS-CFD simulations were in a good agreement with those measured experimentally through PIV. VOF-CFD

simulations were able to predict values that were in closer agreement with the experimental data for lower S_b/D ratios including when surface deformation occurred (S_b/D =0.59).

It should be remarked that this is the first time that such hydrodynamic regime changes have been reported and characterized.

CHAPTER 5

RESULTS AND DISCUSSION II - FLOW REGIMES IN PARTIALLY FILLED STIRRED VESSELS FOR DIFFERENT IMPELLER OFF-BOTTOM CLEARANCES, IMPELLER DIAMETERS, AND FILL RATIOS

As it was discussed in the previous section, a typical radial impeller such as a disk turbine placed in a cylindrical vessel filled with a low viscosity liquid typically produces a "double-loop" recirculation flow (DL Regime), where the fluid flow forms two loops, one above and the other below the impeller. However, if the impeller off-bottom clearance (C_b) is gradually reduced, a flow pattern transition occurs at a critical clearance value, and the lower recirculation loop is suppressed. This transition from "double loop" (DL) to a "single loop-downpumping" recirculation flow (SL-dp Regime) was first described by Nienow (1968) and its importance on process carried out in stirred tanks such as solid suspension behavior was investigated by Armenante et al. (1998) and then by Montante et al. (2001), who simulated this transition.

In this section, the effect of impeller off-bottom clearance (C_b), when the H/T ratio is equal to one and D/T is equal to 0.31, on the flow pattern and different mixing parameters such as Power Number and Pumping Number were investigated first. Then, for each impeller off-bottom clearance the same phenomena were examined at different impeller submergence S_b/D ratios and hence fill ratios (H/T).

5.1 Flow Patterns for H/T=1 at Different C_b/T Ratios

Figure 5.1 shows the flow pattern predicted by FS-CFD simulation for decreasing C_b/T ratios (equal to 0.61, 0.48, 0.30, 0.14 and 0.05). Flow pattern transition from a "double

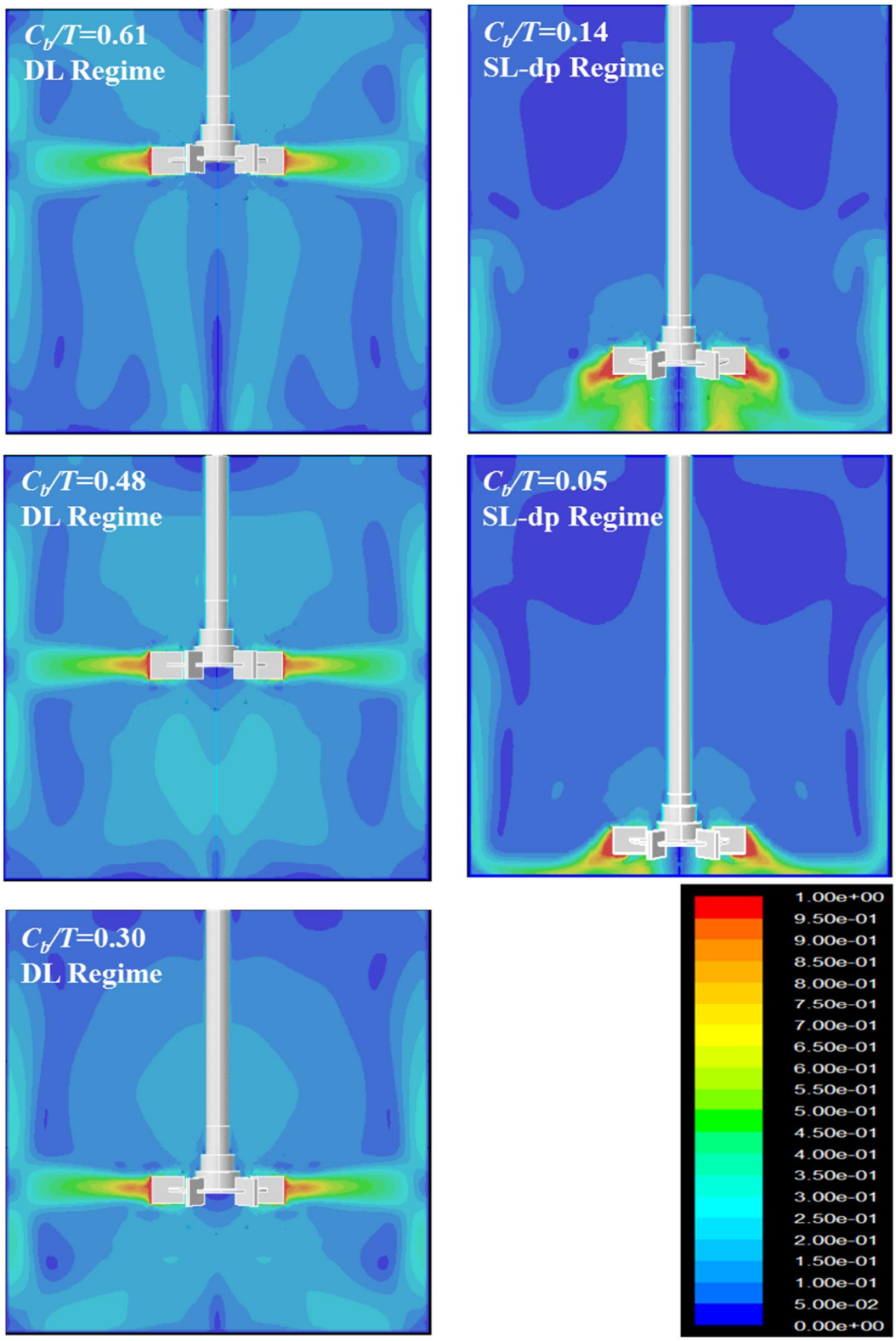

Figure 5.1 FS-CFD prediction of 3D velocity contours for different C_b/T, H/T=1, D/T=0.31, N=300 rpm (U_{tip}=1.2 m/s).

loop" (DL) recirculation flow (one above impeller and one below the impeller), to a "single loop- downpumping" recirculation flow (SL-dp), was observed by decreasing the impeller off-bottom clearance ratio (C_b/T) from 0.30 to 0.14. Montante et al. (2001) were able to predict this flow pattern transition for $C_b/T=0.14$ but only when they used the Sliding Mesh (SM) simulation method which is an unsteady state method and which is more computationally extensive than the approach used in this work. The results shown in Figure 5.1 clearly show that the FS-CFD simulation approach, which is a steady state simulation method, can predict the flow pattern transition accurately when the appropriate mesh size and mesh quality around the impeller and tank bottom are used.

5.1.1 Impeller Discharge Angles, Pumping Numbers and Power Numbers for H/T=1 at Different C_b/T Ratios

The flow regime transition (DL to SL-up Regime) shown in Figure 5.1 is also associated with other changes in the impeller discharge angle, Pumping Number and Power Number, as shown in Figure 5.2 where the average impeller discharge angle, pumping number and power number as a function of C_b/T ratio are reported based on both experimental measurements and FS-CSD simulations methods. The average impeller discharge angles relative to horizontal line are shown in Figure 5.2a for the same impeller off-bottom clearances used in Figure 5.1. For relatively large impeller off-bottom clearances ($C_b/T>0.14$) the average impeller discharge angles were found to be close to zero (PIV measurements for $C_b/T=0.30$, 0.48 and 0.61 were 6.01°, 1.73° and 0.00°, respectively) while for lower impeller off-bottom clearances ($C_b/T=0.14$ and $C_b/T=0.05$) this angle decreased suddenly when the flow pattern changed from the DL Regime to the SL-dp Regime. The impeller discharge angles near the transition point ($C_b/T=0.14$)

calculated by CFD (-23°) and measured by PIV (-20°) are in a good agreement. It is worth mentioning that for $C_b/T=0.14$ Montante et al. (2001) have reported the impeller discharge angle around -20° by PIV. The same C_b/T value was used in this work. However, they predicted via CFD simulation that this value would be about -60° which is far from the real measurements. For a very low impeller off-bottom clearance ($C_b/T=0.05$) while the predicted value and PIV measurements are not as close as in the other cases (predicted angle: -39°; experimentally measured angle: -27°) the trend and the sign has been predicted correctly.

Redial pumping and power numbers as a function of impeller off-bottom clearances are shown in Figure 5.2b and Figure 5.2c, respectively, using both experimental data and computational results. N_{Qr} and Po were nearly constant for impeller off-bottom clearance ratios (C_b/T) equal to 0.61, 0.48 and 0.30. However N_{Qr} and Po were decreased drastically when the impeller off-bottom clearance ratio was decreased from 0.30 to 0.14, which corresponds to the C_b/T range where the flow regime transition occurs changes (DL to SL-dp), as also shown in Figure 5.1. Experimental data and computational predictions of radial pumping and power numbers were in agreement for impeller off-bottom clearance ratios of 0.61, 0.48 and 0.30. However, these dimensionless numbers were slightly under predicted by FS-CFD simulations for C_b/T equals to 0.14 and 0.05. The difference between computational predictions and experimental measurements of impeller discharge angles, radial pumping numbers and power numbers in the case of low impeller off-bottom clearances (Cb/T=0.14 and 0.05) could be attributed to the highly anisotropic turbulence level between the impeller and the tank bottom which cannot be predict well by the k-ε model.

Previous work has shown (and will be discussed in Chapter 6) that solid suspension occurs at lower agitation speed when the impeller is closer to the tank bottom and the SL-dp Regime is present.

5.2 Flow Regimes for Different Combinations of C_b/T and S_b/D Ratios

After examining the effect of C_b/T ratios on flow pattern for H/T=1, the effect of S_b/D (and hence the fill ratio H/T) at each of C_b/T ratio was examined. Figure 5.3 shows the velocity contour plots at the liquid level where the flow regime transition was observed when decreasing S_b/D ratio for all the impeller off-bottom clearances shown in Figure 5.1. In this portion of the work, three different flow pattern transitions were observed:

(1) from a "double loop" recirculation flow (DL Regime) to a "single loop-up-pumping" recirculation flow (SL-up Regime) for “high” C_b/T ratios (and corresponding impeller off-bottom clearance ratios equal to 0.61, 0.48 and 0.3);

(2) from a "single loop-downpumping" recirculation flow (SL-dp Regime) to a” single loop-uppumping" (SL-up) recirculation flow (SL-up Regime) for “low” C_b/T ratios (and corresponding impeller off-bottom clearance ratios equal to 0.14);

(3) from a "single loop-downpumping" recirculation flow (SL-dp Regime) to a” no circulation" flow (NC Regime) for “very low” C_b/T ratios (and corresponding impeller off-bottom clearance ratios equal to 0.05).

The first type of flow transition, also observed for the case of C_b/T=0.3, has been discussed extensively in Chapter 4. The other two flow transitions are discussed in greater detail in this chapter.

The Power Number, Po, was also used to study the effect of impeller submergence on flow regime transition at different impeller off-bottom clearances. Po as a function of impeller submergence ratio was calculated using both FS-CFD simulations and experimental torque measurements. Experimental data were collected from H/T=1 down to when the impeller submergence was equal to zero (S_b=0), whereas computational predictions were obtained for H/T=1 and at other H/T values until the flow pattern transition occurred. The results are shown in Figure 5.4. One can see that a good agreement between computational and experimental results generally exists. In addition, the results presented in Figure 5.3 show that for any impeller off-bottom clearance there is a critical impeller submergence ratio (S_b/D) below which the Power Number decreases suddenly. These sudden changes have been found to correspond to the same levels when flow regime transition occurred.

In general, in this portion of the work it was found from both the FS-CFD simulations and PIV measurements that for each impeller off-bottom clearance there is a minimum impeller submergence ratio (S_b/D) below that flow pattern changed. In addition, by decreasing the impeller off-bottom clearances (C_b/T) the operating window in which stirred vessels could be operated in either the DL Regime or SL-dp Regimes became wider.

5.2.1 Flow Pattern Transition from DL Regime to SL-up Regime

As already mentioned above, the flow pattern transition from Double Loop Regime to Single Loop uppumping Regime occurred when the impeller had a relatively high value of the C_b/D ratio, i.e., in a region where the impeller was sufficiently high in the tank to begin with so that the DL Regime was dominant, provided that the impeller submergence

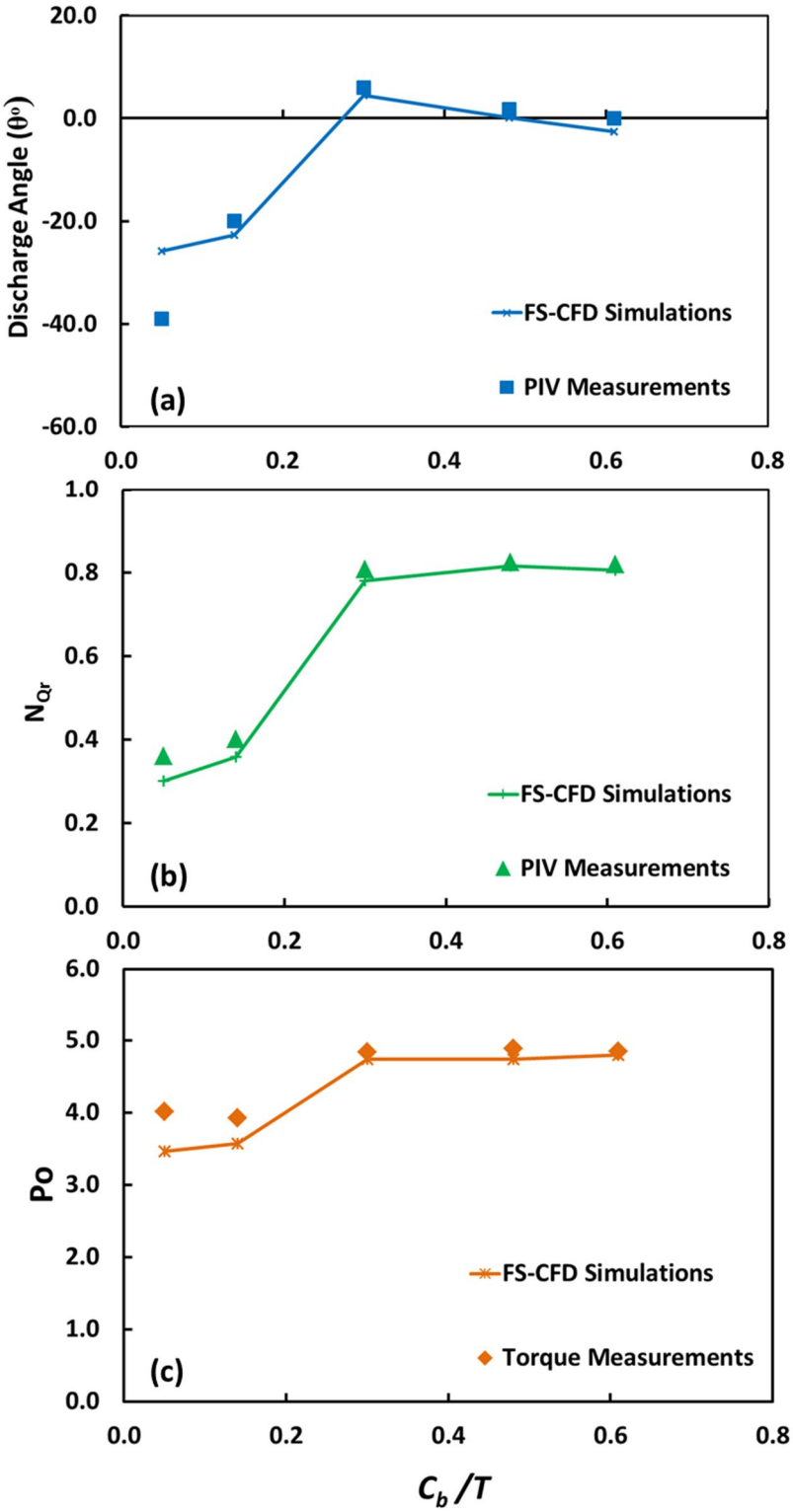

Figure 5.2 (a) Impeller discharge angle, (b) radial Pumping Number, N_{Qr} and (c) Power Number, Po for different C_b/T, H/T=1, D/T=0.31 and N=300 rpm (U_{tip}=1.2 m/s) calculated from both experimental and FS-CFD simulation data.

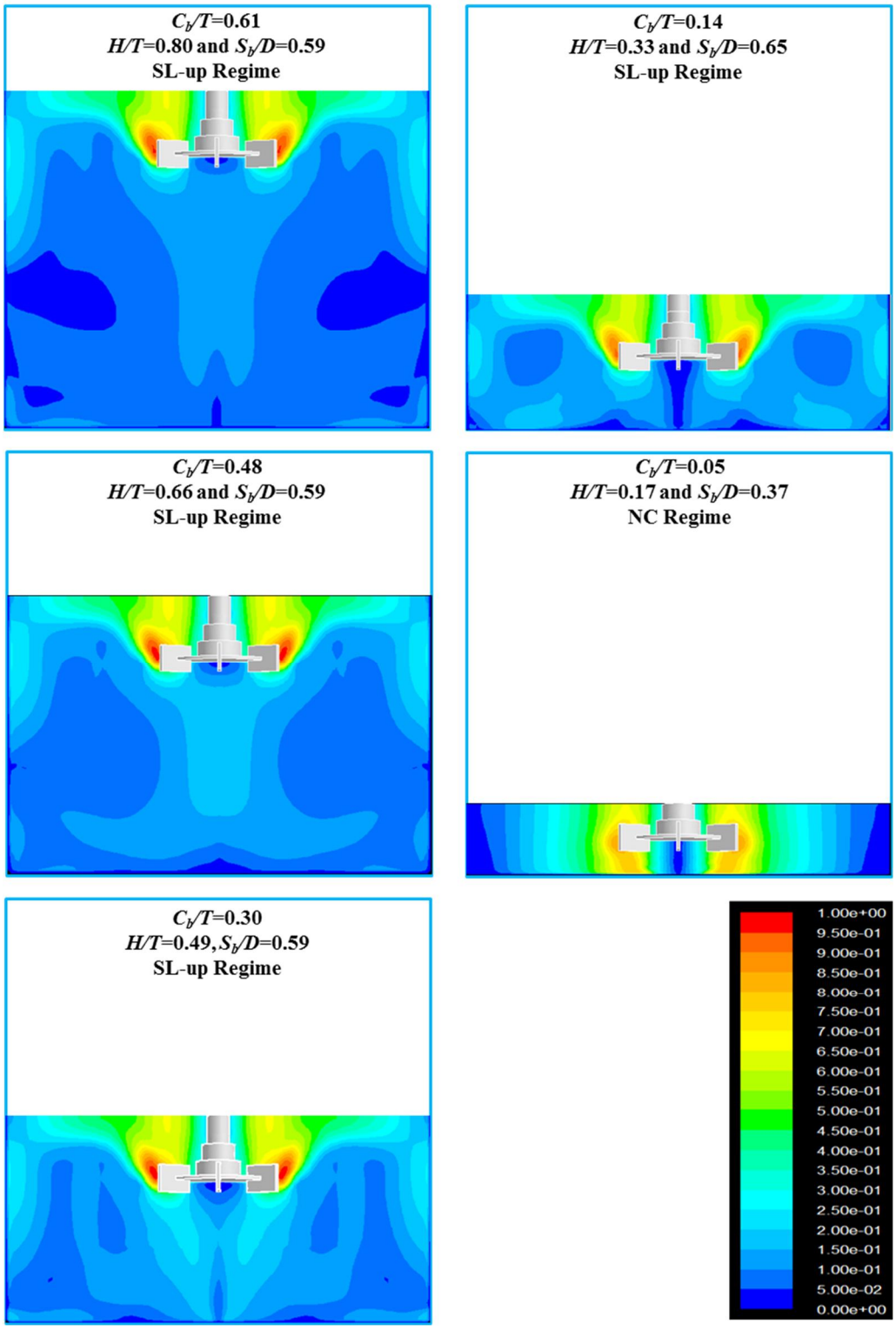

Figure 5.3 FS-CFD simulation results for 3D velocity contours after transition in flow regime from: (1) DL to SL-up for C_b/T=0.61, 0.48 and 0.30; (2) SL-dp to SL-up for C_b/T=0.14; (3) SL-dp to NC for C_b/T=0.05 when H/T=1, D/T=0.31 and N=300 rpm (U_{tip}=1.2 m/s).

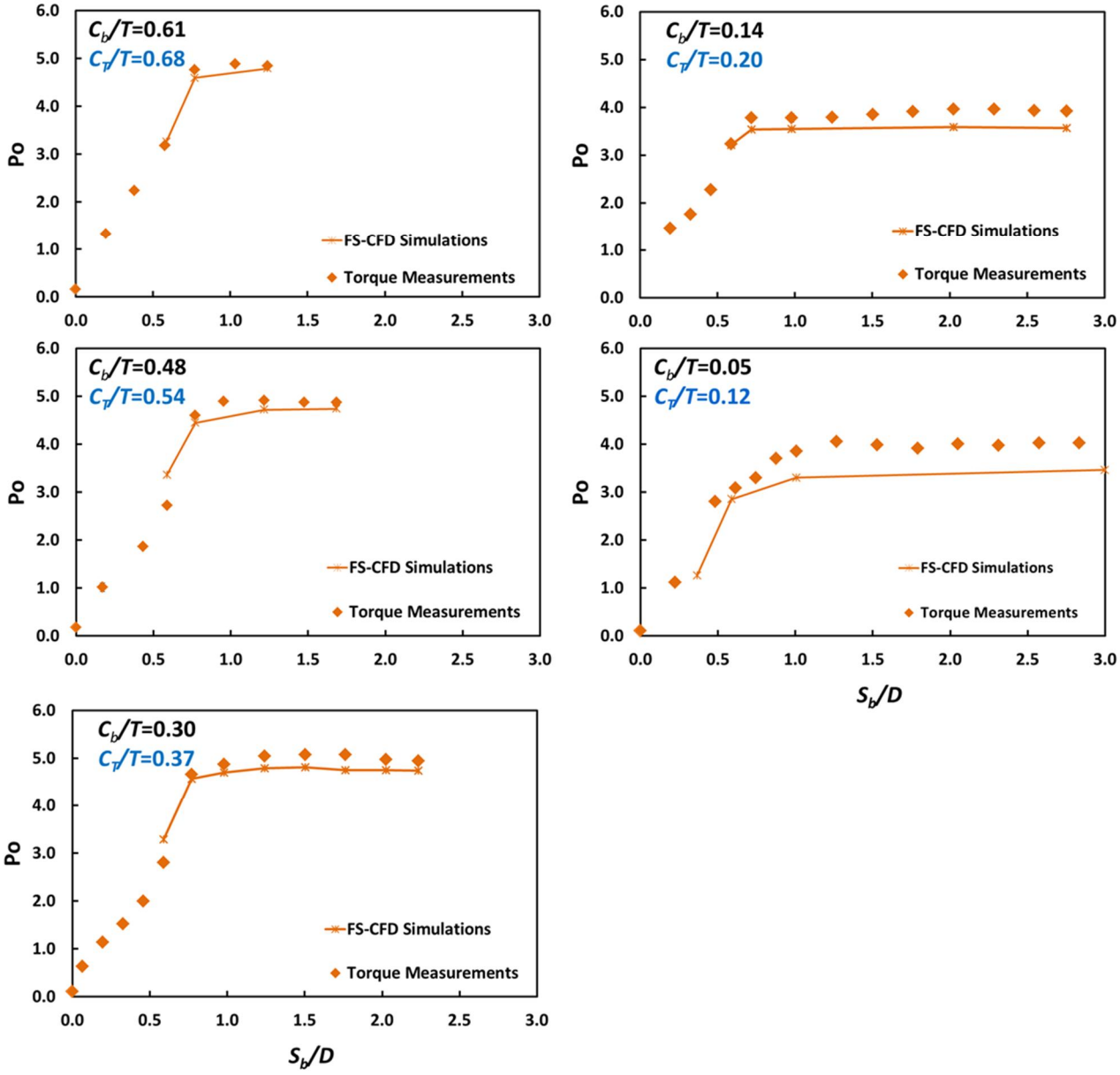

Figure 5.4 Power number for different S_b/D at different C_b/T ratios, D/T=0.31 and N=300 rpm (U_{tip}=1.2 m/s) calculated from both experimental and FS-CFD Simulation data.

was high enough (left-hand panels in Figure 5.1). As the S_b/D ratio was decreased, the DL Regime still prevailed until a critical value of the S_b/D was reached and the flow transition to SL-upwards occurred suddenly (left-hand panels in Figure 5.3) at $S_b/D=0.59$. The critical submergence ratio at which the flow transitions occurred for these three C_b/T ratios (0.61, 0.48 and 0.30) was found to be equal to 0.77. It is clear that this transition happens at lower fill ratio for the lower impeller off-bottom clearance. This phenomenon was described in some detailed in Chapter 4 for $C_b/T=0.3$.

5.2.2 Flow Pattern Transition from SL-dp Regime to SL-up Regime

In this section, the flow regime transition was studied starting with an impeller off-the-tank-bottom position that was already low enough to generate a Single Loop-dowpumping flow to start with, even at high submergence ratios. The case specifically examined was that for which $C_b/T=0.14$.

The experimentally measured velocity profiles at N=200 rpm for different filling ratios are shown in Figure 5.5. The flow transition from SL-dp Regime to SL-up Regime occurred when the impeller submergence ratio (S_b/D) was lowered from 0.77 to 0.64, as clearly evidenced by the flow direction of the velocity vectors in the loop.

Figure 5.6a and b show, respectively, the impeller discharge angle and the radial Pumping Number for the same impeller off-bottom clearance as a function of impeller submergence ratio. These figures contain results from both PIV measurements and FS-CFD simulations. Both methods show that sudden changes in the impeller discharge angles and the radial Pumping Numbers occurs when S_b/D drops from to 0.77 to 0.64, i.e., in correspondence of the flow regime transition. The computational predictions and experimental data are in a good agreement with each other. However, by comparing these

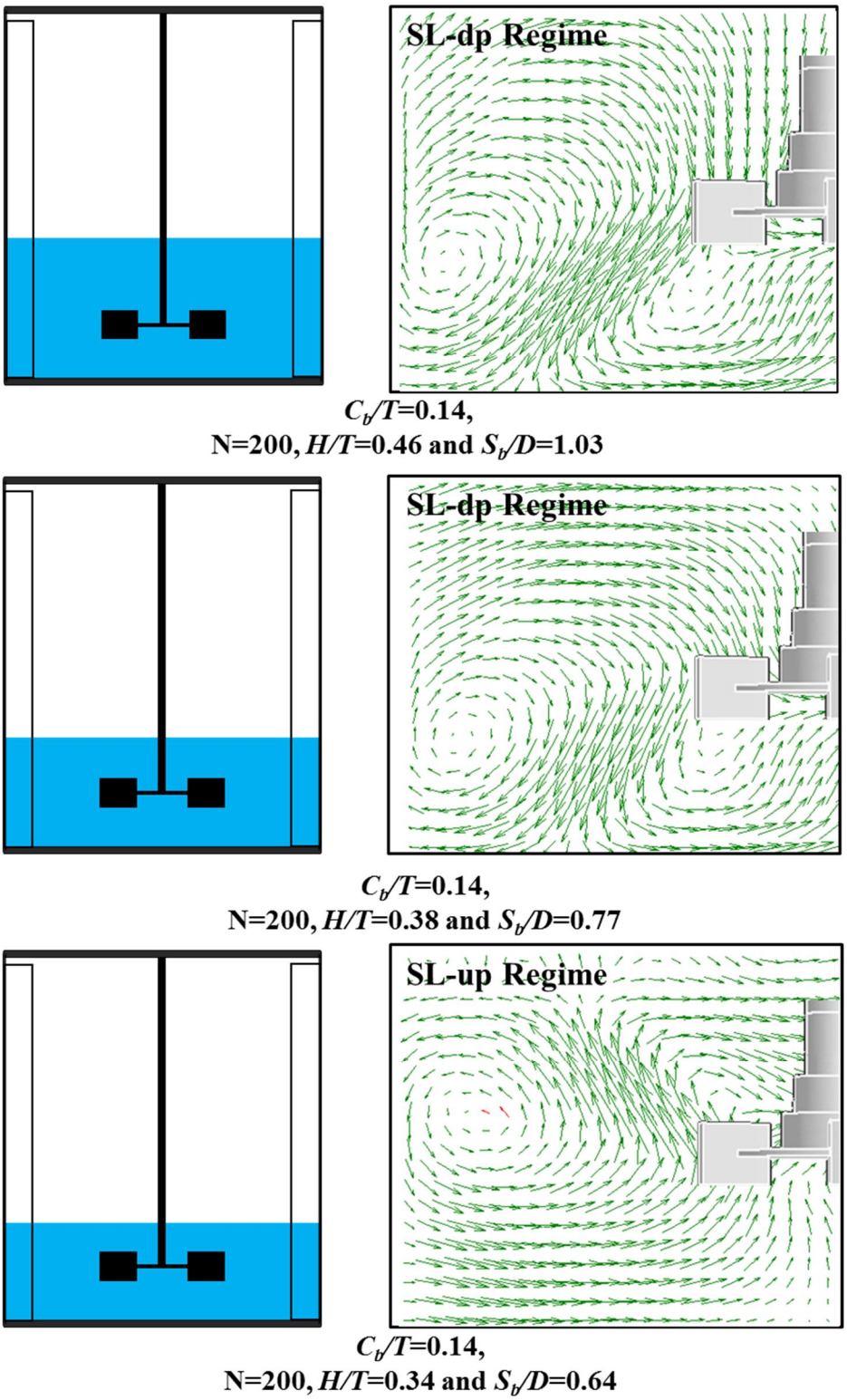

Figure 5.5 PIV measurement of 2D velocity vectors for different S_b/D ratios, C_b/T=0.14, D/T=0.31 and N=200 rpm (U_{tip}=1.2 m/s).

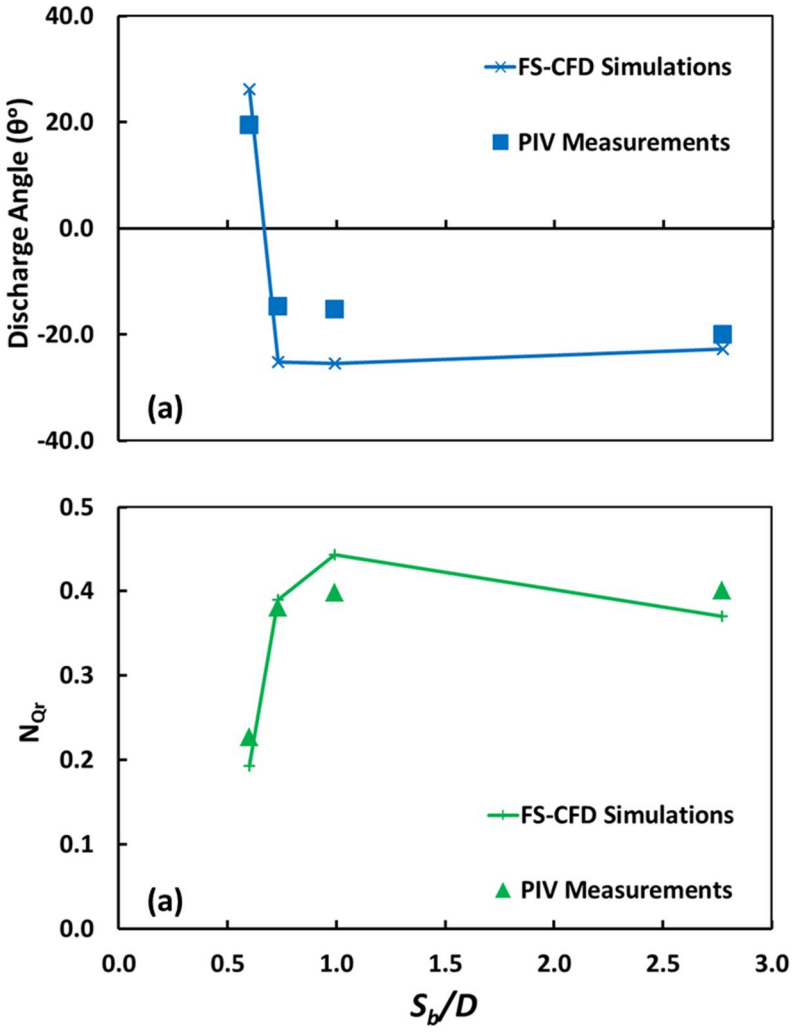

Figure 5.6 (a) Impeller discharge angle and (b) radial Pumping Number, N_{Qr} for Different S_b/D, D/T=0.31, N=200 rpm (U_{tip}=0.8 m/s) and C_b/T=0.14 calculated from both experimental and FS-CFD simulation data.

graphs with the same graphs for C_b/T equals to 0.30 presented in the Chapter 4 (Figure 4.4) it is clear the FS-CFD predictions for C_b/T equals to 0.30 are in better agreement with experimental results. This could be explained by the high anisotropic turbulence level in the region between the impeller blades and the tank bottom, which cannot be perfectly simulated by the k-ε model.

The effect of these flow regime transitions on the overall mixing performance and solid suspension performance is reported in Chapter 6.

5.2.3 Flow Regime Transition from SL-dp Regime to NC Regime

As already reported in Figure 5.3, a "No Circulation" (NC) Regime was predicted by FS-CFD simulations when the impeller was at a very low position in the tank ($C_b/T=0.05$) and the impeller submergence ratio dropped to a very low level ($S_b/D=0.37$). The PIV data obtained with this impeller clearance for three impeller submergences are confirm these predictions and presented in Figure 5.7. For $S_b/D= 1.27$ and 0.48, the "Single Loop-downpumping" (SL-dp) Regime was observed. However, when $S_b/D=0.37$ no clear recirculation pattern could be observed (NC Regime). These results show a very good agreement between results from CFD simulations and PIV measurements.

These results are not unexpected. The previously shown results obtained at higher C_b/T values showed that when the impeller submergence is decreased below a critical value, the impeller begins to pump upwards (SL-up Regime), and the pumping loop closes itself by "feeding" the impeller from below. However, when the impeller is very close to the tank to begin with the impeller cannot close the recirculation loop this way. The result is a catastrophic drop in the pumping ability of the impeller, which is now only able to splash the surrounding fluid around without generation a real pumping action. In other words, when impeller is very close to the tank bottom there is not enough space on the lower portion of the impeller for any possible uppumping circulation flow be established. Therefore, instead of flow regime transition from SL-dp to SL-up, SL-dp to NC happens.

It is interesting to notice however, that the flow transition for this case ($C_b/T=0.05$) happens at much lower impeller submergence ratio ($S_b/D=0.48$). This means that the operating window, in terms of S_b/D, in which a stirred vessel can be operated without losing entirely its pumping action, is wider at very low impeller clearances than in other cases when the impeller is higher in the tank.

Another important observation here is that the flow regime observed during the PIV experiments was somewhat unstable as the critical submergence before the NC Regime was approached. Occasionally the beginning of an uppumping action could be observed. However, these bursts were never stable. By contrast, the FS-CFD simulations never predicted any SL-up Regime for $C_b/T=0.05$.

The radial Pumping Numbers obtained at $C_b/T=0.05$ with FS-CFD simulations and PIV measurements are presented in Figure 5.8 for three impeller submergence ratios. N_{Qr} was not calculated for $S_b/D=0.37$ since no circulation flow was observed for this liquid level. The results indicate that a good agreement exists between the computational predictions and the experimental results for $S_b/D=3.04$ and 1.27. However, for $S_b/D=0.48$ the computational results over predicted N_{Qr} ($N_{Qr}=0.15$ with the FS-CFD simulations and $N_{Qr}=-0.02$ with PIV measurements). A negative value for N_{Qr}, as measured by PIV, would imply that instead of pumping radially the flow next to the blades is pointing inwards. This is clearly difficult to imagine. However, the value of -0.02 is very close to zero which means the impeller pumping action was lost even at $S_b/D=0.48$.

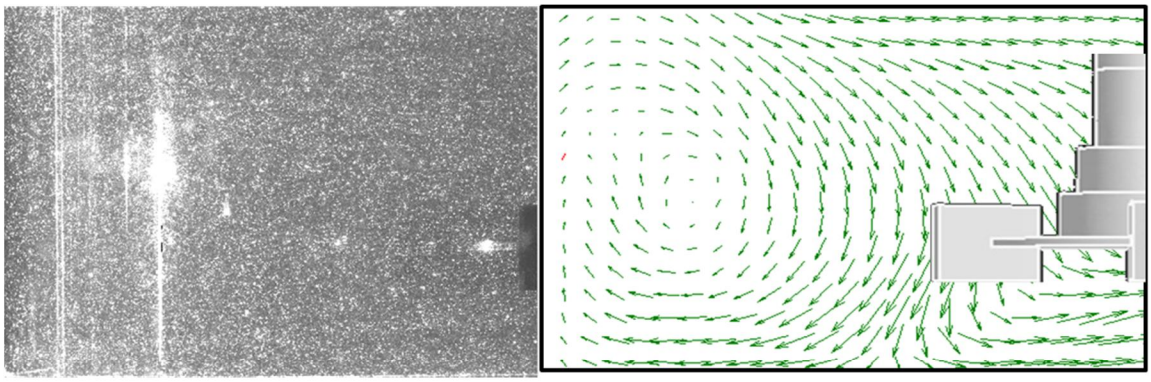

C_b/T=0.05,
N=200, H/T=0.45 and S_b/D=1.27

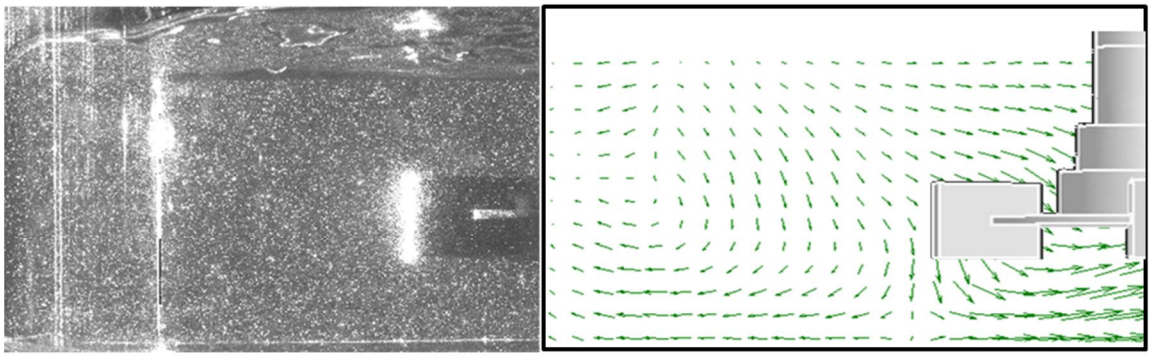

C_b/T=0.05,
N=200, H/T=0.20 and S_b/D=0.48

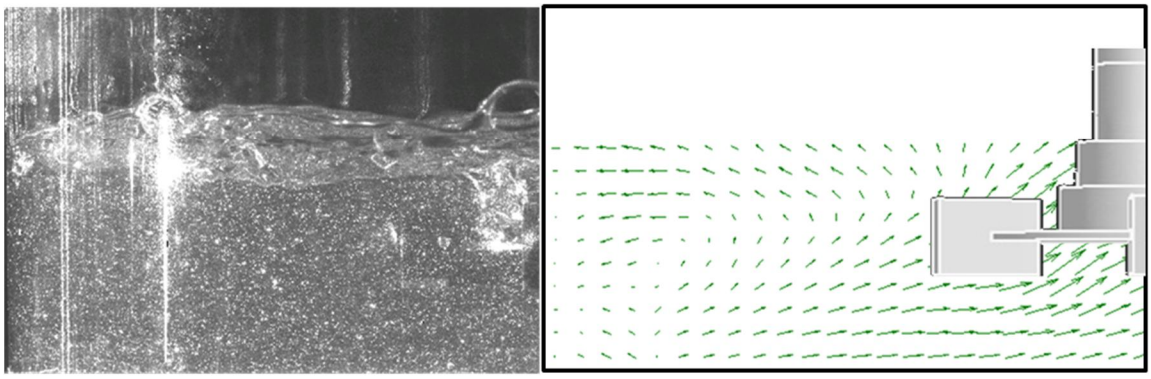

C_b/T=0.05,
N=200, H/T=0.17 and S_b/D=0.37

Figure 5.7 PIV measurement of 2D velocity vectors for different S_b/D ratios, C_b/T=0.05, D/T=0.31 and N=200 rpm (U_{tip}=0.8 m/s).

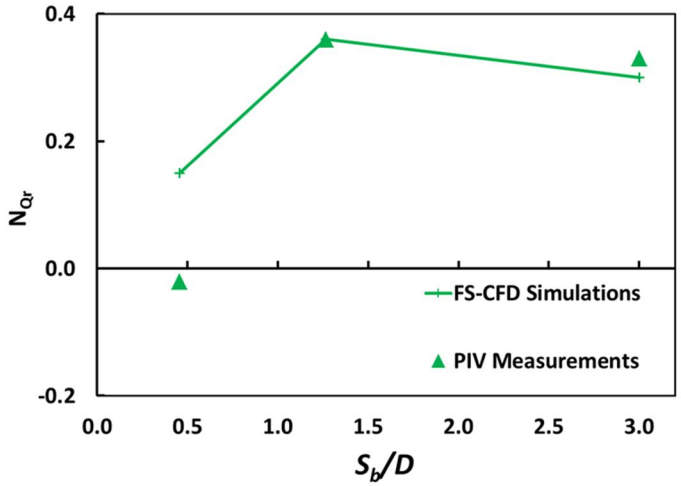

Figure 5.8 Radial Pumping number, N_{Qr} for Different S_b/D, D/T=0.31, N=300 rpm (U_{tip}=1.2 m/s) and C_b/T=0.05 calculated from both experimental and FS-CFD simulation data.

5.2.4 Summary of Flow Regimes and Regime Transitions for Different C_b/T and S_b/D Ratios

S_{bc}/D can be defined as the critical submergence ratio at which a flow transition occurs for a given C_b/T ratio. For any given system, once S_{bc}/D is determined the corresponding critical fill ratio H_c/T (where H_c refers to the critical liquid level below that flow regime transition occurs) is also known.

Table 5.1 presents a summary of the results obtained for this section in terms of critical submergence ratio. In general, the critical submergence level was found to be constant and equal to 0.77 for a D/T ratio equal to 0.31. However, when the impeller was very close to the tank bottom (C_b/T=0.05) the critical submergence ratio was only 0.48. This phenomenon can probably be attributed to the interaction of the impeller with the tank bottom effect. Placing the impeller very close to the tank bottom increases the magnitude of this interaction.

In all cases except for very low impeller locations ($C_b/T<0.05$), flow transition implies switching to the SL-up Regime. This regime is not directly responsible for surface air entrainment and possible impeller flooding. However, the establishment of this regime is a necessary prerequisite for significant surface air entrainment to occur, since the low recirculation zone near the impeller shaft generated by the SL-up Regime can be easily produce a vortex at higher agitation speed which then lead to air entrainment and flooding.

When the impeller location is very low ($C_b/T<0.05$) the critical submergence ratio was lower ($S_{bc}/D=0.48$). However, when flow transition occurred, the new regime (NC Regime) did not produce any flow and the ability of the impeller to be an effective mixer was lost.

Table 5.1 Critical Fill Ratios and Impeller Submergence Ratios for Different C_b/T

C_b/T	**H_c (m)**	**H_c/T**	**S_{bc} (m)**	**S_{bc}/D**
0.05	0.06	0.24	0.05	**0.48**
0.14	0.09	0.38	0.06	**0.77**
0.30	0.134	0.54	0.059	**0.77**
0.48	0.176	0.72	0.059	**0.77**
0.61	0.202	0.82	0.059	**0.77**

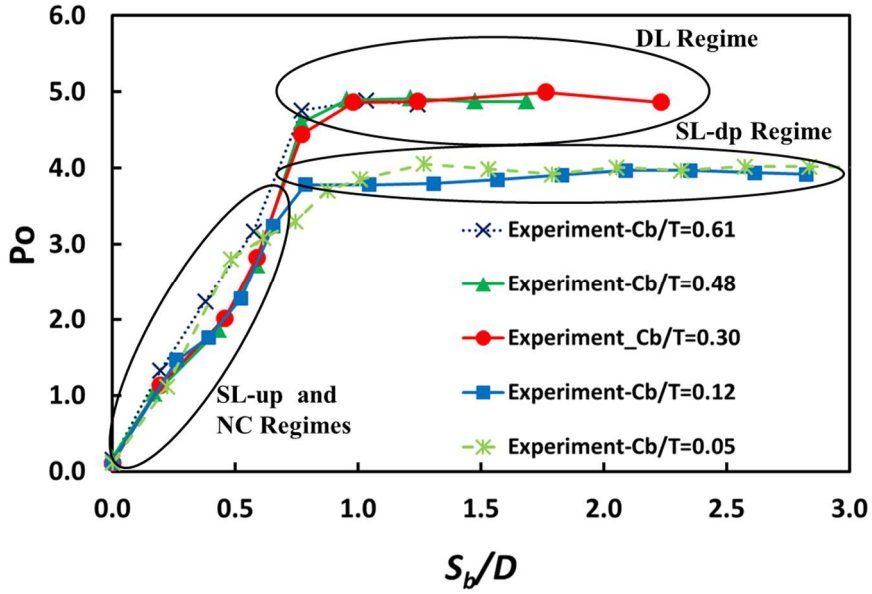

Figure 5.9 Power numbers obtained experimentally for different S_b/D at different C_b/T, D/T=0.31 and N=300 rpm (U_{tip}=1.2 m/s).

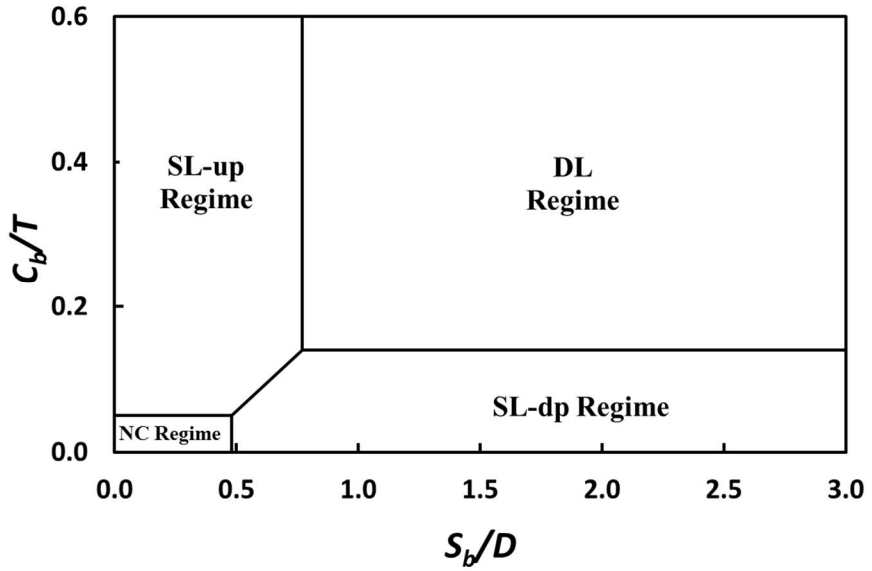

Figure 5.10 Regime diagram obtained experimentally for different S_b/D at different C_b/T, D/T=0.31 and N=300 rpm (U_{tip}=1.2 m/s).

Additional evidence to show the critical importance of S_b/D ratio on flow pattern transition is presented in Figure 5.9 where the Power Number was plotted against S_b/D keeping the C_b/T ratio as a parameter. All experimental power data for different impeller

off-bottom clearances were combined to show that the transition between the different regimes is always associated with sudden changes in power number. In this figure, the NC Regime overlapped with the SL-up Regime. However, the NC Regime was only observed for very at low impeller off-bottom clearance ($C_b/T=0.05$). This figure shows that the detection of a sudden power change can be used as an experimental indication that flow transition has occurred. This may be important in full-scale tanks where it is hard to visually observe the phenomenon. In addition, the flow regime diagram can be used as a guide to determine in which regime the system is operating.

5.3 Flow Pattern and Power Numbers for Different D/T and S_b/D Ratios

After examining the effect of C_b/T on flow pattern in partially filled stirred vessels, power numbers and pumping numbers, the same phenomena was studied for different impeller diameter-to-tank diameter (D/T) ratios. The Power Number has been shown here to be closely associated with flow pattern transitions. In this section Power Number measurements along with visual observations were used to study the effect of D/T and S_b/Don the flow regimes and flow pattern transition.

Five combinations of Disk Turbine impellers and flat bottom vessels were used. The diameters of the impellers and vessels used in this section were summarized in Table 5.2. Dimensional details of these impellers and vessels have been presented in Table 2.1 and Table 2.2, respectively. The C_b/T ratio was always equal to 0.30 and impeller tip velocity, U_{tip} was kept constant at 1.2 m/s irrespective of scale. Power Numbers were determined using the on torque transducers data for different D/T value and impeller submergence ratios. In addition, while collecting experimental power data attention was

paid to detect any flow pattern transition. Changes in flow pattern were verified visually by adding some colored, nearly neutrally buoyant particles that follows the flow closely.

Table 5.2 Diameter of the Impellers and Vessels used in this Section

Tank Diameter (**m**)	Impeller Diameter (**m**)	**D/T**
0.246	0.064	0.42
0.246	0.077	0.31
0.246	0.103	0.26
0.294	0.127	0.43
0.585	0.127	0.22

The results for all cases are presented in Figure 5.11 in terms of Power Number as a function of S_b/D ratio keeping D/T as a parameter. All the curves in this figure show that the Power Number was constant for high values of the S_b/D ratio, and that Po was about 5 independently of the D/T ratio (although the value for each D/T ratio were different). This figure also shows that Po decreased when the S_b/D ratio was lowered below a critical value of this variable, S_{bc}/D, which depended on the D/T ratio. In all cases a flow pattern transition from DL Regime to the SL-up Regime observed when the Power Numbers began their sudden decrease.

Such flow pattern transitions occurred when the impeller submergence ratios were between the dashed lines shown in that figure. The critical submergence ratio S_{bc}/D was larger (1.2) for smaller D/T ratios (0.22) and smaller (0.54) for higher D/T ratios (0.43).

This effect could be explained by wall-impeller interaction effect. When the D/T ratio is larger, wall-impeller interaction is stronger. Therefore, tendency toward DL Regime is higher and flow regime changes (DL to SL-up) occurs at a lower impeller submergence ratio compared to when the stirred tank is equipped with a smaller D/T impeller. The stronger tendency toward DL Regime for higher D/T has been also reported by Armenante and Nagamine (1998) and Li et al. (2010). Higher D/T ratios required slightly lower C_b/T values for the flow transition to take place. Li et al. (2010) proved this by conducting Large Eddy simulation and PIV measurements.

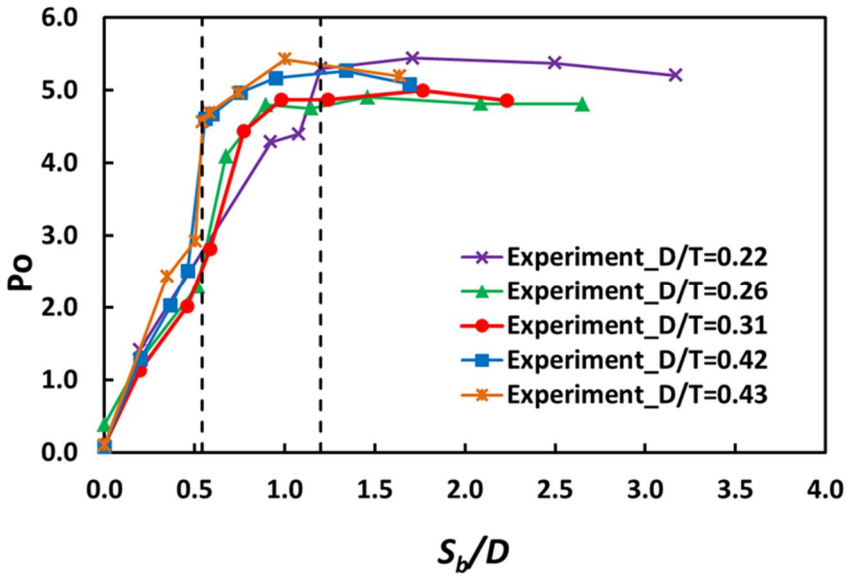

Figure 5.11 Power numbers obtained experimentally for different S_b/D at different D/T, U_{tip}=1.2 m/s and C_b/T=0.30.

5.4 Effect of Agitation Speed on Flow Pattern, Air Entrainment and Impeller Flooding

The effect of agitation speed on flow pattern transition as a function of impeller submergence ratios has already been reported in Chapter 4 for D/T=0.31. In Figure 5.12, graphs of Power Number as a function of Froude number and agitation speed are shown

for four different impeller submergence ratios (S_b/D), i.e., one above the critical submergence level for flow transition, one at the critical level, and two below the critical level. The power measurements were taken at five different agitation speeds (100 rpm, 200 rpm, 300 rpm, 400 rpm and 500 rpm) for all the cases shown in Figure 5.12. The third panel in this figure (D/T=0.31) is identical to the figure presented in Chapter 4 (Figure 4.8) and it repeated here for comparison purpose.

A number of phenomena can be observed in this figure. When the S_b/D ratio was sufficiently high ($S_b/D \geq 0.74$ at any D/T ratio), all impeller were high enough in the tank to operate in the DL regime. When this was the case, the Power Number remained constant as the agitation speed increased and hence the Froude Number also increased (top curves in all panels). A relatively small drop in Po was observed with increasing agitation speed, but only with large D/T impeller. This phenomenon was associated with the entrainment of small air bubbles from the entire surface of the tank. These bubbles were very small and the impeller was able to distribute them somewhat uniformly throughout the vessel (i.e., no flooding occurred). This pattern remained unchanged when the liquid level was dropped to reach just above the critical submergence level (second curve from top in all panels). However, as soon as the liquid level dropped below the critical S_{bc}/D value, the regime changed to SL-up and the power dropped accordingly (third curves in each panel) to reach a value of about 4, provided that the agitation speed was low enough to avoid significant air entrainment near the shaft. The first and second points in the third and fourth curves in each panel show this. When the agitation speed was further increased, air began to be entrained at the shaft and the power started to drop very significantly with agitation speed (third and fourth curves in each

panel). Eventually the impeller became flooded and the Power Number approached an asymptotic lower limit value, typically at or below Po=1. Such phenomenon was observed for all D/T ratios.

Seen from a different angle, the power reduction observable in the panels in Figure 5.12 can be attributed to three different phenomena. The gentle and relatively small drop in Po at high S_b/D values is caused by the entrainment of small air bubbles from the entire (flat) air-liquid surface. This is evident for large D/T ratio impeller as the agitation is increased. A sudden but contained drop in Power Number (from about 5 to about 4) can be observed in all panels when S_b/D drops below the critical value and the flow transitions to the SL-up Regime. This is observable for low agitation speeds in all panels (for example when N=100 rpm for D/T= 0.42 and 0.43 and up 200 rpm for lower D/T ratios). This drop is only attributable to the regime change and not to air entrainment since the agitation speed is too low. Finally, a third and much more drastic reduction in Po occurs when the impeller is in the SL-up regime and the agitation speed is increased. This power drop can be attributed to massive air entrainment originating from the center of the vessel, as a vortex start developing, and eventually result in impeller flooding if the vortex reaches the impeller.

It can be concluded that impeller flooding from surface air entrainment occurs when both of the following conditions are satisfied: (1) S_b/D is low enough to produce SL-up Regime; and (2) the Froude Number is high enough to create a vortex reaching the impeller. For relatively high impeller submergence, vortex formation is not an issue in baffled stirred vessels even for high agitation speed. However, the experimental observation showed that for low impeller submergence (SL-up Regime) vortex formation

was observed. This vortex depth increased as agitation speed has been increased. When this vortex reached the impeller disc the impeller flooding regime started and as a result of that power number decreased drastically.

Figure 5.13 shows a summary of the results at different D/T ratios in terms of Power Number as a function of S_b/D ratio. Po was taken at an agitation speed low enough so that air entrainment did not occur for any of the cases shown in this figure. The first top five curves in this figure are for C_b/T=0.30 and produce a flow transition from the DL Regime to SL-up Regime which is clearly associated with a drop in Po. However, the last curve refers to C_b/T=0.14. Here a flow transition from the SL-dp Regime to the SL-up Regime occurred, which was also accompanied by a drop in Po. For the former flow transition (C_b/T=0.30) the Power Number went from 5.02 to 4.13, 4.71 to 4.02, 4.88 to 3.98, 5.02 to 4.13 and 4.70 to 3.90 for D/T=0.22, 0.26, 0.31, 0.42 and 0.43, respectively. For the latter flow transition (C_b/T=0.14) Po went from 4.03 to 3.75. These Power Numbers reduction are associated only with flow pattern transition and not with surface aeration effects.

Finally, Figure 5.14 shows some experimental photographs taken while the power measurement was conducted: For the case of D/T=0.22 and Fr=0.58 (Figure 5.14a), the Power Number dropped from 5.30 to 4.29 while the S_b/D ratio decreased from 1.2 to 0.98, respectively. This reduction can be explained as a result of both flow pattern changes and surface air entrainment impeller eventually resulting in impeller flooding for S_b/D=0.92. For the case of D/T=0.43 and Fr=0.58 (Figure 5.14b), the Power Number decreased from 4 to 1.5 when the S_b/D ratio was redused from 0.58 to 0.50, respectively (these numbers could be read from Figure 5.14).

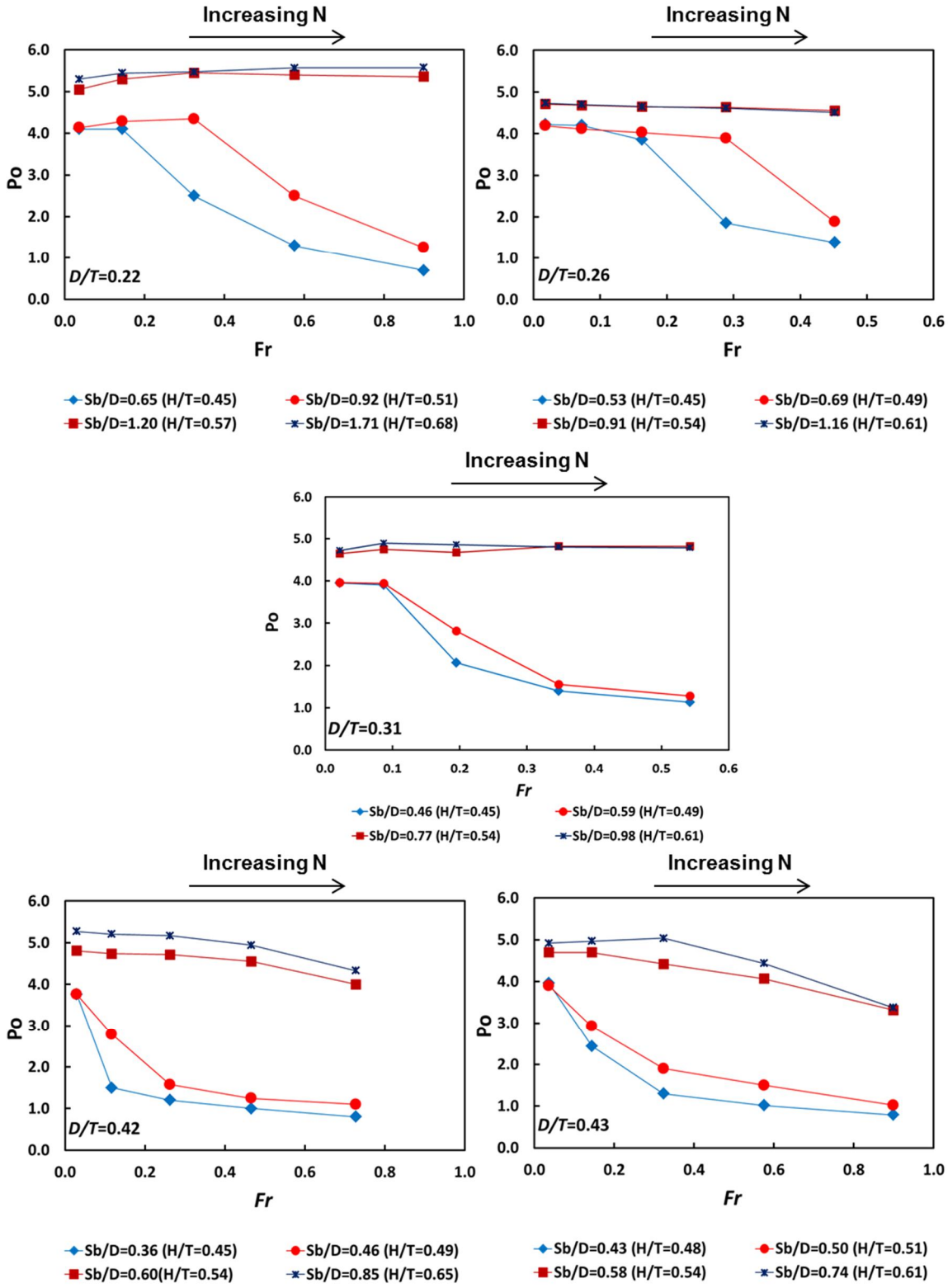

Figure 5.12 Power number as a function of Froude Number for different S_b/D at different D/T values; U_{tip}=1.2 m/s and C_b/T=0.3.

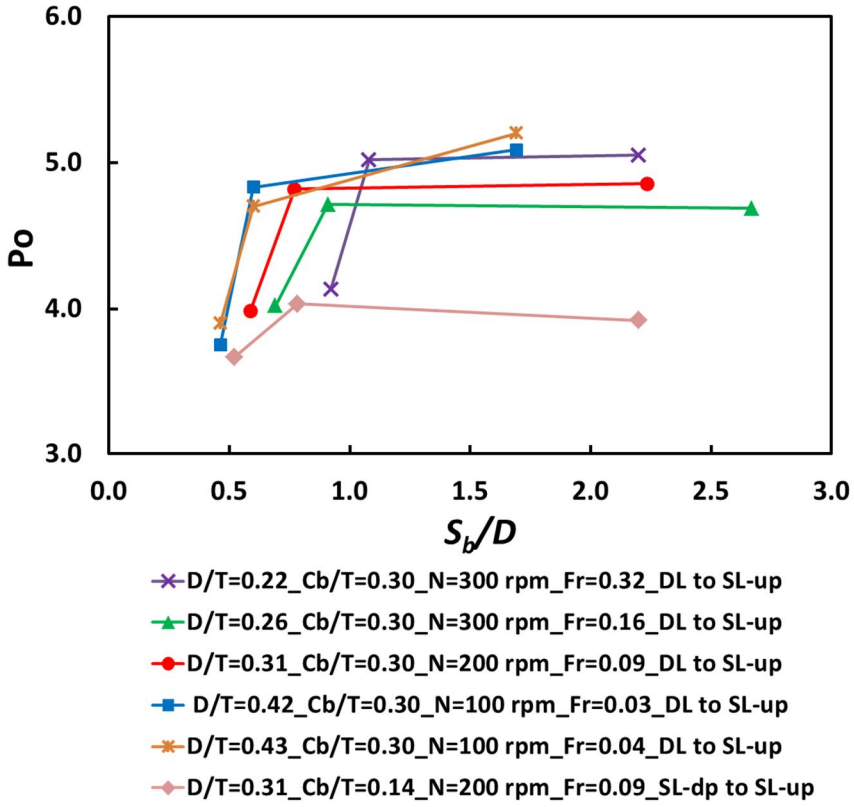

Figure 5.13 Power numbers reduction as a result of transition in flow regime (either from DL Regime to SL-up or from SL-dp Regime to SL-up) without any surface air entrainment.

This could be explained as a result of both a change in flow pattern and surface aeration leading to impeller flooding for S_b/D=0.50. The important observation here is that when impeller flooding occurred (for both D/T equal to 0.22 and 0.43), the entrained air bubbles remained in the upper portion of the vessel. No bubbles were observed in the bottom of the tank. Additionally, water began to splash outside the vessel for D/T=0.43 and S_b/D=0.5. A comparison of Figure 5.14a and Figure 5.14b (before and after flow transition, respectively, i.e., from DL Regime to SL-up Regime) clearly shows many more bubbles inside the vessel in the latter figure for which D/T=0.43. The Power Number reduction was much more pronounced for this case.

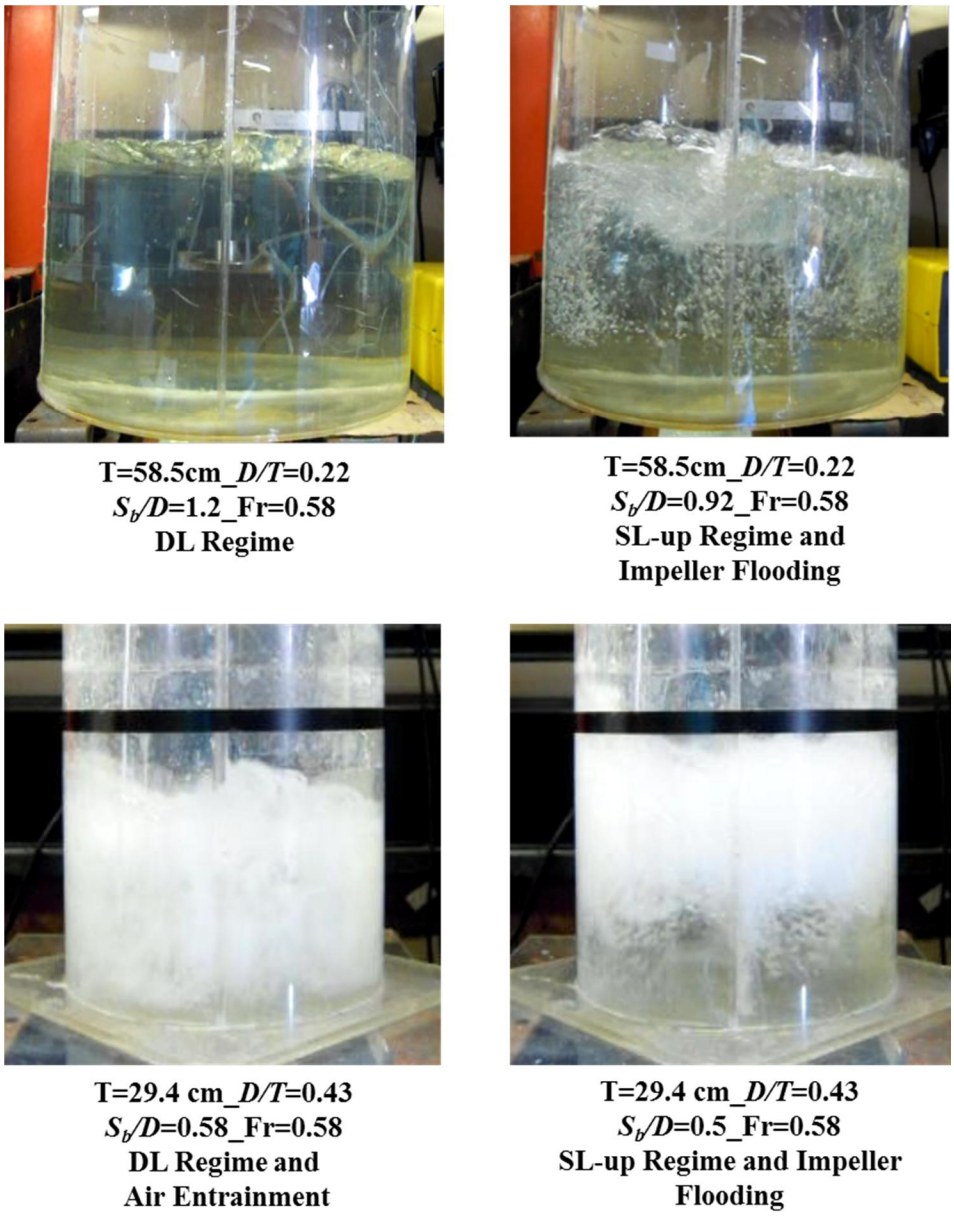

Figure 5.14 Figures on left show the surface air entrainment without flow regime changing (DL Regime) and figures on the right show impeller flooding for low S_b/D liquid system.

5.5 Vortex Formation, Froude Number and Impeller Flooding Regime

The experimental observation described in the previous section have clearly shown that the air-liquid interface does not remain flat when the S_b/D ratio is below the critical level and the agitation speed is sufficiently high. As the agitation speed is increased a vortex begins to form near the shaft, and its depth increases with the intensity of the agitation speed. Impeller flooding can be observed when this vortex depth reached the impeller.

In this section, vortex depth (the lowest point in the vortex center with respect of the initial level of the liquid at rest) and vortex height (the highest point near the vessel wall with respect of the initial level of the liquid at rest) were obtained as a function of Froude number. In previous work available from the literature, vortex depth in stirred tanks in unbaffled tanks was modeled by applying the Navier-Stokes equation to the system under investigation (Smit et al. 1991). Such modeling was based on the following assumptions:

i. A low-viscosity liquid is used and the viscosity term in the Navier-Stokes equation can be ignored;
ii. The flow is only in the tangential direction, i.e., the axial and radial velocities are small enough to be ignored.

Nagata (1975) divided the rotating fluid vortex into two zones: (1) an inner core region where a forced vortex exist (in which the liquid rotates as a solid body) and where it is assumed that the liquid angular velocity is equal to that of the impeller; (2) an outer region where a free vortex exists. In that region momentum is transferred only in radial direction. Based on these assumptions, Smit et al. 1991 reported two equations for dimensionless vortex depth, h_1^* and vortex height, h_2^* as linear functions of Froude number.

The vortex depth is the only important variable in this work since when such depth is equal to the impeller submergence flooding occurs. The following expression was obtained by Smit el al. (1991) for the vortex depth:

$$h_1^* = \left[\pi^2 \times \Omega^{*2} \times \left(\xi_c^{\,2} - \frac{\xi_c^{\,4}}{\xi_T^{\,2}} \right) \times \left(\frac{3}{4} - \ln\left(\frac{\xi_c}{\xi_T} \right) \right) \right] \times Fr = k_1 \times Fr \tag{6.1}$$

where:

$$h^*_{\,1} = \frac{H - Z_0}{D} = \frac{S_d}{D} \tag{6.2}$$

$$(Froude \text{ Number}) \; Fr = \frac{N^2 D}{g} \tag{6.3}$$

$$\Omega^* = \frac{\Omega}{2\pi N} = \frac{2\pi N}{2\pi N} = 1 \tag{6.4}$$

$$\xi = \frac{2r}{D}: \; \xi_C = \frac{2r_C}{D}; \; \xi_T = \frac{2r_T}{D} = \frac{T}{D} \tag{6.5}$$

where H is the static liquid level, Z_0 is the vortex depth, r_C is the radius at which the forced vortex is transferred into the free vortex and r_T is the radius of the vessel (Smit et al., 1991).

The constant k_1 in these equations depends on the geometry of the system and r_C which can be varied by changing the D/T ratio. In this work, C was related to D/T assuming a power law dependence of the type:

$$h^*_{\,1} = \frac{S_d}{D} = k_1 \, Fr_{flooding} = \alpha \left(\frac{D}{T} \right)^{\beta} Fr_{flooding} \tag{6.4}$$

The values of the constants α and β were obtained by substituting for h_1* the impeller submergence S_d (defined as the distance between the static liquid level and impeller disk) and by using for N in the Froude number the experimentally obtained

agitation speed needed to achieve impeller flooding. The experimental data were used to obtain the values of α and β by regression. A summary of the input data is given in Table 5.3. The experimental values that were included in the regression were those obtained when: (1) the system was operating in the SL-up Regime and; (2) the vortex depth reached the impeller disk. Smit et al. (1991) obtained a value of k_1=2.2 using two unbaffled vessels with constant D/T ratios and different agitation speed.

Table 5.3 Experimentally Obtained Input Data for the Determination of Parameters in the Vortex Depth Equation

D/T	S_d[a] m	$h^*_1=S_d/D$	$Fr_{flooding}$[b]	$k_1=h^*_1/Fr$
0.22	0.105	0.828	0.415	1.993
0.26	0.038	0.596	0.289	2.063
0.31	0.038	0.496	0.195	2.543
0.42	0.038	0.370	0.122	3.032
0.43	0.042	0.331	0.104	3.189

[a] S_d is the distance between the static liquid level and the impeller disk
[b] This is the Froude number at which impeller flooding started (based on the agitation speed that produced the vortex depth equals to S_d when SL-up Regime produced for each D/T ratio)

Table 5.3 also reports the value of k_1 obtained using the experimental data in this work. The C's obtained here are of the same order of magnitude of the 2.2 value obtained by Smit et al. (1991). Regressing the data resulted in the following equation for the vortex depth in baffled systems at low S_b/D values (R^2=0.9711):

$$\frac{S_d}{D} = k_1 Fr_{flooding} = k_1 \frac{N_{flooding}^2 D}{g} = 5.711\left(\frac{D}{T}\right)^{0.7107} Fr_{flooding} \quad (6.5)$$

Figure 5.15 shows a comparison between experimental data and the fitted curve for Equation 6.5. Rearranging this equation resulted in the following equation:

$$Fr_{flooding} = \frac{N_{flooding}^2 D}{g} = 0.175\left(\frac{T}{D}\right)^{0.7107} \frac{S_d}{D} \quad (6.6)$$

This equation can be used to predict the agitation speed that results in impeller flooding from surface air entrainment when $S_b/D < S_{bc}/D$ and the system is in the SL-up Regime.

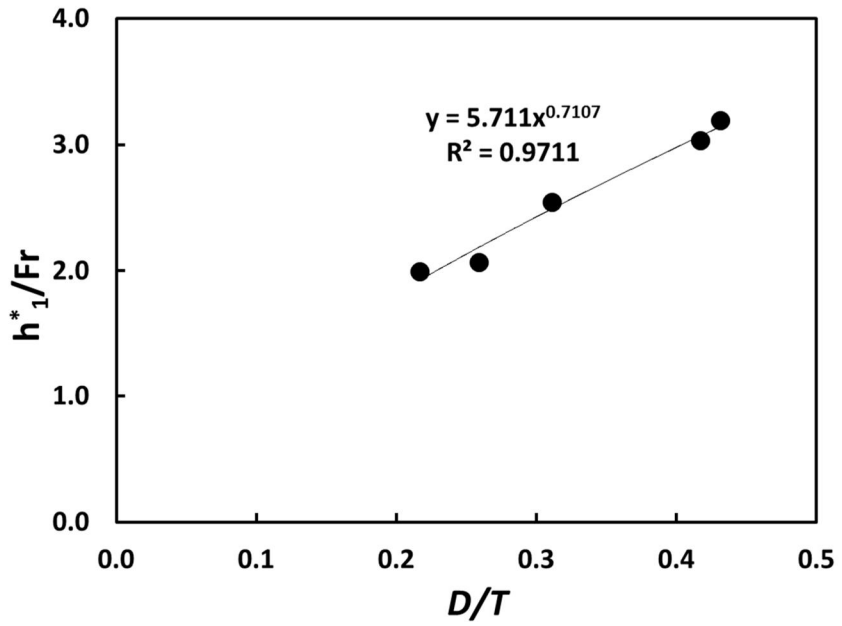

Figure 5.15 Figures on left show the surface air entrainment without flow regime changing (DL Regime).

5.6 Conclusion II

i. Depending on the values of S_b/D and C_b/T the following different regimes can be observed for a disc turbine rotating in a baffled stirred tanks:
    a. Double Loop (DL) Regime
    b. Single Loop-downpumping (SL-dp) Regime
    c. Single Loop-uppumping (SL-up) Regime
    d. No Circulation (NC) Regime

ii. For a given C_b/T ratio and D/T ratio a critical impeller submergence S_{bc}/D value exists where the fluid undergoes a transition from its initial flow Regime (DL Regime or SL-dp Regime) to the SL-up Regime, or for very low vales of C_b/T, to the NC Regime

iii. The SL-up Regime typically occurs well before the liquid level drops to the impeller level

iv. The critical impeller submergence S_{bc}/D value is higher (and hence the operating window in which the system can be operated without entering the SL-up Regime is wider) when:
    a. the impeller off-bottom clearances (C_b/T) is lower;
    b. the D/T ratio is larger

v. The NC Regime, only achievable for very low impeller off-bottom clearances ($C_b/T \leq 0.05$) and low S_b/D ratios, results in no clear recirculation and very poor mixing conditions

vi. Surface air entrainment and impeller flooding can only be achieved if the following conditions are both met:

a. S_b/D is low enough to produce SL-up Regime; and

b. the agitation speed N is high enough to result in a Froude number sufficiently large to create a vortex reaching the impeller

vii. Three types of transitions in flow regime were observed as the S_b/D was lowered:

a. DL Regime to SL-up Regime

b. SL-dp Regime to SL-up Regime

c. SL-dp Regime to NC Regime

viii. These flow transitions are associated with a sudden drop in Power Number, Po and the possibility of surface air entrainment if the agitation speed is appropriately high, thus resulting in even lower Po values

ix. An equation was obtained to determine the agitation speed at which impeller flooding from surface air entrainment occurs when the impeller is in the SL-up Regime.

CHAPTER 6

RESULTS AND DISCUSSION III – MIXING PERFORMANCE IN PARTIALLY FILLED STIRRED VESSELS FOR SINGLE AND MULTIPHASE SYSTEMS

In Chapter 4 and Chapter 5 the effect of S_b/D on flow regimes, induced surface air entrainment, Power Number, and Pumping Number in stirred vessels with different geometrical variables (C_b/T, D/T) was described. In this chapter, the effect of S_b/D on the performance of the same mixing systems to achieve different mixing requirements, such as liquid blending and solid suspension, is reported, together with the effect of submergence on important variables, such as the velocity distributions in the bottom region of the vessel or near the air-liquid interface, which are known to directly impact mixing effectiveness.

6.1 Velocity Distribution and Turbulence Intensity near the Tank Bottom

A fundamental understanding of mixing operations cannot only rely on overall measurement of quantities such as power dissipation or Power Numbers, but often requires also the quantification of other variables of importance at the location of relevance for the process under investigation. For example, solid suspension in stirred liquids is a process that is strongly affected by the uplifting velocity of the solid particles near the tank bottom. Therefore, the determination of the velocity profiles near the tank bottom and the quantification of how they change when variables such as S_b/D and C_b/T are varied are essential in order to gain a fundamental understanding of the solid suspension effectiveness of a mixing vessel.

In this portion of the work, the velocity field and turbulence intensity in the lower portion of the tank bottom were studied. These properties of the flow field are important

especially as far as the attainment of the complete suspension of solids off the tank bottom is concerned. Suspension of solid particles is a complex phenomenon caused by strong turbulent disturbances near the tank bottom, which can lift the particles upwards, combined with a sufficiently high average velocity field "sweeping" the tank bottom and distributing the particles in other regions of the vessel (Baldi et al., 1978). Therefore, the vessel configurations and impeller types and geometries that generate stronger turbulence near the bottom of the vessel are typically capable of suspending solids at lower agitation speeds, often with lower overall energy consumption.

Figure 6.1 presents the PIV measurements and the VOF-CFD simulation results for the non-dimensional axial and radial velocities (U_r/U_{tip} and U_z/U_{tip}), as well as turbulence intensities (k/U_{tip}^2), on two different horizontal surfaces near the tank bottom (at Z/T=0.04 and Z/T=0.07) in a stirred vessel with D/T=0.31 and C_b/T=0.31 at N=300 rpm, corresponding to a tip speed velocity, U_{tip} of 1.2 m/s (Fr=0.2). This data were obtained for S_b/D=0.77, i.e., when the impeller submergence was sufficiently high, but barely so, to still observe a DL Regime (as shown Figure 2 in Chapter 4) and for S_b/D=0.59, i.e., when the system had transitioned to the SL-up Regime (as also shown Figure 2 in Chapter 4).

These graphs clearly show that the flow transition was accompanies by a significant reduction in velocity magnitude and the turbulence intensity as S_b/D decreases from 0.77 to 0.59. A summary of the average difference in velocity magnitude and turbulence intensity for these impeller submergence ratios is presented in Table 6.1. This table additionally shows data for two more plane locations where measurement were

made, i.e., Z/T=0.10 and 0.15. Negative signs imply the reduction of each property when S_b/D ratio was reduced from 0.77 to 0.59.

Phenomena such as solid suspension, which rely on the uplifting capability of the fluid near the vessel bottom, are likely to be affected by such significant changes in the flow field and the turbulence intensity.

The flow field changes that accompany another regime transition phenomenon were also studied here. As it was discussed in Chapter 5, for C_b/T=0.14 the flow pattern transitions from a "Single loop-downpumping" Regime (SL-dp Regime) to a "Single loop-uppumping" Regime (SL-up Regime) as the S_b/D ratio decreases from 0.77 to 0.60. The results for this case are plotted in Figure 6.2. This figure presents the non-dimensional axial velocities (U_r/U_{tip}), radial velocities (U_z/U_{tip}), and turbulence intensities (k/U_{tip}^2) on two horizontal surfaces near the tank bottom (at Z/T=0.04 and Z/T=0.07) in a stirred vessel with D/T=0.31 and C_b/T=0.14 at N=200 rpm, corresponding to a tip speed velocity, U_{tip} of 0.8 m/s (Fr=0.1). Each panel in this figure shows curves for three different impeller submergence ratios, i.e., one above the critical level (S_b/D=1.03) which produced a "single-loop down-pumping" recirculation flow; at the critical submergence, i.e., S_b/D=0.77 which again produced the same flow pattern; and below the critical submergence, i.e., at S_b/D=0.64 which produced a "single-loop down-pumping" recirculation flow (Figure 6.2). The selected agitation speed was lower compared to the previous case (C_b/T=0.3) to avoid any air entrainment and impeller flooding (Figure 5.5). Therefore, any reduction in velocities or turbulence intensity for this case is only due to flow pattern changes.

Table 6.1 Average Percentage Change in Radial Velocity, Axial Velocity and Turbulence Intensity when the Liquid Level Dropped from $S_b/D=0.77$ to $S_b/D=0.59$ and Flow Transition from the DL Regime to the SL-up Regime Occurred. Data are from PIV Measurement near the Tank Bottom, i.e., on Four Different Horizontal Surfaces (Different Z/T Values). $C_b/T=0.30$, $D/T=0.31$ and N=300 rpm

	Average percentage change in $\mathbf{U_r/U_{tip}}$	Average percentage change in $\mathbf{U_z/U_{tip}}$	Average percentage change in $\mathbf{k/U_{tip}^2}$
Z/T=0.04	-70%	-47%	-53%
Z/T=0.07	-63%	-63%	-47%
Z/T=0.10	-55%	-68%	-36%
Z/T=0.15	-40%	-22%	-44%

These graphs clearly show for $S_b/D=1.03$ and 0.77 the PIV measurements generate very similar profiles, implying that relatively small changes in submergence that do not involve a regime transition have little impact on the flow near the tank bottom. However, when the regime transition took place the velocity profiles change dramatically. The radial velocities for $S_b/D=0.64$ are now directed inwards (negative U_r), a phenomenon that is consistent with the flow reversal associated with the SL-up Regime. The axial profiles also show that the flow reversal results in a significant reduction in the axial velocities and especially of the turbulence intensity, which is responsible for bursting effects capable of lifting up the particles before they become swept away by the prevailing flow.

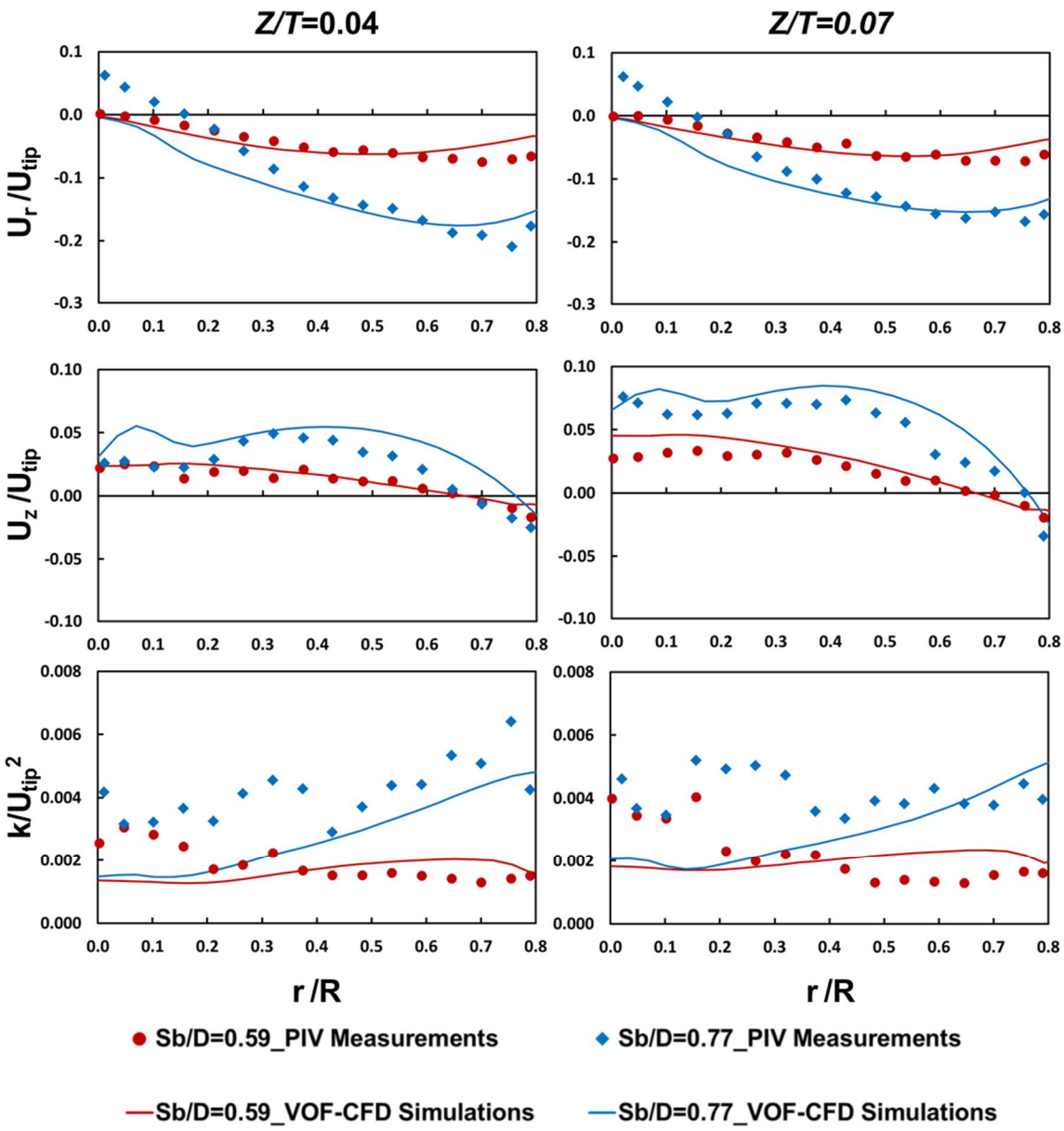

Figure 6.1 VOF-CFD simulations and PIV measurements of radial and axial velocities and turbulence intensities for S_b/D=0.77 and 0.59 on two different iso-surfaces near the tank bottom (C_b/T=0.30, D/T=0.31 and N=300 rpm).

A summary of the average reductions of velocity field and turbulence intensity is presented in Table 6.2, which additionally shows data for two more plane locations where measurement were made, i.e., Z/T=0.10 and 0.15. The overall reduction in the velocity field and turbulence intensity that can be observed as S_b/D decreased from 0.77 to 0.64 is

less than in the previous case when C_b/T was equal to 0.30. This could be explained by the partial impeller flooding effect that could have affected the flow generated for C_b/T=0.30. PIV measurements for C_b/T=0.3 (Figure 6.1and Table 6.1) were taken at Froude number equals to 0.2 which was the beginning of impeller flooding. However, experimental data for C_b/T=0.14 were taken at lower agitation speed (Fr <0.2), before entering to the flooding regime. Therefore, any reduction in the velocity field and turbulence intensity for this case is due to flow regime changes (SL-dp to SL-up).

As it was mentioned before, the sudden reduction shown in Table 6.1 and 6.2 in the flow field and turbulence intensity near that tank bottom are expected to have a strong impact on solid suspension, as discussed below.

Table 6.2 Average Percentage Change in Radial Velocity, Axial Velocity and Turbulence Intensity when the Liquid Level Dropped from S_b/D=0.77 to S_b/D=0.64 and Flow Transition from the SL-down Regime to the SL-up Regime Occurred. Data are from PIV Measurement near the Tank Bottom, i.e., on Four Different Horizontal Surfaces (Different Z/T Values). C_b/T=0.14, D/T=0.31 and N=200 rpm

	Average percentage change in $\mathbf{U_r/U_{tip}}$	Average percentage change in $\mathbf{U_z/U_{tip}}$	Average percentage change in $\mathbf{k/U_{tip}^2}$
Z/T=0.04	-5%	-58%	-29%
Z/T=0.07	+38%	-44%	-34%
Z/T=0.10	+16%	-41%	-37%
Z/T=0.15	-4%	-52%	-33%

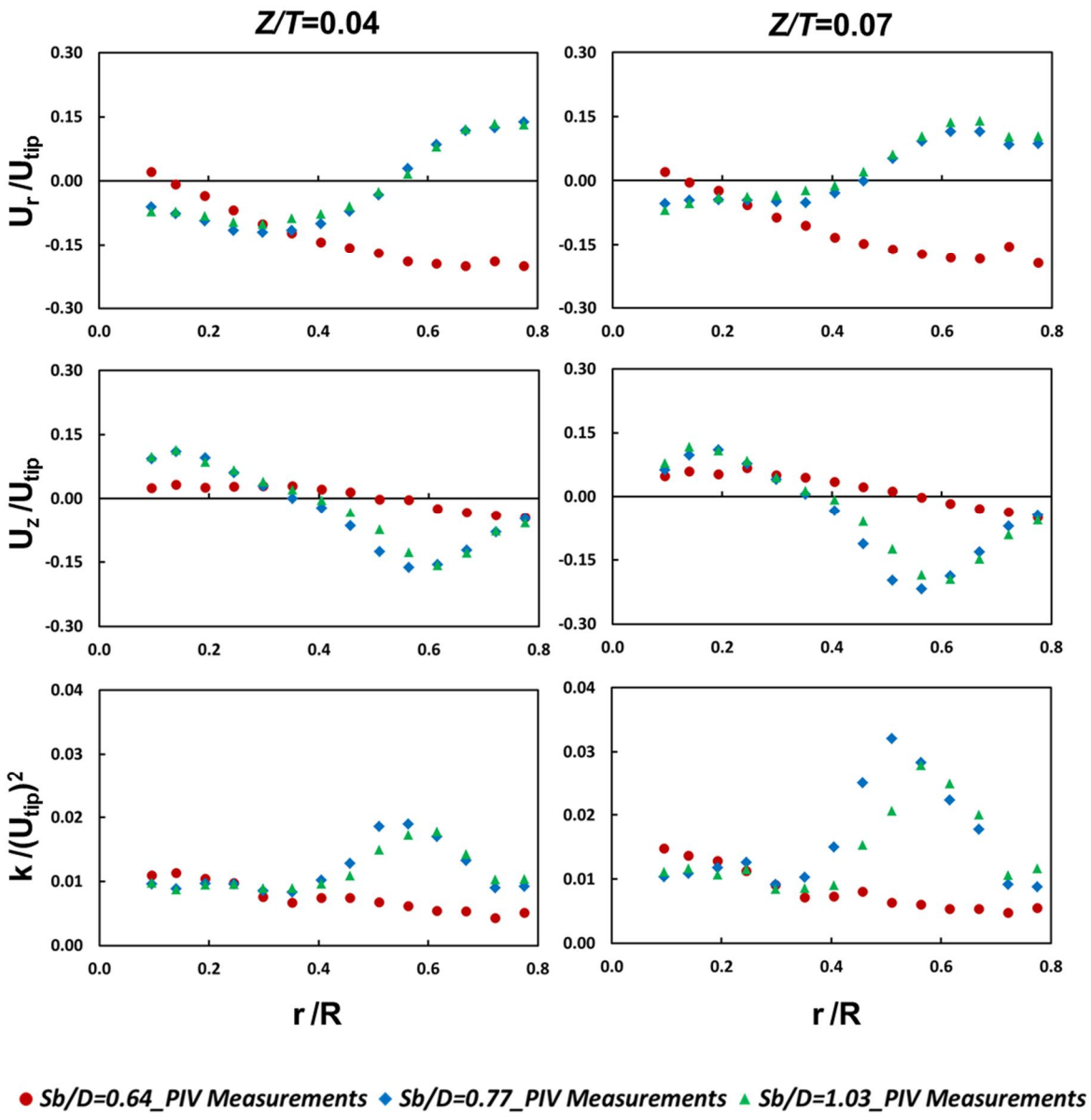

Figure 6.2 PIV measurements of radial and axial velocities and turbulence intensities for S_b/D=1.03, 0.77 and 0.59 on two different iso-surfaces near the tank bottom (C_b/T=0.14, D/T=0.31 and N=200 rpm).

6.2 Velocity Distribution and Turbulence Intensity near the Air-Liquid Interface

The velocity field and turbulence intensity near the air-liquid interface are important for surface air entrainment. N_E is defined as the minimum agitation speed which adds sufficient energy to the stirred tank to entrain bubbles into the vessel. As the impeller submergence decreases air entrainment occurs at progressively lower agitation speeds

(Bhattacharya et al., 2007; Malli et al., 2009). For instance, N_E for agitation system with D/T=0.31, C_b/T=0.30 and S_b/D =2.23, 0.77 and 0.59 were found to equal to 600, 450 and 300 rpm (the experimental method has been explained in Chapter 2 (Section 2.6)). Ervin et al. (1986) reported that air entrainment occurred when the turbulence intensity near the surface was large enough to overcome both surface tension and gravity effects. Bhattacharya et al. (2007) found that both velocity and turbulence intensity in axial direction near the air-liquid interface are the important factors for entrainment of the air bubbles.

In this work, the same mixing system described in the previous section was studied but with particular attention being paid to the velocities near the interface. Figure 6.3 presents the PIV measurements and the CFD simulation results for the non-dimensional axial velocities (U_r/U_{tip}), radial velocities (U_z/U_{tip}), and turbulence intensities (k/U_{tip}^2), on a horizontal surface near the air-liquid interface, i.e., at Z′/T=0.04 for a stirred vessel with D/T=0.30 and C_b/T=0.31 at N=300 rpm, corresponding to a tip speed velocity, U_{tip} of 1.2 m/s (Fr=0.2). Z' is defined here as the distance from the air-liquid interface, and it was equal to 1 cm when Z′/T=0.04 in this system (Z′ is zero at air-liquid interface). This figure contains the results of the FS-CFD simulations of dimensionless radial velocity, axial velocity and turbulence intensity for S_b/D equals to 2.23 (H/T=1) and 1.24 (H/T=0.69). In addition, this figure contains VOF-CFD simulation results for S_b/D equal to 0.77 (H/T=0.54) and 0.59 (H/T=0.49). This figure shows that the velocities and turbulence intensities near the surface are very close to each other when the impeller submergence is large (S_b/D≥0.77) and the DL Regime prevails. However, the velocities and turbulence intensities increased suddenly when the flow pattern changes (S_b/D=0.59;

SL-up Regime). Therefore, air-entertainment can be expected to occur at much lower agitation speeds in stirred vessels in which the recirculation flow is dominated by the SL-up Regime. This can explain why this regime can facilitate surface air entrainment and produce impeller flooding.

In Figure 6.4, the experimentally measured velocities and turbulence intensities on two planes close to the air-liquid interface (1 cm and 2 cm away from air-liquid interface corresponding to $Z'/T=0.04$ and $Z'/T=0.08$, respectively) are reported for different impeller submergence ratios when the impeller is relatively low in the tank ($C_b/T=0.14$) and the SL-down Regimes dominates. A trend similar to that observed for the $C_b/T=0.3$ case can be seen. The axial velocities, axial velocities, and turbulent intensity increased suddenly when the flow pattern transition from SL-dp Regime to SL-up Regime occurs as the S_b/D ratio decreases from 0.77 to 0.64. Therefore, air entrainment can be expected to happen at a lower agitation speed when the SL-up Regime dominates, as experimentally observed.

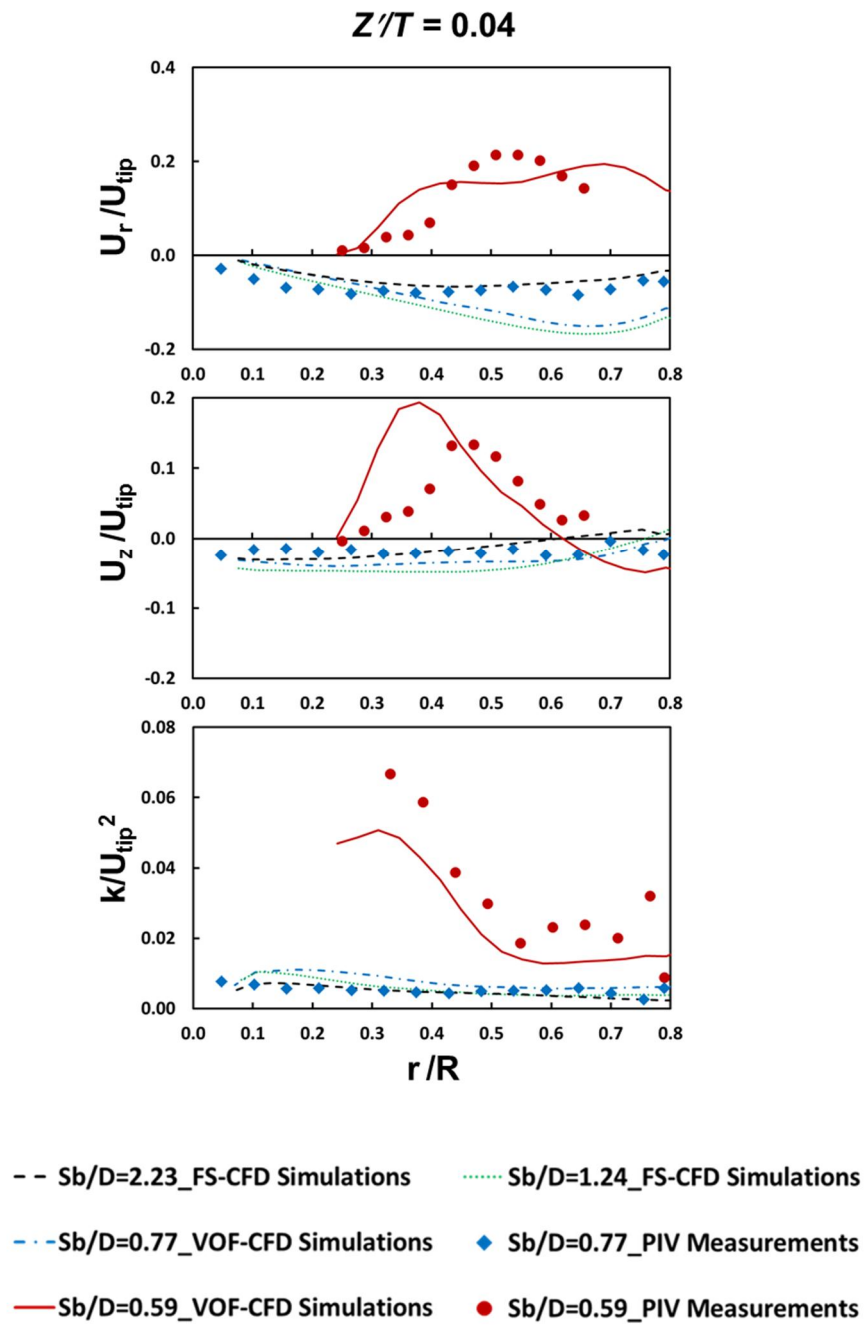

Figure 6.3 VOF-CFD simulations and PIV measurements of radial and axial velocities and turbulence intensities for different S_b/D, C_b/T=0.30, D/T=0.31 and N=300 rpm near the air-liquid interface (1 cm away from air-liquid interface).

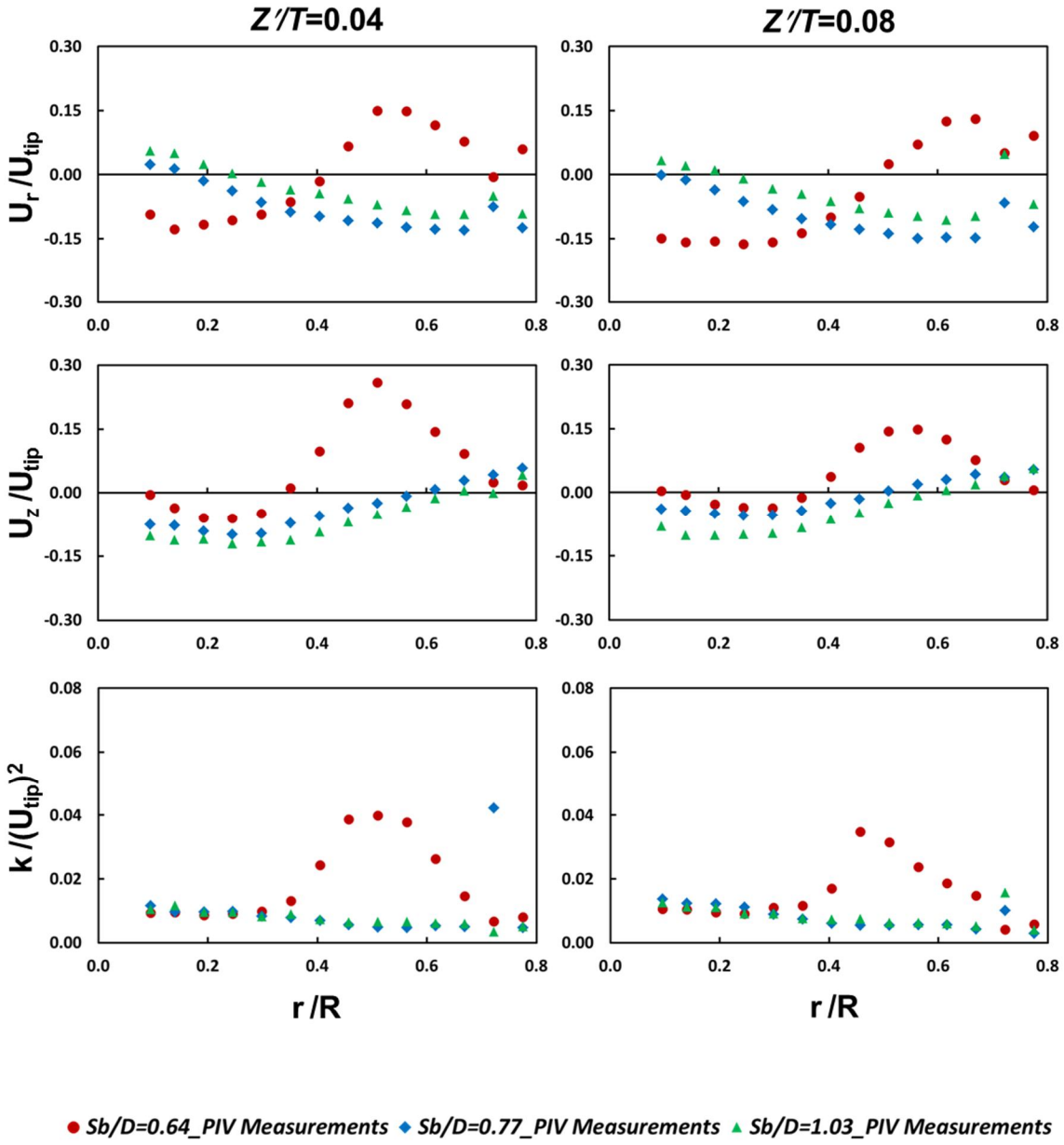

Figure 6.4 PIV measurements of radial velocities, axial velocities, and turbulence intensities for different S_b/D ratios near the air-liquid interface when C_b/T=0.14, D/T=0.31 and N=200 rpm.

6.3 Mixing Time (Blend Time) in Partially Filled Stirred Vessels

In this work, mixing time was measured experimentally using a colorimetric system coupled with image processing (as explained in Chapter 2) and was predicted using CFD simulations (as explained in Chapter 3) for a stirred vessel with D/T=0.31, C_b/T=0.30 and different filling ratios. Both experimental and computational results were compared with the predicted mixing time using correlations available from the literature.

6.3.1 Mixing Time for Standard Case (H/T=1 and C_b/T=0.30)

In this portion of the work, the color change throughout the stirred vessel resulting from the discoloration of phenolphthalein when HCl was added to a NaOH solution was captured on images that were recorded with a CCD camera. Each digital image was analyzed with the MATLAB Image Analysis Toolbox to determine the green light intensity for a number of pixels in the each image. As a result, the MATLAB output was the green light intensity, I, versus time. Then normalized light intensity, $\overline{I}$, was calculated as following:

$$\overline{I} = \frac{I(t) - I_{in}}{I_f - I_{in}} \tag{6.1}$$

where I_{in} and I_f are the initial and final green light intensity, respectively.

A typical graph of the normalized light intensity as a function of time for a conventional stirred vessels (H=T and C_b/T=0.3; N=200 rpm) at a specific location in the tank (Point 2-4 on the 0° vertical plane in Figure 3.6 in Chapter 3) is presented in Figure 6.5. As anticipated, these experimental results show that the tracer concentration at a given point in the vessel fluctuates with time. However, the amplitudes of the concentration fluctuations decreased over time, and eventually the local concentration

converged asymptotically toward the ultimate homogeneous concentration value corresponding to a uniform dispersion of the tracer in the entire system. The dotted line in this figure identifies the injection time, $t_{injection}$, and the dashed line the time at which time the normalized light intensity reached the 95% value of the normalized intensity and stayed within the interval 95%-105%. As a result, the 95% mixing time, t_{95}, for this specific experiment was determined to be 8.54 sec. The final mixing time in this work was reported as the average of t_{95} at several points in the mixing vessel (i.e., Points 1-1, 1-4, 2-4, 3-1 and 3-4 at 0° in Figure 3.6).

It should be remarked that there is no special value attached to the 95% homogeneity level. In fact, in general, the mixing time, t_U, is defined as the time required by the tracer–liquid system to reach a desired and predefined level of tracer concentration uniformity, U. It is common to choose a 95% uniformity level as the endpoint of the blending process (corresponding to a 95% blend time, t_{95}), although other uniformity levels such as t_{99} and $t_{99.9}$ (or any other value for that matter) can also be used. It is always possible to calculate the blend time to achieve a desired level of uniformity, U′, once the blend time at another uniformity level is known using the following equation:

$$\frac{t_{U'}}{t_U} = \frac{-\ln(1-U')}{-\ln(1-U)} \tag{6.2}$$

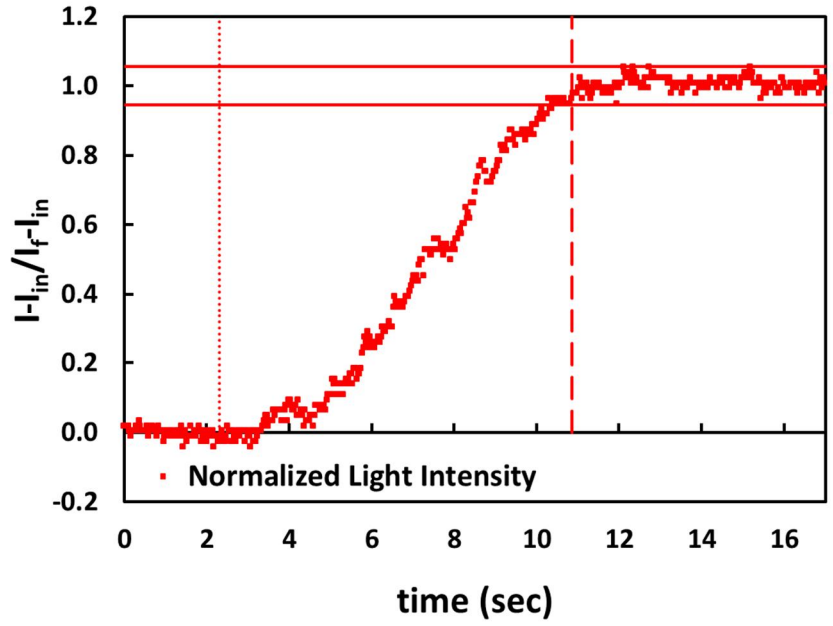

Figure 6.5 Plot of the experimental values of the normalized light intensity vs. time for a conventional stirred vessel (H=T and C_b/T=0.3, N=200 rpm) during a mixing time experiment. The dotted line corresponds to the injection time and the dashed line to the first time when the normalized light intensity reached the 95% value and remained within 95%-105% range.

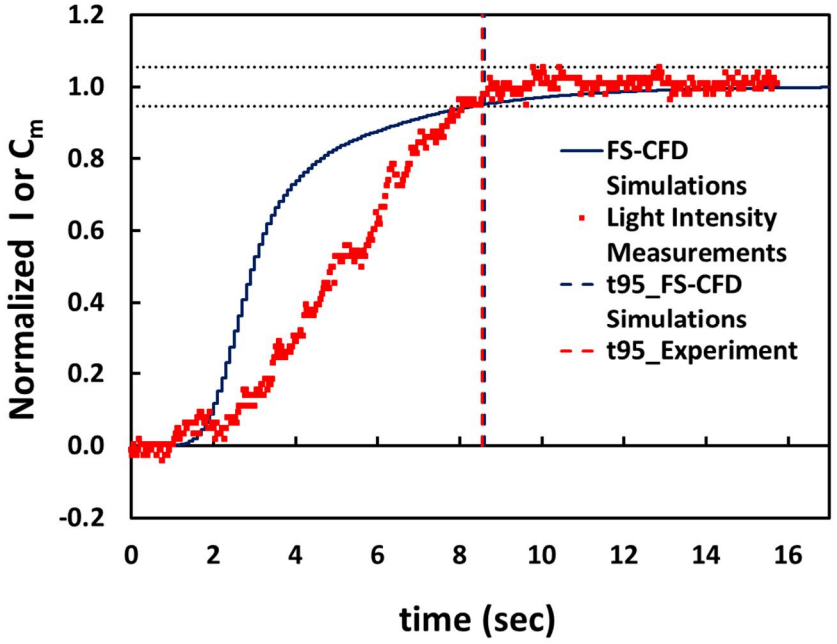

Figure 6.6 Plot of the experimental and predicted (though FS-CFD simulation) values of the normalized light intensity vs. time for a conventional stirred vessel (H=T and C_b/T=0.3, N=200 rpm) during a mixing time experiment. The dashed line corresponds to mixing time.

In this work, mixing time was also predicted with FS-CFD by tracking the tracer mass fraction vs. time at the same locations in the tank that were used to obtain the experimental mixing time. In this case, the normalized mass fraction, $\bar{C}_m$, was obtained using the same approach used in the experimental part:

$$\bar{C}_m = \frac{C_m(t) - C_{in}}{C_f - C_{in}} = \frac{C_m(t)}{C_f} \tag{6.3}$$

where C_{in} and C_f are the initial and final tracer mass fraction at the selected point in the mixing vessel, respectively. Since the tracer was introduced at t=0, C_{in} is equal to zero at all location. Mixing time at each point was calculated as the time at which time the normalized light intensity reached the 95% value of the normalized tracer mass fraction and stayed within the interval 95%-105%. The average of the mixing times calculated at the selected locations (Chapter 3, Figure 3.6) was reported as the overall mixing time.

Figure 6.6 reports both the experimental and computational results for the normalized light intensity and for tracer mass fraction as a function of time. The experimental data in this figure are those that were initially presented in Figure 6.5, but the injection time for the experimental data was shifted to t=0. In this example, one can see that the predicted mixing time from the FS-CFD simulation and experimental mixing time are in a good agreement: t_{95}= 8.66 s using the computational method vs. t_{95}=8.54 s using the experimental method.

Table 6.3 summarized the overall mixing time, t_{95}, experimentally measured and CFD-predicted in this work at three different agitation speeds (100 rpm, 200 rpm, and 300 rpm) along with the dimensionless global mixing time, $t_{95}N$, for the conventional stirred vessel. One can see that the agreement is quite satisfactory.

In addition to the computation predictions, in this work an attempt was made to correlate mixing time with another characteristic time of the agitation system, i.e., the "batch recirculation time", t_{BR}. Here, t_{BR} is defined as the ratio between the liquid volume in the tank and the flow rate generated by the impeller, i.e.:

$$t_{BR} \equiv \frac{V}{Q} \tag{6.4}$$

t_{BR} is the time required by the impeller to "sweep" the entire liquid volume of the tank V based on its pumping capacity Q. It is intuitive to imagine that some type of relationship must exist between t_U and t_{BR}. The simplest possible relationship between these two variables is a linear one. Therefore, in this work it was assumed that:

$$t_U = \alpha_U t_{BR} = \alpha_U \frac{V}{Q} \tag{6.5a}$$

where the proportionality constant α_U depends on the desired level of homogeneity U. If U=95% then:

$$t_{95} = \alpha_{95} t_{BR} = \alpha_{95} \frac{V}{Q} \tag{6.5b}$$

In this equation, Q can be obtained knowing the impeller Pumping Number (which can be predicted from the CFD simulation results), since $Q=N_Q \cdot ND^3$. A regression of t_{95} vs. t_{BR} was conducted here for the case in which H/T=1, and different agitation speed. The value of α_{95} was found to be equal to 0.88 (R^2 =0.998). The resulting values for t_{95} predicted using Equation 6.5b together with the non-dimensional mixing time ($t_{95}N$) are also presented in Table 6.6. A good agreement between the results so predicted and the experimental data was found.

In order to further validate these results, a comparison with the correlations for mixing time available from the literature was also made. Over the years, several approaches have been proposed to model mixing time based on the assumed dominance of individual transport mechanisms in the stirred vessels (Patwardhan and Joshi, 1999). As a result, there are different correlation equations in the literature for mixing time. However, most of them are for H/T=1. The objective here is to obtain the mixing times at different impeller submergence ratios (S_b/D) or fill ratios (H/T) and not just for the case in which H/T=1. Therefore, it is important to use correlations that account for impeller submergence (or maximum liquid level, H) effects.

Table 6.3 Comparison of the Mixing Times Experimentally and Computationally Obtained in this Work with Values of Correlations and CFD Predictions Available in Literature for Conventional Stirred Vessels

	Condition	$\mathbf{t_{95}}$ 100 rpm Re=10,000	$\mathbf{t_{95}}$ 200 rpm Re=20,000	$\mathbf{t_{95}}$ 300 rpm Re=30,000	$\mathbf{t_{95}N}$	**Δ(%)**[a]
Present work	Light Intensity Measurements	15.90	8.49	5.47	27.4	
Present work	FS-CFD Simulations	15.80	8.60	5.20	27.0	-1.4
Equation 6.5b	$t_{95}=\alpha_{95}V/Q$	17.32	8.66	5.77	28.8	5.3
Equation 6.6	Grenville Equation	16.92	8.46	5.64	28.2	2.97
Javed et al. (2005)	Sliding Mesh CFD Simulations/ Re=24,000				28.0	2.26

[a] Difference between present light intensity measurements and preset predictions, correlations and predictions available in literature

The Grenville equation is the most common correlation equation that has been used in the literature (Paul et al., 2004):

$$t_{95} = \frac{5.2}{Po^{1/3}N}\left(\frac{T}{D}\right)^{1.5}\left(\frac{H}{D}\right)^{0.5} \tag{6.6}$$

This equation contains the liquid level term and also the Power Number Po, which are relevant for lower fill ratios. This equation was also used here to predict mixing time.

As expected, the mixing times obtained here and presented in Table 6.3 were inversely proportional to agitation speed. As a consequence, the non-dimensional mixing times $t_{95}N$ was constant. This table also presents a comparison between the results obtained here and $t_{95}N$ was obtained using the Grenville Equation and those obtained by Javet et al. (2005) using Sliding Mesh (SM) CFD simulations.

6.3.2 Effect of Impeller Submergence Ratio, S_b/D, on Mixing Time in Conventional Stirred Vessels

Mixing time, t_{95}, was experimentally measured and computationally predicted for different impeller submergence ratios, i.e. for S_b/D equal to 2.23 (H/T=1), 1.76 (H/T=0.85), 1.24 (H/T=0.69), 0.98 (H/T=0.61), 0.77 (H/T=0.54), and 0.59 (H/T=0.49). The results are shown in Figure 6.7. Mixing times for all of the impeller submergence ratios decreased inversely with agitation speed, as expected. Furthermore, the experimental results and the simulation predictions were in a good agreement in all cases including when the system transitioned to the SL-up Regime (S_b/D=0.59). However, for this case the largest difference between the mixing time experimentally obtained and that predicted based on FS-CFD simulations was observed (deviation of 15 % and 8% for N= 200 rpm and 300 rpm, respectively). In order to improve the prediction for this case,

VOF-CFD simulations for the agitation speed equals to 200 and 300 rpm were conducted. These results have been also included in Figure 6.7. This approach did not produce any significantly improved predictions compared to the experiments.

In order to understand better the impact of impeller submergence on mixing time, the experimental mixing times for all impeller submergence ratios are presented in Figure 6.8. This figure shows that mixing time decreased with impeller submergence when S_b/D was equal to 2.23, 1.76, 1.24 and 0.77, i.e., when the DL Regime was present. This phenomenon can be explained if one considers that the circulation time decreases as a result of the decreasing liquid volume when the impeller submergence decreases at constant C_b/T. In other terms, decreasing the impeller submergence as a result of decreasing the liquid level will lead to decreasing the amount of liquid volume (V) and hence mixing time, since the velocity field around the impeller did not change, as shown in Figure 4.7 (Chapter 4). However, Figure 6.8 also shows that t_{95} increased suddenly when the S_b/D was lowered to 0.59. This impeller submergence ratio led to a new flow pattern (SL-up Regime) and both the Power Number and the Pumping Number decreased suddenly compared to when the impeller had higher S_b/D ratios. These could be the reasons why mixing time was increasing for this submergence ratio instead of decreasing.

The dimensionless mixing times, $t_{95}N$, based on experimental data was then calculated and plotted as a function of the agitation speed, N (rpm), for different impeller submergence ratios. The results are presented in Figure 6.9. This figure shows that $t_{95}N$ was independent of agitation speed for any given S_b/D ratio provided that the impeller submergence was such as to generate the DL Regime (Figure 6.9a). This result was expected and is consistent with the data shown in Table 6.1 for conventional stirred

vessels with H/T=1 since in all cases the flow regime did not change. The average $t_{95}N$ value for three different agitation speeds was equal to as 27.38, 24.46, 21.67 and 16.05 for S_b/D values equal to 2.23 (H/T=1), 1.76 (H/T=0.85), 1.24 (H/T=0.69) and 0.77 (H/T=0.54), respectively. The dependence between $t_{95}N$ and H/T is approximately linear, especially for high H/T values, which is consistent with the observation that mixing time is proportional to the fill ratio.

The mixing time reduction resulting from a decrease in the impeller submergence ratio can additionally be explained using the predictions based on the batch recirculation time t_{BR} proposed here (Equation 6.5b), where the expressions for the varying liquid volume and the pumping rate (expressed as a function of the Pumping Number) are used:

$$t_{95} = \alpha_{95}\frac{V}{Q} = \alpha_{95}\frac{\frac{\pi T^2}{4}\left(C_b + S_b\right)}{N_Q N D^3} = \frac{\alpha_{95}\pi}{4N_Q N}\left(\frac{T}{D}\right)^2\left(\frac{T}{D}\frac{C_b}{T} + \frac{S_b}{D}\right) \tag{6.7}$$

$$t_{95}N = \frac{\alpha_{95}\pi}{4N_Q}\left(\frac{T}{D}\right)^2\left(\frac{T}{D}\frac{C_b}{T} + \frac{S_b}{D}\right) = \frac{\alpha_{95}\pi}{4N_Q}\left(\frac{T}{D}\right)^3\frac{C_b}{T} + \frac{\alpha_{95}\pi}{4N_Q}\left(\frac{T}{D}\right)^2\frac{S_b}{D} \tag{6.8}$$

This equation implies that if T/D and C_b/T are constant and if S_b/D is larger or equal to 0.77 (i.e., before flow pattern transition occurs) N_Q can be expected to be constant as well (as shown for N_{Qr} in Figure 4.4), and the non-dimensional mixing time becomes only a function of S_b/D. Therefore, under these assumptions the non-dimensional mixing time can be expected to be a linear function of the impeller submergence ratio only, which is similar to the trend that was found in the experimental results.

Figure 6.9 also shows that when the flow regime switched to the SL-up Regime as S_b/D was decreased to 0.59 $t_{95}N$ was no longer independent of N but increased with

agitation speed (Figure 6.9b). As shown above already, increasing the agitation speed when the system is operating in the SL-up mode can result in surface aeration and ultimately in impeller flooding. This observation is consistent with the increase in mixing time with N for such a case, since one can expect that as N is increased the impeller progressively loses its ability to be an effective pumper as a result of air entrainment and partial flooding. Therefore, one can expect that the mixing time would increase as a result.

In Figure 6.10, the experimental and computationally predicted of non-dimensional mixing times were plotted as a function of S_b/D at constant agitation speed. Clearly, $t_{95}N$ decreased with the impeller submergence ratio at any agitation speed until $S_b/D=0.77$, i.e., as long as the system was operated in the DL Regime, but suddenly increased when the regime transitioned to the SL-up Regime for $S_b/D=0.59$.

For comparison purposes, the predicted values for $t_{95}N$ based on Equation 6.8 ($t_{95}=\alpha_{95}t_{BR}$ where $\alpha_{95}=0.88$, as determined in the previous section) and Equation 6.6 (Grenville Equation) were also included in Figure 6.10. Both equations are appropriate for fully filled vessels ($S_b/D=2.23$ or $H/T=1$). For other impeller submergence ratios however, the Grenville Equation overestimates the dimensionless mixing time and failed to predict the sudden increase in mixing time when S_b/D was lowered from 0.77 to 0.59 and the regime transition to SL-up took place. Conversely, Equation 6.8 was still able to predict the whole phenomenon appropriately, since this equation contains the Pumping Number N_Q which can be correctly determined even when the flow regime changes to SL-up (average error=-1.1%). The agreement of experimental results with the predictions based on Equation 6.8 confirm that mixing time is indeed proportional to the

batch recirculation time, and that this proportionality remains even when the flow regime changes.

Therefore, both the prediction based on CFD simulations, and Equation 6.8 can be used to predict the mixing time for partially filled stirred vessels when experimental measurements are not available.

For better visualization purpose, Figure 6.11 shows the experimental and predicted (Equation 6.7 and Equation 6.8) results for both mixing time (t_{95}) and non-dimensional mixing time ($t_{95}N$). Above the critical impeller submergence ratio, S_b/D (DL Regime) t_{95} and $t_{95}N$ decrease linearly with decreasing impeller submergence ratio for all agitation speeds. Regressing the data resulted in the following equations:

$$t_{95}N = 7.49\left(\frac{S_b}{D}\right)+11.17 \tag{6.9}$$

$$t_{95}N = 8.90\left(\frac{S_b}{D}\right)+8.66 \tag{6.10}$$

Equation 6.9 (R^2=0.94) and Equation 6.10 (R^2=0.99) are the results from data regression of experimental data and proposed method in this work (Equation 6.8), respectively. As Figure 6.11 shows, the sudden increase in mixing time below the critical impeller submergence ratio, S_b/D (SL-up Regime) was correctly predicted using the method proposed in this work (t_{BR}).

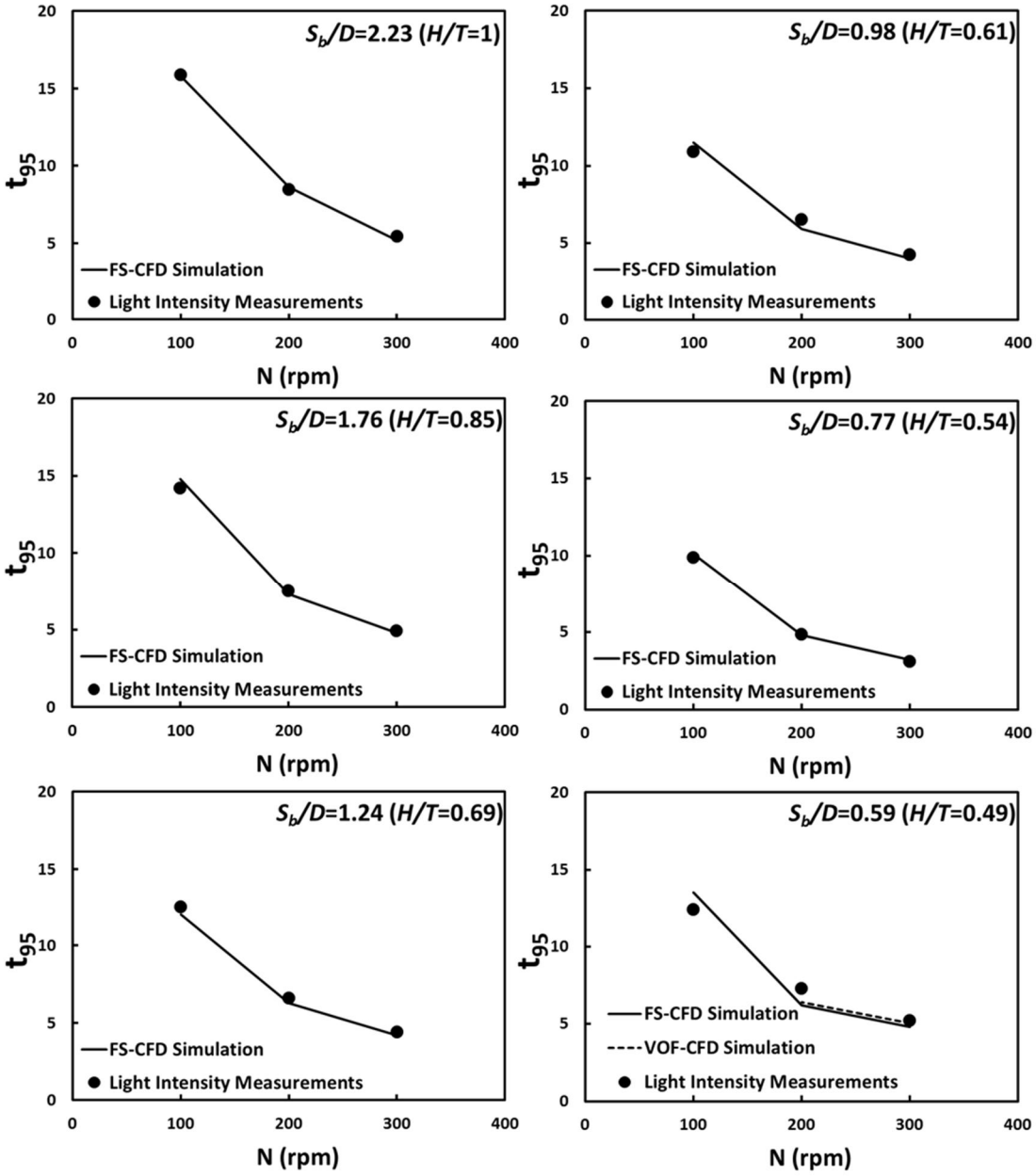

Figure 6.7 Experimental results and CFD simulation results for mixing time as a function of agitation speed for C_b/T=0.30, D/T=0.31, at different S_b/D ratios.

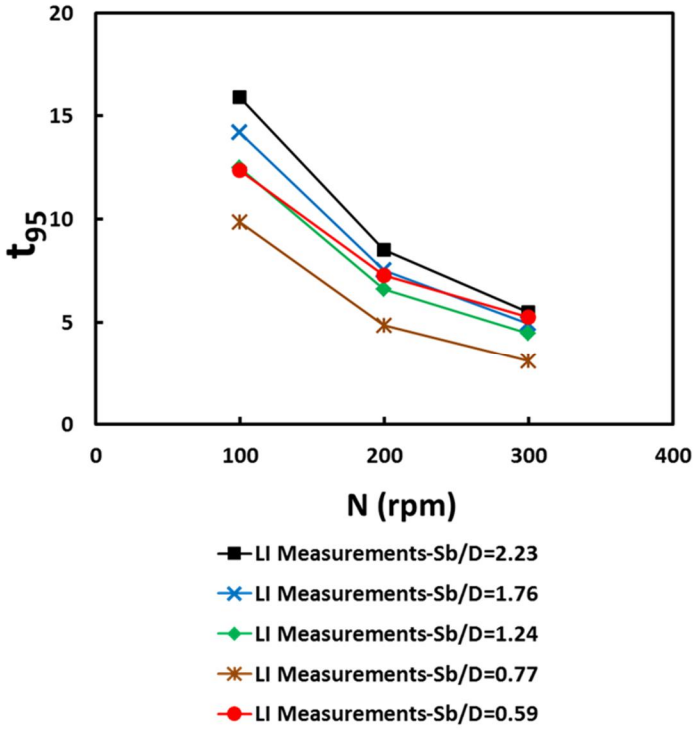

Figure 6.8 Summary of Experimental results and CFD simulation results for mixing time as a function of agitation speed for C_b/T=0.30, D/T=0.31, at different S_b/D ratios.

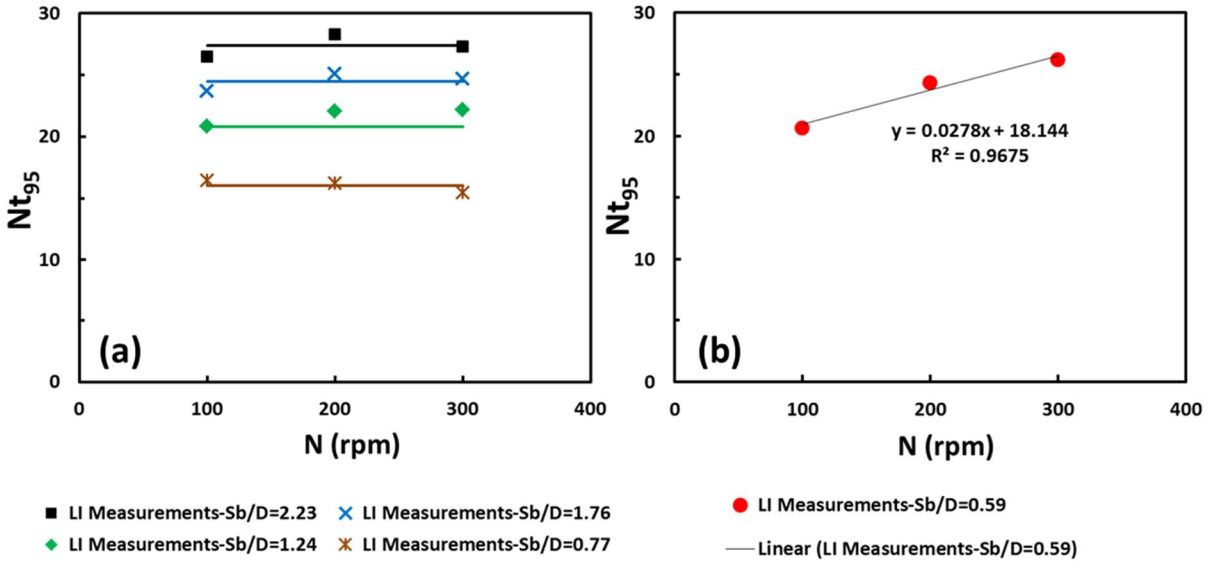

Figure 6.9 Experimental non-dimensional mixing time as a function of agitation speed for C_b/T=0.30, D/T=0.31: (a) S_b/D= 2.23, 1.76, 1.24 and 0.77 (DL Regime); (b) S_b/D=0.59 (SL-up Regime).

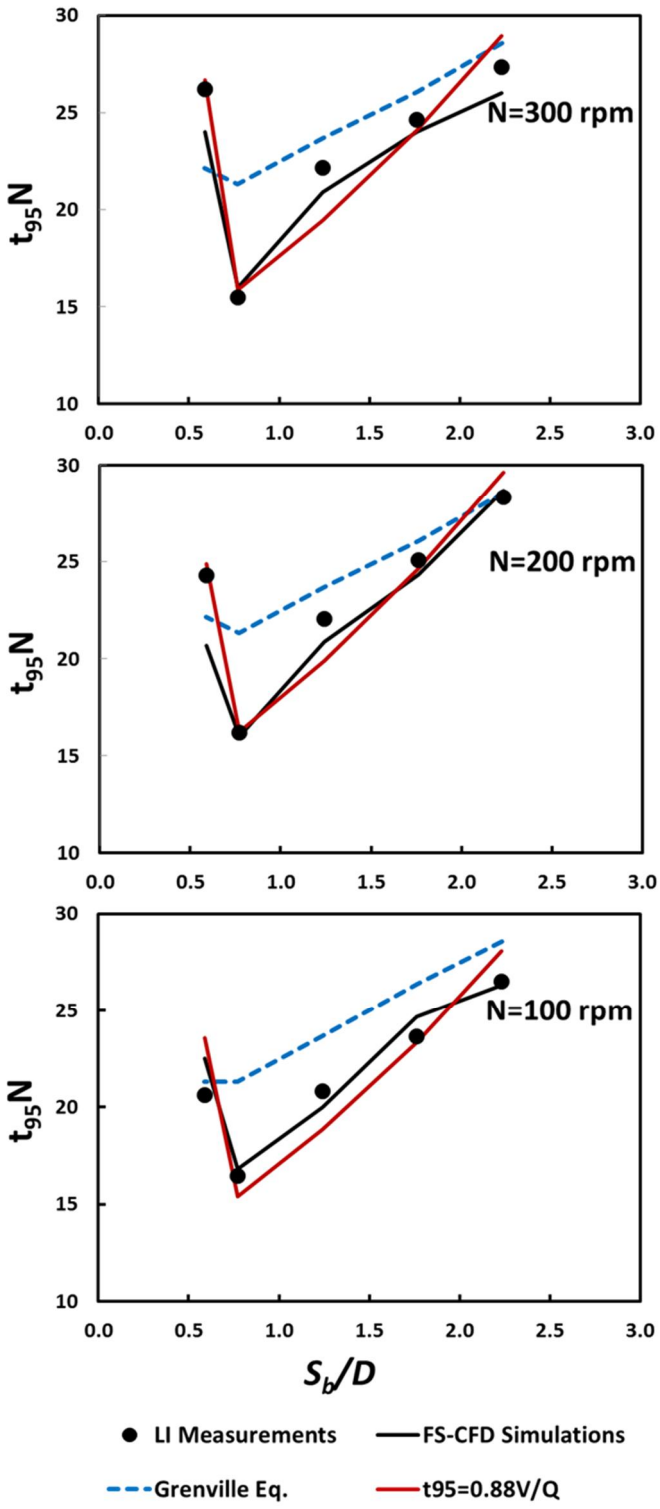

Figure 6.10 Non-dimensional mixing time as a function of the impeller submergence ratio for $C_b/T=0.30$, $D/T=0.31$, at different agitation speeds (Batch characteristic time: BCT).

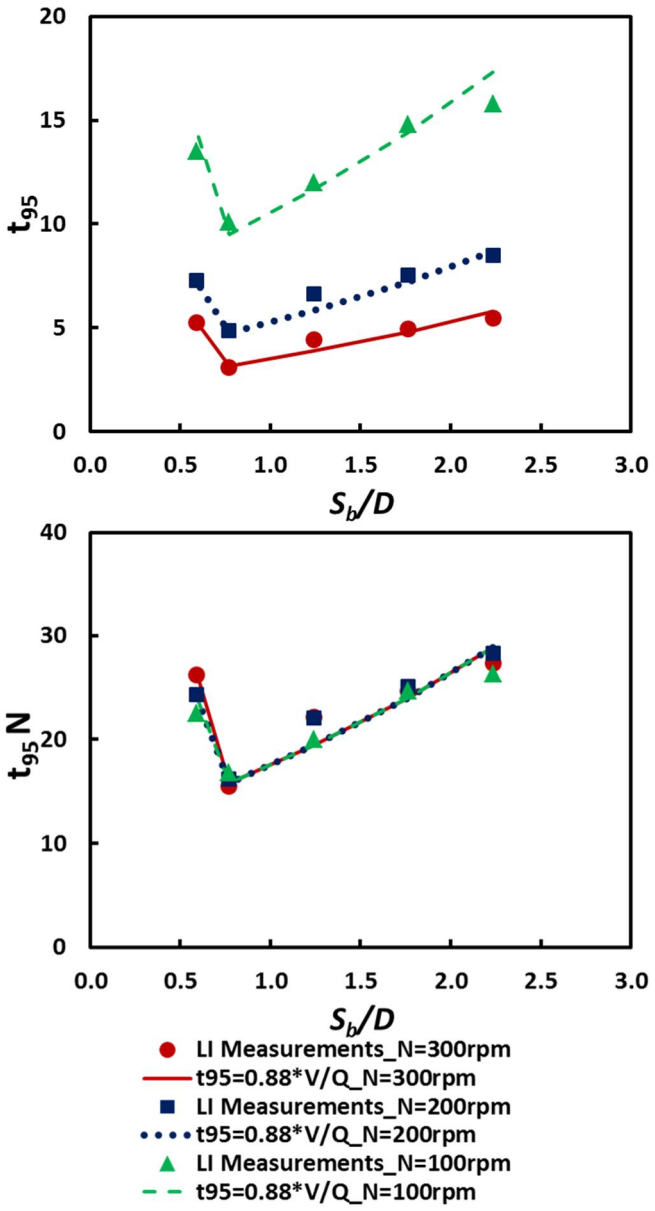

Figure 6.11 Comparison between the predictions based on the proposed method ($t_{95}=\alpha_{95}t_{BR}$, where $\alpha_{95}=0.88$) and the experimental data for mixing time (t_{95}) and non-dimensional mixing time ($t_{95}N$) as a function of the impeller submergence ratio for $C_b/T=0.30$, $D/T=0.31$, at different agitation speeds.

It is important to mention that the values for N_Q that appear in Equation 6.7 and Equation 6.8 were determined from FS-CFD simulations at low agitation speeds (N=100 rpm and 200 rpm) for both $S_b/D\geq0.77$ and $S_b/D=0.59$, i.e., before impeller flooding

occurred. In addition, VOF-CFD simulation results were used for $S_b/D=0.59$ at N=300 rpm ($N_Q=0.41$). The N_Q values for high submergence ratios ($S_b/D\geq0.77$) were nearly constant regardless of the agitation speed ($N_Q=0.77$-0.80). However, for $S_b/D=0.59$ and agitation speeds equal to 100 rpm and 200 rpm, N_Q was predicted to be equal to 0.45, and this drop in Pumping Number produced the increase in the predicted mixing time (based on t_{BR}) shown in Figure 6.11. It should be stressed that α_{95} was always kept constant at 0.88 in these calculations, based on the results obtained for the standard case (H/T=1)

6.4 Solid Suspension in Partially Filled Stirred Vessels

Experiments wer carried out in the same stirred vessel described in Figure 2.1. The liquid phase was water and spherical glass beads (0.5% wt/wt; $\rho_L=2500$ m^3/kg) with average diameter of 150 μm were used. The minimum agitation speed required for complete off-bottom particle suspension, N_{js}, was determined visually (as described in Chapter 2).

The main objective here was to characterize the effect of impeller submergence ratio (S_b/D) on N_{js} for stirred vessels with different C_b/T and D/T. N_{js} was obtained for: (1) D/T=0.31 and different C_b/T and S_b/D ratios; (2) and $C_b/T=0.30$ and different D/T and S_b/D ratios.

6.4.1 Effect of S_b/D on Minimum Agitation Speed for Complete Off-Bottom Solid Suspension for D/T=0.31 and Different C_b/T

Figure 6.12 presents a plot of N_{js} as a function of the submergence ratio (S_b/D) for D/T=0.31 and three different impeller off-bottom clearances (C_b/T) of 0.30, 0.14 and 0.05. The first observation from these results is that solid suspension occurs at lower agitation speed when the impeller is closer to the tank bottom. This could be seen by

comparing results for C_b/T= 0.30 and 0.14 and relatively high impeller submergence. This could be explained by different flow regimes that were seen by decreasing the C_b/T ratio from 0.30 (DL Regime) to 0.14 (SL-dp Regime). Previous work showed that a "single loop-downpumping" flow circulation produces stronger turbulence intensity near that tank bottom which is the important parameter for solid suspension. The predictions obtained using the correlations proposed by Armenante et al., (1998) were also included in this figure. The results obtained here are in agreement with those predictions for the case in which those correlations could be applied (H/T=1).

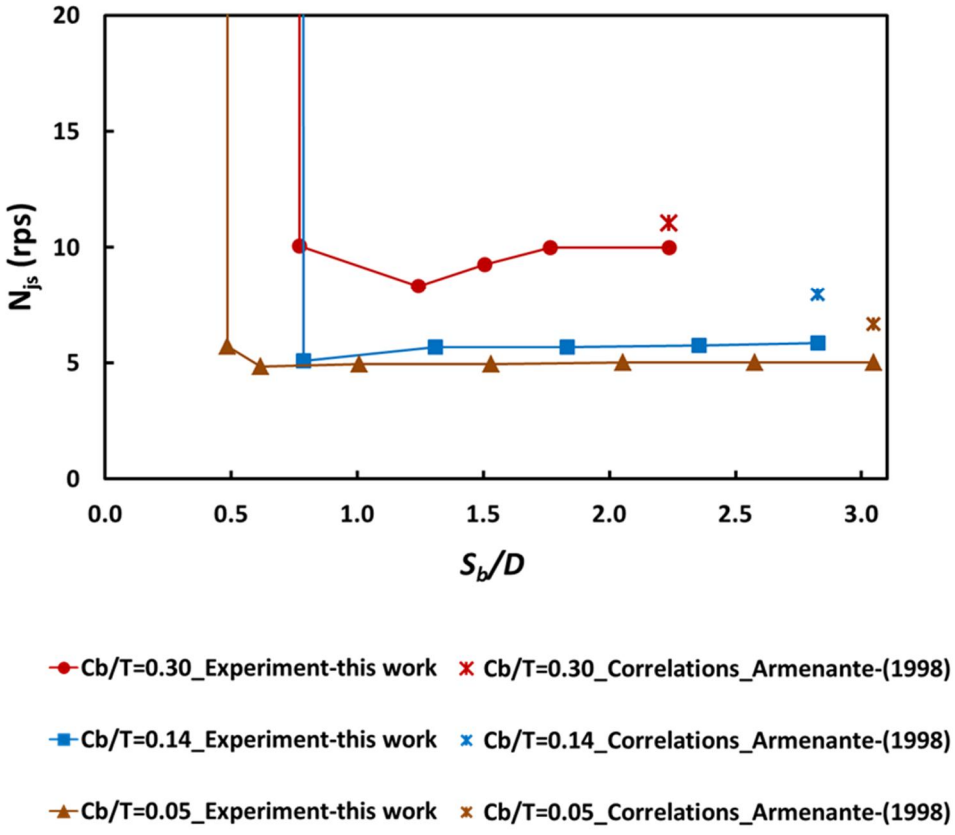

Figure 6.12 Minimum agitation speed for complete off-bottom solid suspension (N_{js}) as a function of impeller submergence ratio for D/T=0.31 and different C_b/T ratios.

The second and most important observation here is that for each impeller off-bottom clearances there is a minimum liquid level below which the solids cannot be suspended ($N_{js}=\infty$). When the impeller submergence ratio reaches a critical low value, solids can no longer be suspended even if the impeller speed is increased to a very high number. The critical S_b/D ratio for $C_b/T=0.30$ and 0.14 was 0.77 which is exactly the same submergence ratio corresponding to the flow pattern transition from either DL Regime to SL-up Regime for $C_b/T>0.16$ or from the SL-down Regime to SL-up Regime for $C_b/T<0.16$ as previously discussed in this work.

These results can be explained as follows. Whenever the flow regime transitions to the SL-up Regime as a result of a drop in the liquid level that lowers the S_b/D ratio below the critical level, two important phenomena occur that are critical to solid suspension: (1) the velocities and turbulence intensities in the lower portion of the vessel decrease, as described above (Figure 6.2 and Table 6.2). This would per se require a higher agitation speed to suspend the solids, assuming that everything else remains the same; (2) a segregated region forms above the impeller where a vortex can occur if the agitation speed is sufficiently high, thus possibly producing impeller flooding, as also described here (Chapter 4). However, if the agitation is increased in the attempt to achieve solid suspension (by trying to increase the velocities and turbulence intensities near the tank bottom) a vortex begins to form at the air-liquid interface which further reduces the pumping ability of the impeller. If the agitation is further increased, significant air entrainment occurs and the impeller becomes flooded, thus losing entirely its pumping effectiveness. At this stage, the solids can no longer be suspended no matter how high the agitation speed is.

A similar but even more dramatic phenomenon occurs when the impeller is placed very low in the tank ($C_b/T<0.05$). In this case, as soon as the impeller submergence drops below the critical S_b/D value for this case ($S_b/D=0.48$) the flow transitions from the SL-down Regime to the NC Regime and the impeller loses entirely its ability to pump. No solid suspension can occur at this point as also obtained experimentally and shown in Figure 6.12.

However, by decreasing the impeller off-bottom clearances (C_b/T) the operating window in which the impeller can is still able to suspend solids is wider. For the lowest possible position of the impeller in the vessel ($C_b/T=0.05$) solids could not be suspended only when S_b/D was equal to 0.48, which corresponds to 24% of the tank content.

Photos of the stirred vessel with $C_b/T=0.30$ at different liquid levels (H/T) during the measurement of N_{js} are presented in Figure 6.13. Figure 6.13a and b show the solid-liquid dispersion at the point when the impeller speed reaches N_{js} when $S_b/D=2.3$ (H/T=1) and 0.77 (H/T=0.54), respectively. One can see that the solids are fully suspended. Figure 6.13c, where $S_b/D=0.59$ (H/T=0.49), shows that the solids cannot be suspended at any impeller speed despite the fact that the impeller is located well below the liquid level. In Figure 6.13d, which is the magnification of Figure 6.13c, solids can be observed at the bottom of the tank, indicating the failure of the system to suspend them. At this impeller submergence, increasing the impeller speed only increases the interface fluctuation at the air-liquid interface, causing impeller flooding (as explained in Chapter 4) and resulting in the inability of the impeller to suspend the solids. When this flow regime transition occurs, the average velocity field and turbulence intensity close to the tank bottom decreases substantially as the flow transitions from “double-loop” to “single-

loop up-pumping" (for relatively high C_b/T ratio; Figure 6.1 and Table 6.1) or from "single-loop down-pumping" to "single-loop up-pumping" (for relatively low C_b/T ratio; Figure 6.3 and Table 6.2). It is the flow regime transition that is responsible for air entrainment and the inability to suspend solids.

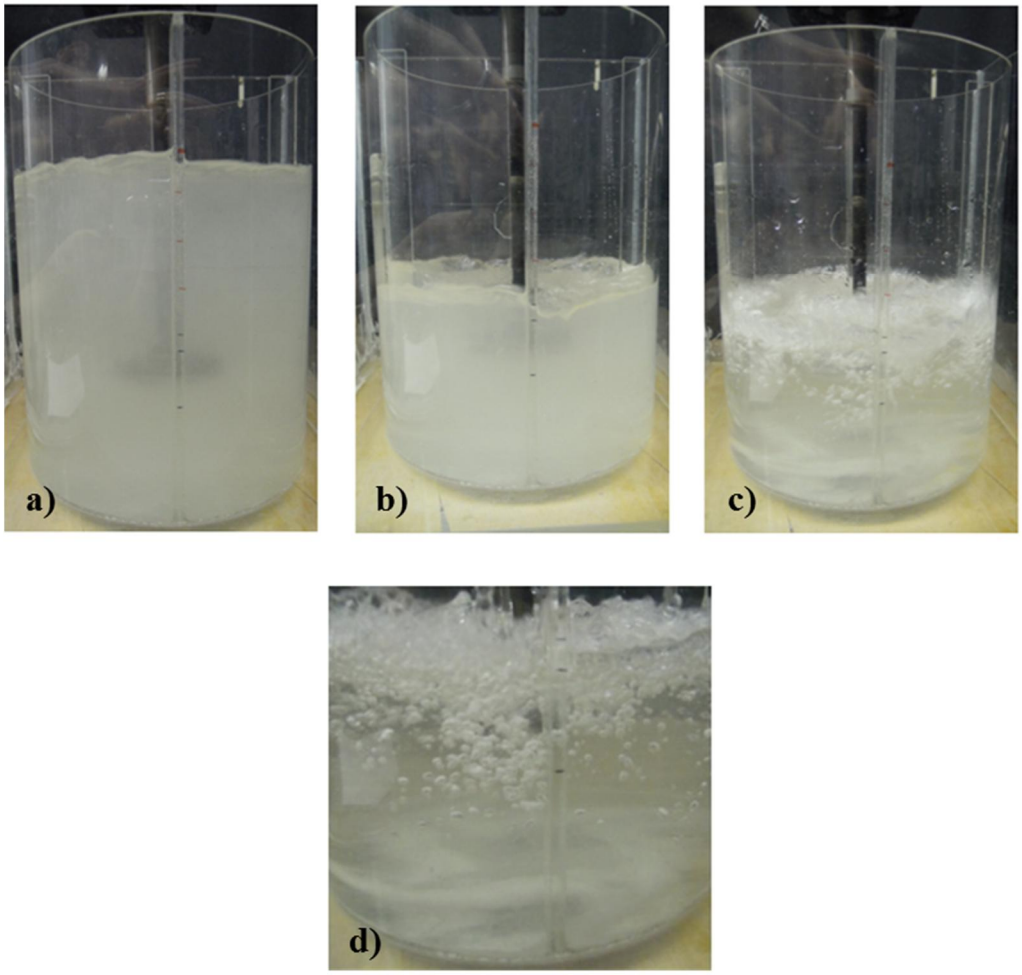

Figure 6.13 Solid liquid suspension at different S_b/D, for D/T=0.31 and C_b/T=0.30 (a) S_b/D=2.3 (H/T=1) and N=N_{js}; (b) S_b/D=0.77 (H/T=0.54) and N=N_{js}; (c) S_b/D=0.59 (H/T=0.49) and N_{js}=∞; (d) magnified view of Figure c.

6.4.2 Effect of Sb/D on Minimum Agitation Speed for Complete Off-Bottom Solid Suspension for Cb/T=0.30 and Different D/T

Figure 6.14 shows N_{js} measured for $C_b/T=0.30$ at two different impeller D/T ratios (0.31 and 0.43) as a function of the impeller submergence ratio (S_b/D). From this figure one can see that solids could be suspended at a lower agitation speed when using larger impellers i.e., by increasing the D/T ratios. This phenomenon has been reported by other researchers (Armenante et al., 1997, 1998). The predictions obtained using the correlations proposed by Armenante et al., (1998) were also included in this figure. The results obtained here are in agreement with those predictions for the case in which those correlations could be applied (H/T=1). It is worth mentioning that increasing the D/T ratio per se did not have any impact on the flow regime produced by the impeller, which

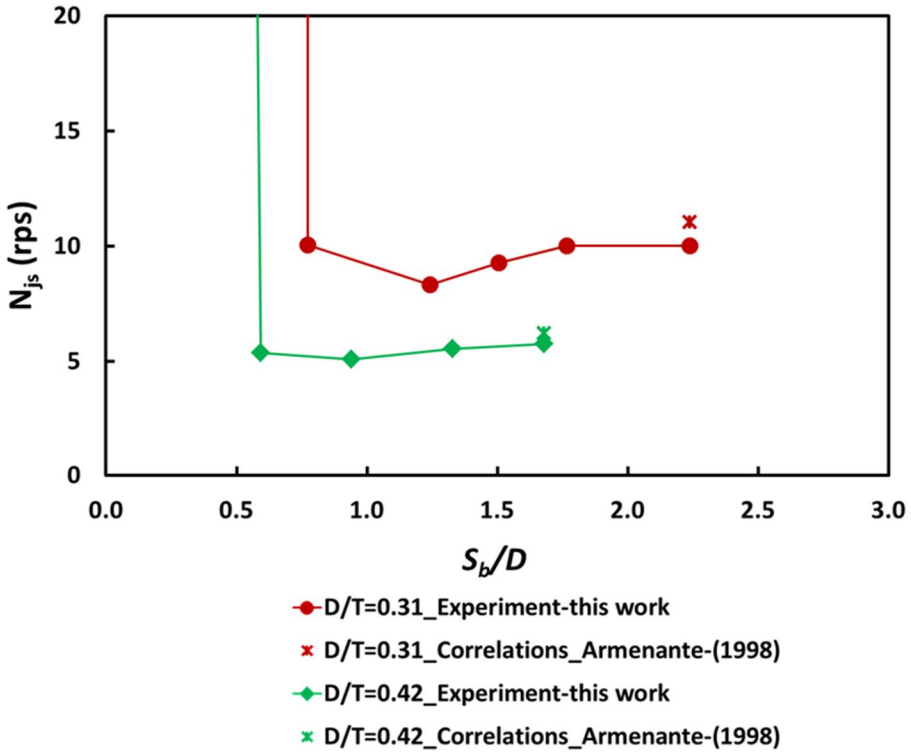

Figure 6.14 Minimum agitation speed for complete off-bottom solid suspension (N_{js}) as a function of impeller submergence ratio for $C_b/T=0.30$ and different D/T ratios.

depended only on the S_b/D ratio, as explained in Chapter 5. The most important effect of the D/T ration was the generation of stronger flow throughout the vessel.

Figure 6.14 additionally shows that there is a minimum liquid level below which that solids cannot be suspended ($N_{js}=\infty$) also for this case. The critical level for solid suspension was found to be $S_b/D=0.54$ (H/T=0.54) and 0.77 (H/T=0.54) for D/T=0.43 and 0.31, respectively. These impeller submergence ratios are exactly the same as those that have been reported in Chapter 5 as the critical levels for the flow pattern transition (from DL Regime to SL-up Regime) corresponding to sudden reduction in power number. Therefore, the same mechanism that was invoked in the previous section to explain these results can be applied here.

6.5 Conclusion III

i. The velocity field and turbulence intensity in a stirred tank change rapidly and significantly from "double-loop" (DL) Regime to "Single-loop up-pumping" (SL-up) Regime or from "single-loop down-pumping" (SL-up) to "single-loop up-pumping" (SL-up) when a critical value of the impeller submergence ratio is reached. This was shown to be especially significant for the following area in the vessel:

   a. near the tank bottom

   b. near the liquid-air interface

   These changes were more pronounced at higher agitation speeds.

ii. Above the critical impeller submergence ratio, S_b/D, which results in a flow regime change from DL Regime to SL-up Regime:

   a. Mixing time, t_{95} decreases with decreasing impeller submergence ratio

b. Non-dimensional mixing time, $t_{95}N$ remains constant irrespective of the agitation speeds for each impeller submergence ratio. Lower values for $t_{95}N$ can be observed for lower submergence ratios

iii. At or below the critical impeller submergence ratio, S_b/D, which results in a flow regime change from DL Regime to SL-up Regime:

a. Mixing time, t_{95}, increases suddenly compared the values at higher submergence ratios

b. $t_{95}N$ is no longer independent of the agitation speed but increases with agitation speed. This indicates that the mixing performance at low S_b/D ratios is reduced.

iv. For each impeller off-bottom clearance, C_b/T, there is a critical value of the impeller submergence ratio, S_b/D, below which solids cannot be suspended.

v. For each impeller D/T ratio, there is a critical value of the impeller submergence ratio, S_b/D, below which solids cannot be suspended.

vi. The results obtained here for mixing time and for the minimum agitation for solid suspension N_{js} confirm that a stirred vessel operating at low impeller submergence is more likely to experience impeller flooding conditions caused by surface air entrainment, especially at high agitation speed. Under these conditions, the impeller loses its ability to provide adequate liquid pumping and thus gives poor mixing results.

CHAPTER 7

OVERALL CONCLUSIONS

In this work, the different hydrodynamic regimes and recirculation patters which are encountered in partially filled, cylindrical, baffled tanks that are mechanically stirred by a central disk turbine (DT) impeller and in which the fill ratio H/T is lower than 1 have been described, and the operating ranges in which these regimes can exist have been specified. It was found that each regime exists within a very specific range of non-dimensional geometric variables, which included the impeller submergence ratio, S_b/D, the impeller off-bottom clearance ratio, C_b/T, and the impeller diameter-to-tank diameter ratio, D/T. In some of these regimes (typically associated with higher impeller submergence), the impeller was able to operate effectively and provide an adequate mixing level that resulted in effective impeller pumping levels, high power dissipations, and high velocities and turbulence intensities throughout the vessel. When operated in these regimes, the impeller was capable of adequately discharging its mixing duties, such as suspending disperse solids or rapidly homogenizing the tank contents, at liquid levels that were similar to those experience in completely filled tanks for which H/T=1. However, when the tank was operated in other regimes (typically associated with lower impeller submergence) the impeller was much less capable of producing effective mixing, as evidenced by reduced pumping effects, lower power dissipations, and reduced velocities and turbulence intensities throughout the vessel. Furthermore, the operation in one of these regimes made the system much more likely to incorporate air in the liquid through a vortex mechanism which eventually produced impeller flooding and severely reduced the mixing ability of the impeller, including preventing solid suspension altogether. One regime even resulted in the complete suppression of the pumping action

by the impeller and resulted in extremely poor mixing. Some more specific conclusions from this work are as follow:

1. In a standard stirred tank with $0.77<H/T<1$ and $C_b/T=0.31$, the DT impeller generates the “double-loop” recirculation flow typically observed in similar stirred tanks with H/T=1
2. For the same system, the macroscopic flow pattern changes by decreasing S_b/D from 0.77 to 0.59, thus transitioning from a “double loop” recirculation flow (DL Regime) to a "single loop-up-pumping" recirculation flow (SL-up Regime). When this transition occurs the Power Number and radial Pumping Number drop significantly
3. The critical impeller submergence ratio which results in the establishment of the newly described SL-up Regime is not affected by dynamic variables such as agitation speed;
4. Significant surface air entrainment possibly resulting in impeller flooding for low S_b/D liquid system be can observed only when; (1) the SL-up regime becomes established and; (2) the Froude number (and consequently the agitation speed) is high enough to create a vortex reaching the impeller.
5. The velocity profiles, velocity contours, Power Number and Pumping Number at different impeller submergence ratios can be predicted by FS-CFD simulations and the prediction are in a good agreement with those measured experimentally through PIV. VOF-CFD simulations are able to predict values that are in closer agreement with the experimental data at lower S_b/D ratios including when surface deformation occurs (S_b/D =0.59).

6. In a standard stirred tank where S_b/D and C_b/T are both varied the following regimes can be observed depending on the values of these variable:

   a. Double Loop (DL) Regime (at high S_b/D and high C_b/T)

   b. Single Loop-downpumping (SL-dp) Regime (at high S_b/D and low C_b/T)

   c. Single Loop-uppumping (SL-up) Regime (at low S_b/D and high or low C_b/T)

   d. No Circulation (NC) Regime (at low S_b/D and very low C_b/T)

   The following diagram (for D/T=0.31) can be used to determine the operational regime depending on the value of the geometric ratios

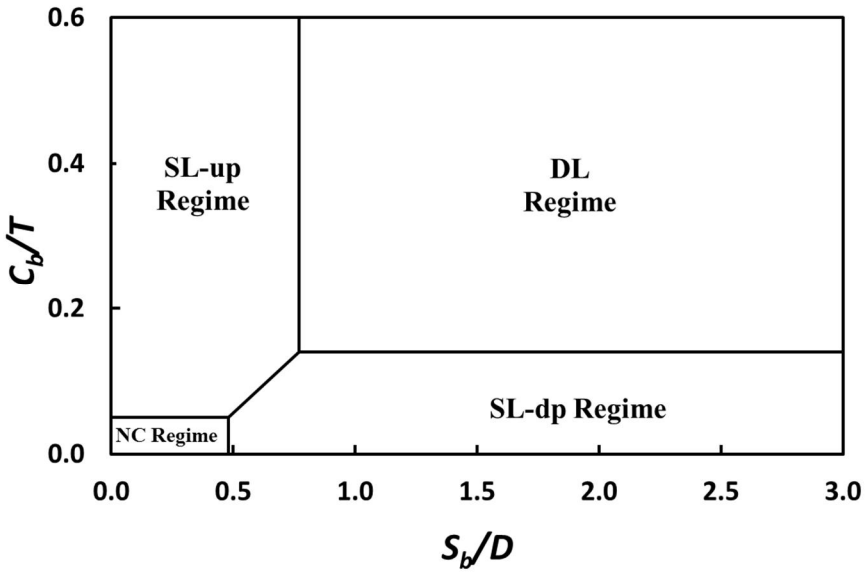

7. For a given C_b/T ratio and D/T ratio a critical impeller submergence S_{bc}/D value exists where the fluid undergoes a transition from its initial flow Regime (DL Regime or SL-dp Regime) to the SL-up Regime, or for very low vales of C_b/T, to the NC Regime

8. The SL-up Regime typically occurs well before the liquid level drops to the impeller level
9. The critical impeller submergence S_{bc}/D value is higher (and hence the operating window in which the system can be operated without entering the SL-up Regime is wider) when:
    a. the impeller off-bottom clearances (C_b/T) is lower;
    b. the D/T ratio is larger
10. The NC Regime, only achievable for very low impeller off-bottom clearances ($C_b/T \leq 0.05$) and low S_b/D ratios, results in no clear recirculation and very poor mixing conditions
11. Surface air entrainment and impeller flooding can only be achieved if the following conditions are both met:
    a. S_b/D is low enough to produce SL-up Regime; and
    b. the agitation speed N is high enough to result in a Froude number sufficiently large to create a vortex reaching the impeller
12. Three types of transitions in flow regime were observed as the S_b/D was lowered:
    a. DL Regime to SL-up Regime
    b. SL-dp Regime to SL-up Regime
    c. SL-dp Regime to NC Regime
13. These flow transitions are associated with a sudden drop in Power Number, Po and the possibility of surface air entrainment if the agitation speed is appropriately high, thus resulting in even lower Po values

14. The following equation (where S_d is the submergence of the disk in a DT impeller and $Fr_{flooding}$ is the impeller Froude number at the agitation speed at flooding) can be used to determine the agitation speed at which impeller flooding from surface air entrainment occurs provided that the impeller is in the SL-up Regime:

$$Fr_{flooding} = \frac{N_{flooding}^2 D}{g} = 0.175\left(\frac{T}{D}\right)^{0.7107}\frac{S_d}{D}$$

15. The velocity field and turbulence intensity in a stirred tank also change rapidly and significantly when a regime transition occurs from DL Regime to SL-up Regime or from SL-dp Regime to SL-up Regime. This is especially significant for the following area in the vessel:
    a. near the tank bottom
    b. near the liquid-air interface
16. Above the critical impeller submergence ratio, S_b/D, which results in a flow regime change from DL Regime to SL-up Regime:
    a. Mixing time, t_{95} decreases with decreasing impeller submergence ratio
    b. Non-dimensional mixing time, $t_{95}N$ remains constant irrespective of the agitation speeds for each impeller submergence ratio. Lower values for $t_{95}N$ can be observed for lower submergence ratios
17. At or below the critical impeller submergence ratio, S_b/D, which results in a flow regime change from DL Regime to SL-up Regime:
    a. Mixing time, t_{95}, increases suddenly compared the values at higher submergence ratios

b. $t_{95}N$ is no longer independent of the agitation speed but increases with agitation speed. This indicates that the mixing performance at low S_b/D ratios is reduced.

18. For each impeller off-bottom clearance, C_b/T, there is a critical value of the impeller submergence ratio, S_b/D, below which solids cannot be suspended.

19. For each impeller D/T ratio, there is a critical value of the impeller submergence ratio, S_b/D, below which solids cannot be suspended.

20. The results obtained here for mixing time and for the minimum agitation for solid suspension N_{js} confirm that a stirred vessel operating at low impeller submergence is more likely to experience impeller flooding conditions caused by surface air entrainment, especially at high agitation speed. Under these conditions, the impeller loses its ability to provide adequate liquid pumping and thus gives poor mixing results.

It is important to remark again that the establishment of the SL-up Regime is a necessary but not sufficient condition for facilitated surface air entrainment and impeller flooding to occur in the system examined here. Furthermore, the establishment of the SL-up Regime can only occur if S_b/D is lowered to a critical value, which also depends on other geometric parameter (C_b/T and D/T). Once the SL-up Regime is established, surface air entrainment is greatly facilitated and it will occur for a sufficiently high value of Froude Number (which needs high value of agitation speed, N). When this flow regime transition occurred, it was observed that the average velocity field and turbulence intensity close to the tank bottom decreased substantially, which was identified as the reason why mixing time increased suddenly and solid suspension became problematic.

In conclusion, in this work the role that key geometric and dynamic parameters play that result in different operating regimes for vessels operated under partial fill ratio conditions were determined and quantified. Furthermore, in this work, the establishment of a previously unreported hydrodynamic regime at critical impeller submergences was described. This regime is not only associated with reducing mixing effectiveness, but can also explain why phenomena such as air entrainment and loss in impeller pumping capacity occur at low H/T ratios. It is expected that the knowledge developed in this work will help practitioners properly operate their equipment in regions where the desired mixing effects can be achieved.

REFERENCES

Akiti, O. and P. M. Armenante (2004). "Experimentally-Validated Micromixing-Based CFD Model for Feld-Batch Stirred-Tank Reactors." AIChE Journal **50**(3): 566-577.

Armenante, P. M. and C. C. Chou (1996). "Velocity Profiles in a Baffled Vessel with Single or Double Pitched-Blade Turbines." AIChE Journal **42**(1): 42-54

Armenante, P. M., C. Luo, et al. (1997). "Velocity profiles in a closed, unbaffled vessel: Comparison between experimental LDV data and numerical CFD predictions." Chemical Engineering Science **52**(20): 3483-3492.

Armenante, P. M. and E. U. Nagamine (1998). "Effect of low off-bottom impeller clearance on the minimum agitation speed for complete suspension of solids in stirred tanks." Chemical Engineering Science **53**(9): 1757-1775.

Armenante, P. M., E. U. Nagamine, et al. (1998). "Determination of correlations to predict the minimum agitation speed for complete solid suspension in agitated vessels." Canadian Journal of Chemical Engineering **76**(3): 413-419.

Armenante, P. M., Y. T. Huang, et al. (1992). "Determination of the minimum agitation speed to attain the just dispersed state in solid-liquid and liquid-liquid reactors provided with multiple impellers." Chemical Engineering Science **47**(9-11): 2865-2870.

Baldi, G., R. Conti, et al. (1978). "Complete suspension of particles in mechanically agitated vessels." Chemical Engineering Science **33**(1): 21-25.

Bhattacharya, S., D. Hebert, et al. (2007). "Air entrainment in baffled stirred tanks." Chemical Engineering Research and Design **85**(5 A): 654-664.

Brocchini, M. and D. H. Peregrine (2001). "The dynamics of strong turbulence at free surfaces. Part 1. Description." Journal of Fluid Mechanics **449**: 225-254.

Brucato, A., A. Cipollina, et al. (2010). "Particle suspension in top-covered unbaffled tanks." Chemical Engineering Science **65**(10): 3001-3008.

Campolo, M., A. Paglianti, et al. (2002). "Fluid dynamic efficiency and scale-up of a retreated blade impeller CSTR." Industrial and Engineering Chemistry Research **41**(2): 164-172.

Chapple, D., S. M. Kresta, et al. (2002). "The effect of impeller and tank geometry on power number for a pitched blade turbine." Chemical Engineering Research and Design **80**(4): 364-372.

Choi, B. Y. and M. Bussmann (2007). "A piecewise linear approach to volume tracking a triple point." International Journal for Numerical Methods in Fluids **53**(6): 1005-1018.

Collignon, M. L., A. Delafosse, et al. (2010). "Axial impeller selection for anchorage dependent animal cell culture in stirred bioreactors: Methodology based on the impeller comparison at just-suspended speed of rotation." Chemical Engineering Science **65**(22): 5929-5941.

Coroneo, M., G. Montante (2011). "CFD prediction of fluid flow and mixing in stirred tanks: Numerical issues about the RANS simulations." Computers and Chemical Engineering **35**: 1952-1968.

Deglon, D. A. and C. J. Meyer (2006). "CFD modeling of stirred tanks: Numerical considerations." Minerals Engineering **19**(10): 1059-1068.

Distelhoff, M. F. W., A. J. Marquis, et al. (1997). "Scalar Mixing Measurements in Batch Operated Stirred Tanks." Canadian Journal of Chemical Engineering **75**(4): 641-652.

Dyster, K. N., E. Koutsakos, et al. (1993). "LDA study of the radial discharge velocities generated by a Rushton turbine: Newtonian fluids, Re $\geq$ 5." Chemical Engineering Research and Design **71**(A1): 11-23.

Gueyffier, D., J. Li, et al. (1999). "Volume-of-Fluid Interface Tracking with Smoothed Surface Stress Methods for Three-Dimensional Flows." Journal of Computational Physics **152**(2): 423-456.

Haque, J. N., T. Mahmud, et al. (2006). "Modeling turbulent flows with free-surface in unbaffled agitated vessels." Industrial and Engineering Chemistry Research **45**(8): 2881-2891.

Horowitz, A. (2010) "Is the reign of batch processing coming to an end?" Life Science Leader (accessed November, 2010).

Hirt, C. W. and B. D. Nichols (1981). "Volume of fluid (VOF) method for the dynamics of free boundaries." Journal of Computational Physics **39**(1): 201-225.

Ibrahim, S. and A. W. Nienow (1996). "Particle suspension in the turbulent regime: The effect of impeller type and impeller/vessel configuration." Chemical Engineering Research and Design **74**(6): 679-688.

Ibrahim, S. and A. W. Nienow (1999). "Comparing impeller performance for solid-suspension in the transitional flow regime with Newtonian fluids." Chemical Engineering Research and Design **77**(8): 721-727.

Javed, K. H., T. Mahmud, et al. (2006). "Numerical simulation of turbulent batch mixing in a vessel agitated by a Rushton turbine." Chemical Engineering and Processing: Process Intensification **45**(2): 99-112.

Kasat, G. R. and A. B. Pandit (2005). "Review on mixing characteristics in solid-liquid and solid-liquid-gas reactor vessels." Canadian Journal of Chemical Engineering **83**(4): 618-643.

Li, Z., Y. Bao, et al. (2011). "PIV experiments and large eddy simulations of single-loop flow fields in Rushton turbine stirred tanks." Chemical Engineering Science **66**(6): 1219-1231.

Lane, G. L. and P. T. L. Koh (1997). "CFD simulation of a Rushton turbine in a baffled tank." Inter Cnf on CFD in Mineral & Metal Processing and Power Generation.

Mahmoudi, S. M. and M. Yianneskis (1992). "The variation of flow pattern and mixing time with impeller spacing in stirred vessels with two Rushton impellers."

Mahmud, T., J. N. Haque, et al. (2009). "Measurements and modeling of free-surface turbulent flows induced by a magnetic stirrer in an unbaffled stirred tank reactor." Chemical Engineering Science **64**(20): 4197-4209.

Mali, R. G. and A. W. Patwardhan (2009). "Characterization of onset of entrainment in stirred tanks." Chemical Engineering Research and Design **87**(7): 951-961.

Montante, G., K. C. Lee, et al. (2001). "Experiments and predictions of the transition of the flow pattern with impeller clearance in stirred tanks." Computers and Chemical Engineering **25**(4-6): 729-735.

Montante, G., K. C. Lee, et al. (2001). "Numerical simulations of the dependency of flow pattern on impeller clearance in stirred vessels." Chemical Engineering Science **56**(12): 3751-3770.

Murthy, B. N. and J. B. Joshi (2008). "Assessment of standard k - ε{lunate}, RSM and LES turbulence models in a baffled stirred vessel agitated by various impeller designs." Chemical Engineering Science **63**(22): 5468-5495.

Nagata, S. (1975). "Mixing. Principles and applications." Haltset Press, New York

Nienow, A. W. (1968). "Suspension of solid particles in turbine agitated baffled vessels." Chemical Engineering Science **23**(12): 1453-1459.

Ochieng , A. , M. S Onyango, et al., (2007). "Mixing in a tank stirred by a Rushton turbine at a low clearance." Chemical Engineering and Processing **47**: 842-851.

Patwardhan, A. W. and J. B. Joshi (1998). "Design of stirred vessels with gas entrained from free liquid surface." Canadian Journal of Chemical Engineering **76**(3): 339-365.

Pilliod, J. E. and E. G. Puckett (2004). "Second-order accurate volume-of-fluid algorithms for tracking material interfaces." Journal of Computational Physics **199**(2): 465-502.

Rushton, J.H., Costich, E.W. and Everett, H.J. (1950). "Power characteristics of mixing impellers - Part I." Chem. Engng Prog. **46**: 395-404

Rutherford, K., S. M. S. Mahmoudi, et al. (1996). "The influence of Rushton impeller blade and disk thickness on the mixing characteristics of stirred vessels." Chemical Engineering Research and Design **74**(3): 369-378.

Sardeshpande, M. V., A. R. Sagi, et al. (2009). "Solid suspension and liquid phase mixing in solid-liquid stirred tanks." Industrial and Engineering Chemistry Research **48**(21): 9713-9722.

Serra, A., M. Campolo, et al. (2001). "Time-dependent finite-volume simulation of the turbulent flow in a free-surface CSTR." Chemical Engineering Science **56**(8): 2715-2720.

Sheng, J., H. Meng, et al. (2000). "A large eddy PIV method for turbulence dissipation rate estimation." Chemical Engineering Science **55**(20): 4423-4434.

Smit L. and J. During (1991). "Vortex geometry in stirred vessel." 7th European Congress on Mixing **2:** 633-639.

Tamburini, A., A. Cipollina, et al. (2011). "Dense solid-liquid suspensions in top-covered unbaffled stirred vessels." Chemical Engineering Transactions **24**: 1441-1446.

Wang, W., Z. S. Mao, et al. (2006). "Experimental and numerical investigation on gas holdup and flooding in an aerated stirred tank with Rushton impeller." Industrial and Engineering Chemistry Research **45**(3): 1141-1151.

Wu, H. and G. K. Patterson (1989). "Lasser-doppler measurements of turbulent-flow parameters in a stirred mixer." Chemical Engineering Science **44**(10): 2207-2221.

Yang, T. and K. Takahashi (2010). "Effect of impeller blades angle on Power Number and flow pattern in horizontal stirred vessel." Journal of Chemical Engineering of Japan **43**(8): 635-640.

Yeoh, S. L., G. Papadakis, et al. (2004). "Numerical simulation of turbulent flow characteristics in a stirred vessel using the LES and RANS approaches with the sliding/deforming mesh methodology." Chemical Engineering Research and Design **82**(7): 834-848.

Yianneskis, M., Z. Popiolek, et al. (1987). "Experimental Study of the steady and unsteady flow characteristics of stirred reactors." Journal of Fluid Mechanics **175**: 537-555.

Zhao, J., Z. Gao, et al. (2011). "Particle image velocimetry study of flow patterns and mixing characteristics in multiple impeller stirred tank." Journal of Chemical Engineering of Japan **44**(6): 389-397.

Zwietering, T. N. (1958). "Suspending of solid particles in liquid by agitators." Chemical Engineering Science **8**(3-4): 244-253.

Paul, E. L., V. Atiemo-Obeng and S. M. Kresta (2004). Handbook of Industrial Mixing, Hoboken: John Wiley & Sons, Inc.

Marshal, E. M. and A. Bakker. Computational Fluid Mixing, Fluent Inc. (http://www.bakker.org/cfmbook/cfmbook.htm, accessed October 2010)

www.ansys.com, accessed October, 2010.

www.fluentusers.com, accessed October, 2010.